Pore pressure evolution and related risk at Gaustad, Oslo

Rannveig Brørvik Sæten

Thesis submitted for the degree of
Master in Environmental Geosciences
60 credits

Department of Geosciences
Faculty of Mathematics and Natural Sciences

UNIVERSITY OF OSLO

Autumn 2021

Pore pressure evolution and related risk at Gaustad, Oslo

Rannveig Brørvik Sæten

Pore pressure evolution and related risk at Gaustad, Oslo

http://www.duo.uio.no/

Printed: Reprosentralen, University of Oslo

Abstract

The hydrogeological setting in Gaustadbekkdalen consists of a confined fractured bedrock aquifer, covered by marine sediments. The marine sediments consists mainly of clay, which in some areas are found to be quick clay. Layers of silt and sand are interbedded in the marine clay. The UiO's Life Science Building is being constructed in Gaustadbekkdalen and is set to be finished in 2026. During construction work the groundwater level in the area is lowered, causing the potential for pore pressure reduction in the overlying aquitard. The extent of the interbedded silt and sand layers are interpolated from CPTU data. A 3D steady state groundwater model of the construction area is constructed and the model sensitivity is studied. The sensitivity study assesses the effect of representing the interbedded silt and sand in the marine clay. Further, the potential for differential sediment compaction is assessed based on experience data. The silt and sand layers have a greater thickness in the areas north and south of the construction area, and show a trend towards pinching out to the east. The groundwater model results show that representing the silt and sand layers makes the marine sediment more sensitive to groundwater level changes in the fractured aquifer. The assessed risk of potential sediment compaction in relation to surrounding buildings and infrastructure is considered low.

Acknowledgements

First, I would like to thank my supervisors, Anja Sundal and Kevin J. Tuttle, for all the help along the way and the support you have given me. For help with chemical analysis of the water samples I would like to thank Mufak Naoroz and Magnus Kristoffersen.

Thank you to Statsbygg and Grunnteknikk AS for providing me the relevant data and access to the construction site.

Thank you to all of the lovely students in room 217, for all the laughs and help along the way and to the girls in the computer lab for the motivational words towards the end of this marathon. Thank you to Frøya Vold Bjørvik for the help during field work and the exchange of ideas. And lastly, I would like to thank my sister, Barbro Brørvik Sæten, for your love and support along the way.

Contents

List of Figures

List of Tables

Chapter 1

Introduction

As the city of Oslo is increasing in size and population the need for new buildings and infrastructure is growing. As a result, construction occurs in close proximity to already existing infrastructure, which poses a risk to cause damage on surrounding buildings. Construction in Oslo has always been challenging due to presence of marine mud and quick clay. One of the biggest reasons for ground settling and differential compaction in Oslo is changes in pore pressure in these sediments (Eriksson et al., 2019). There are numerous examples in Oslo of how urban development can cause damage to surrounding structures, were Bjørvika is one of the most recognized cases (Hauser, 2020). Ground work for urban development influence the pore pressure in the marine mud causing a potential for ground settling and differential compaction. In 2012 the Norwegian Geotechnical Institute (NGI) started the project Limiting Damage (Begrens Skade) to increase the knowledge on how to minimize damage from differential compaction in relation to foundation work. The project was continued through the REMEDY research project (Langford, 2020). Acquiring more and improved knowledge on how pore pressure and groundwater is affected by the invasive measures during construction is central to reduce risk of differential settling and costly damage often related to foundation work.

1.1 Background

The construction of UiO´s Life Science Building started in 2019 with excavations of the sediments at the site. Statsbygg is the project coordinator and Norconsult is the entrepreneur responsible for the construction. During ground investigations the presence of clay with varying content of silt and sand layers was uncovered. The marine clay has proven to be quick clay and a limestone cement mixture has been used to stabilize the sediment (VAV and Statsbygg, 2019). During construction, a temporary open pit is excavated. To prevent groundwater influx and drainage, installation of sheet pile walls with anchors and foundation piles (for anchoring in bedrock) are needed. The Limiting Damage (Begrens Skade) project has documented that such installations often lead to unwanted

groundwater drainage of bedrock and pore pressure reductions in clayey sediment. During installation of foundation piles the sediment is displaced which cause a local horizontal displacement (Langford and Sandene, 2015), but as the sediment reconsolidates settling may occur. After installation, a common problem is leakage along the pile structures causing a decline in the piezometric surface in fractured bedrock and pore pressure reduction in the sediment (Baardvik et al., 2016).

1.2 Main Objectives

In this study the pore pressure evolution at the site of UiO´s Life Science Building (LSB) will be assessed. During foundation work at the site groundwater levels are lowered causing the pore pressure in the overlaying marine sediments to change. The marine sediments consists mainly of clay with horizontal layers of sand and silt of varying thickness. A 3D model of groundwater flow and hydraulic head in the study area has been constructed using the USGS modeling software MODFLOW. The effect of representing the marine stratigraphic units in the model is assessed by conducting a sensitivity study. Further, the pore pressure changes in the marine sediments will be analysed and the potential for sediment compaction is estimated. Normally, the pore pressure change is monitored for the first years after construction is completed, but pore pressure migration in low permeability sediments such as clays may take decades (Janbu, 1970). The main aim of this thesis is to study the effect pore pressure changes has on sediments potential to settle when being exposed to the invasive measured during foundation work. To assess this several research questions have been formulated:

- Analysing the effect of representing marine stratigraphic units in the 3D groundwater model of the study area.
- Assessing the effect the sedimentary layer distribution in the aquitard has on pore pressure distribution and migration, and the potential risks associated with these changes in an urban environment.
- Assessing the potential for sediment compaction as a result of pore pressure changes in the aquitard.

Chapter 2

Study Area and Data

The study area is located in the urban area of Gaustadbekkdalen, Oslo with close proximity to the Research Park at UiO and highway 150 (Ring 3), one of the biggest motorways in Oslo (figure 2.1). The pit has a northeast-southwest orientation and covers an area of about 29 000m^2. On the northwestern side of the construction site bedrock is exposed, while for the rest of the pit marine mud deposits dominate (VAV and Statsbygg, 2019). In some areas the marine mud is overlain by anthropogenic fill. Investigations by Hognestad and Tuttle (2020) have shown that the groundwater at the site is flowing into the aquifer, situated below the construction area, from the north. Sheet piling has been installed outside the perimeter of the planned building for stabilizing the sediment and prevention of groundwater flow into the area (Tuttle, 2020). The installation of foundation piles is scheduled to start in August 2021. As a part of Oslo municipality's plan for reopening rivers and streams, parts of Gaustad river will be flowing in an artificial stream at the LSB (VAV and Statsbygg, 2016). A new culvert has been constructed outside the sheet piling walls, following the wall along the east and south borders, to transport the greater volumes of Gaustad river underground.

Infrastructure in close proximity to the construction pit may be sensitive to changes in groundwater levels and potential settling of sediment. Among others, is the tram lines on the northwestern side of the construction site that follow Gaustadallèen and turns onto Problemveien. During construction of the tram line sediment was overlaid with EPS geofoam to prevent settling (Mehus et al., 2000). To prevent water absorption and damage to the EPS-filling drains follow the path of the tram line with the low point assumed to be at 81 - 82m.a.s.l. near PZ93 (figure 2.1) (Hognestad and Tuttle, 2020). Gaustadbekkdalen is a part of Gaustad that has become increasingly more urbanized over the last 50 years (VAV and Statsbygg, 2019 ; NGI, 1971). Housing on the south-east side of the construction area, in Bukken Bruses vei, is another area that is monitored closely to prevent damage due to potential changes in groundwater level.

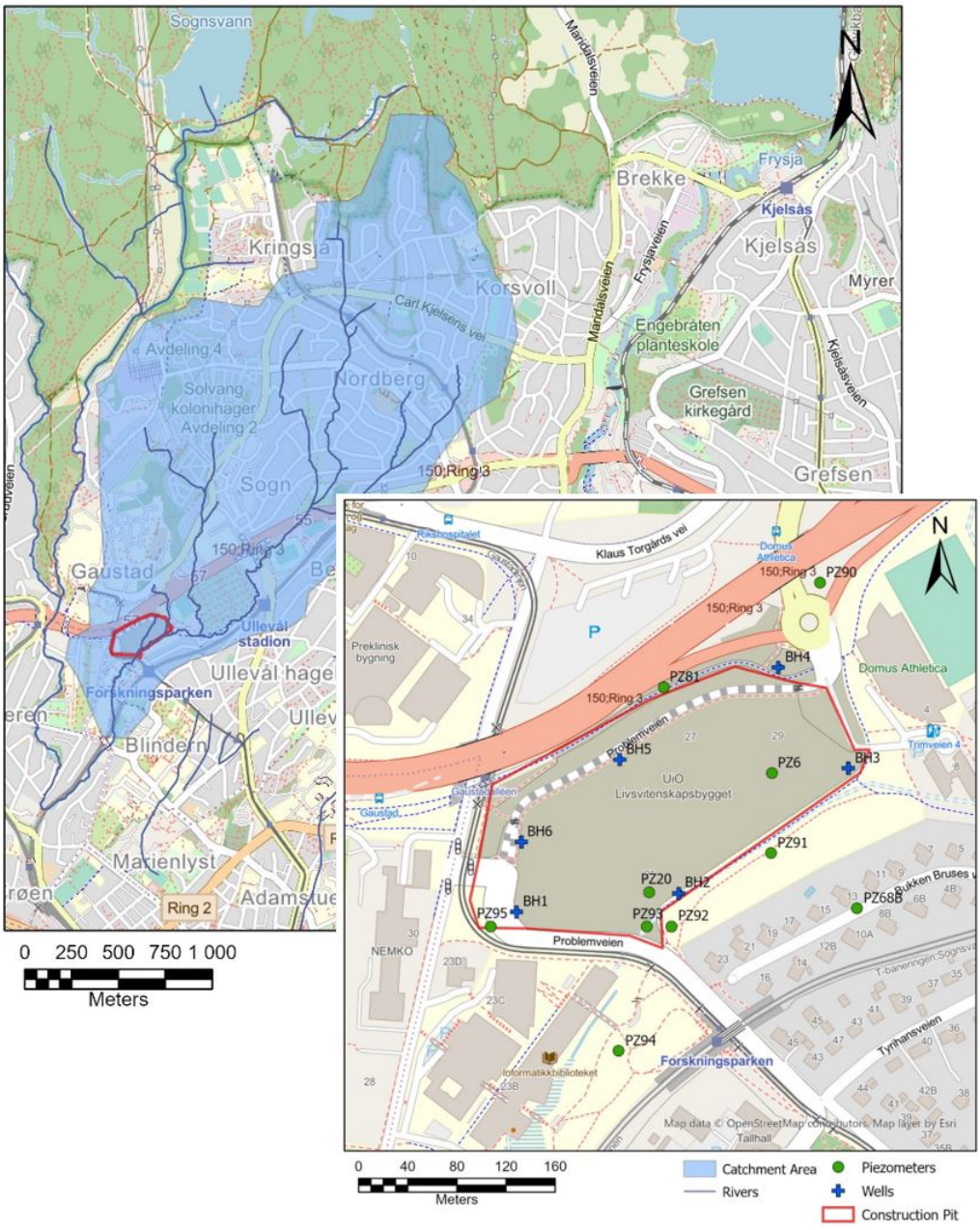

Figure 2.1: The study area is located in the catchment area of Gaustad river. The rivers in the catchment are mostly closed and flowing in drainage pipes. Six observation wells and ten piezometers have been installed in and around the construction pit. PZ6 & PZ20 was installed in 2015, but are no longer active measuring points.

2.1 Geological Background

2.1.1 Bedrock

Oslo is located in the area of Oslo Graben that formed during continental rifting in the Late Carboniferous to Permian (Stratford and Thybo, 2011). During the early and mid-stages of rifting basaltic magma was formed, while around 280 Ma the composition of the magma changed, forming a granitic and syenitic crust (Stratford and Thybo, 2011). Fault structures surrounding the graben set a divide between the Permian igneous rock and the Precambrian rock of the Fennoscandian shield (Oftedahl, 1959). The Precambrian rock consist of granite, biotite gneisses, migmatites, minor quartzite and amphiboles (Ramberg and Smithson, 1971). Cambro-Silurian marine deposits formed during a marine succession, later to be folded by the Caledonide Orogeny (Neumann et al., 1992). The bedrock in Gaustadbekkdalen is part of this Cambro-Silurian formation.

The bedrock in Gaustadbekkdalen consists of alternating shale and limestone, nodular limestone and shale (figure 2.2 A)) (Lutro et al., 2017). It is part of the Oslo Group lithostratigraphic unit formed during Mid to Late Ordovician. The Oslo Group is dominated by nodular limestone formations with increasing elements of silt-/sandstone towards the top of the unit (NGU, 2020). During the formation of the Oslo Graben the Oslo Group unit was subject to stress and strain (Stratford and Thybo, 2011 ; Lutro et al., 2017), which caused fractures and faulting in the bedrock. The Blindern fault runs in a northeast-southwest direction south of the construction site (Lutro et al., 2017). Exposed bedrock within the study area show varying degrees of deformation and fracturing frequency.

2.1.2 Quaternary Sediments

During the last glaciation (Weichselian) most of the earlier Quaternary sediments on the Norwegian land mass was removed by the ice (Mangerud et al., 2011). The sediment situated on top of the Ordivician bedrock at Gaustad is mainly marine clay deposited during late Weichselian when the marine limit around Oslo was 220 m.a.s.l. (figure 2.2 B)) (Solheim and Groenlie, 1983). Ground investigations report the marine clay sediment to be 1 - 30m thick with interbedded thin layers of sand and silt (VAV and Statsbygg, 2019). The total sediment thickness varies with the topography of the bedrock. NGI (1971) give a description of three rivers valleys situated in Gaustadbekkdalen (figure A.1), that were filled with anthropogenic masses in the time before the 1950s.

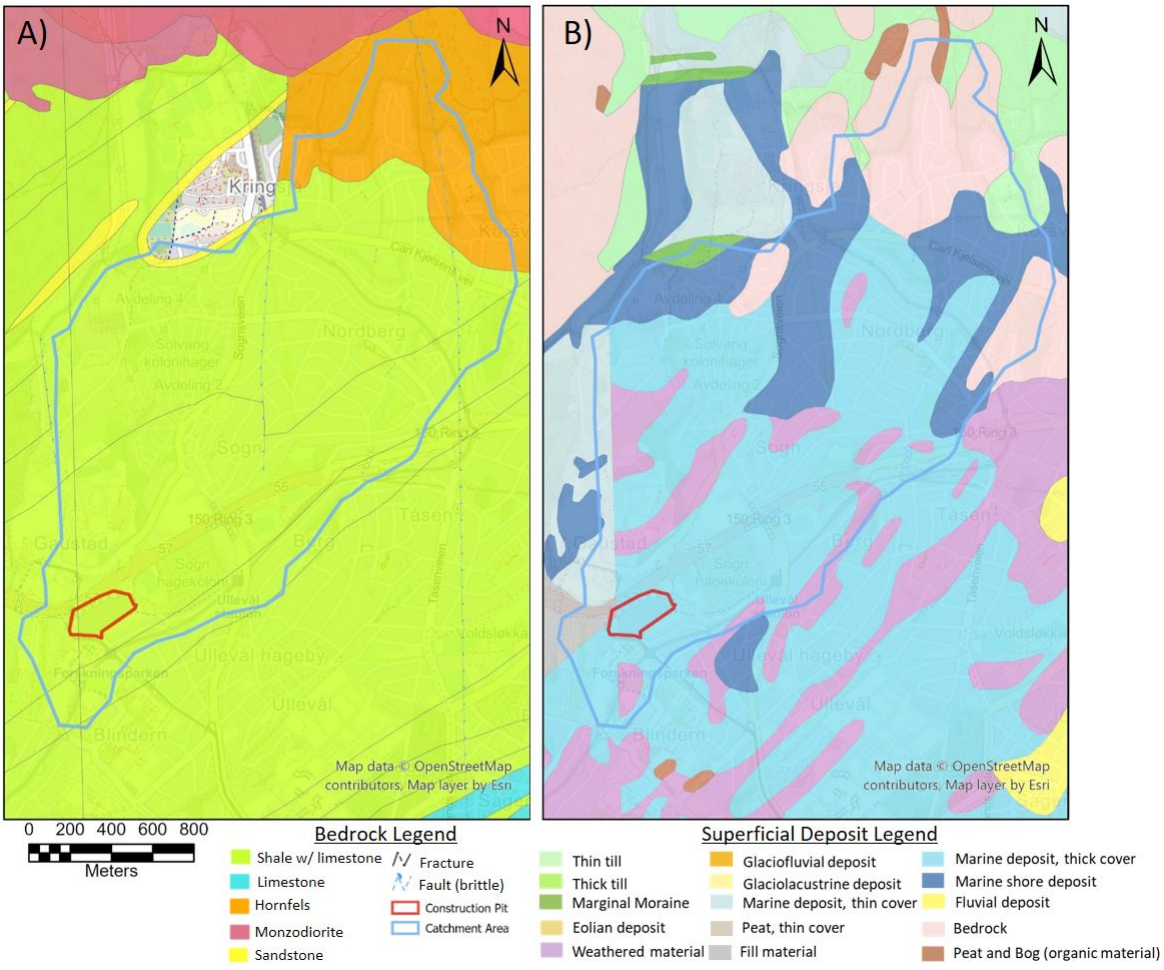

Figure 2.2: A) Bedrock map of the study area show a great extent of shale with limestone nodules. B) Superficial deposits in the study area are predominantly a thick cover of marine sediments. Map layers are downloaded from Geological Survey of Norway.

2.2 Data

Ground investigations have been done in the area close to the construction site several times in relation to other projects of development, before the start of the LSB project. These data have provided relevant information about the geological history and anthropogenic influence at the site. VAV and Statsbygg (2019) summarize the findings of resent ground investigations by GrunnTeknikk AS, and previous work by COWI in 2012. Observations and interpretations from total sounding, Cone Penetration Test Undrained (CPTU) and core sampling determine sediment properties and depth to bedrock. Six boreholes (BH) located inside the construction area were installed in 2019 by Seabrokers, and all boreholes were logged by NGI (Norwegian Geotechnical Institute). The borehole logs contain images from an optic televiewer, data from natural gamma radiation, bedrock resistivity, fractures, layering, and in some intervals loss of water has been measured through a Lugeon test (VAV and Statsbygg, 2020). Before construction started, ten piezometers were installed to monitor the pore pressure change during construction, but also to determine the pore pressure before ground work initiated (figure 2.1) (Hognestad and Tuttle, 2020). Tuttle (2020) has previously modelled the 2D pore pressure evolution in the sediment and bedrock at the construction site. The sediment situated above bedrock was then assumed to be homogeneous.

2.2.1 Total Sounding, CPTU and Core Sampling

Total sounding gives depth to bedrock and an indication of the sediment stratification. The depth to bedrock varies greatly, and within the construction pit the bedrock forms a valley oriented northeast - southwest. In the north end of the pit, close to BH5 and BH6 (figure 2.1), depth to bedrock is sallow, and during construction bedrock has been exposed. In some measuring points the presence of a basal moraine layer is located between the bedrock and overlaying sediment. The CPTU measurements gives information about the soil stratification, mechanical soil parameters and an indication of the soil type (figure A.2 - A.17). The data from CPTU tests is applied to parameterize the layering of the model in MODFLOW. From the core samples, both grain size analyze and triaxial testing is preformed. The triaxial testing gives the shear strength, sensitivity, water content, plastic limit and liquid limit of the soil.

2.2.2 Borehole Observations

Of the six boreholes installed four of them is intended for injection of water to maintain the groundwater level during the construction period. BH5 and BH6 was drilled and logged in 2019, but as construction continued they were closed off. Based on the borehole logs it is clear that the bedrock consists predominantly of shale with layers and nodes of limestone.

The layering in BH1, BH4 and BH6 all have a strike direction towards east/southeast, while the strike direction of layering in BH2, BH3 and BH5 have no clear trend (VAV and Statsbygg, 2020). All boreholes contain open and closed fractures with varying orientation (figure A.18 - A.23). In both BH1 and BH6, interpretation of the logs determine the presence of an intrusive syenite. In BH1 the syenite is located in the intervals 44.4 - 40.7m.a.s.l. and 37.3 - 35.4m.a.s.l., while in BH6 it is observed between 81.2 - 79.2m.a.s.l. Table 2.1 summarize measurements of hydraulic head in the six boreholes in December 2019 (Hognestad and Tuttle, 2020).

Table 2.1: Measurements of hydraulic head in boreholes December 2019 by Hognestad and Tuttle (2020).

ID	Depth from TOC (m)	Surface elevation (m)	Hydraulic head (m)
BH1	3.85	94.8	90.7
BH2	7.7	89.3	81.6
BH3	2.0	92.9	90.9
BH4	3.9	95.0	91.1
BH5	4.1	96.7	92.6
BH6	7.1	97.7	90.6

Chapter 3

Theoretical Framework

3.1 Hydrogeology

Hydrogeology is the study of the interrelationship between water and geological materials (Fetter, 2018). As water on the Earths surface is transported trough the water cycle it interacts with soil and rock. The presence of water affect the behavior and stability of geological materials (NGI, 2020), therefore it is important to have knowledge of the hydrologic conditions when altering the ground surface during urban development.

3.1.1 Hydrologic Cycle

The hydrologic cycle describes how water is transported from the ocean, into the atmosphere, and onto and across the land (Hiscock and Bense, 2014). Precipitation falling onto the land surface can be transported by evapotranspiration or runoff, either as surface runoff or groundwater flow (figure 3.1). Surface runoff and groundwater flow discharge water back into the ocean, but the residence time of the water on the continents vary depending on its flow path (Alley et al., 2002). How the water is transported on the land surface depends greatly on the climate and the degree of permeability for the surface (Hiscock and Bense, 2014). In humid climates where the permeability is relatively high greater volumes of water will contribute to groundwater recharge and flow. While in airid climates with low permeability surfaces a bigger fraction of precipitation will be transported by direct runoff. Water can be stored in lakes, glaciers and groundwater and it interacts with the geological materials on Earth (Dingman, 2002).

3.1.2 Urban Hydrogeology

Anthropogenic influence cause changes on the natural hydrological cycle (figure 3.1) (Schirmer et al., 2013). Due to an increase in impervious surfaces recharge through infiltration of precipitation is reduced, and evapotranspiration is reduced (Vázquez-Suñé et al., 2005). But recharge may occur through losses in water supply and sewage that flows in pipes underground (Vázquez-Suñé et al., 2005). As direct infiltration is

reduced there is more available water for surface runoff. The response is greater volumes of water in drainage pipes, rivers and other flow paths (Booth, 1991), and the water volume may easily exceed the capacity of the flow conduits and the risk of flooding and damage to infrastructure increases. Another big influence on the urban hydrology is groundwater wells and energy wells. Exploiting groundwater in energy wells to harvest the thermal energy form the earth is a fast growing technology, but the extraction and injection of groundwater during Underground Thermal Energy Storage (UTES) may influence of the local groundwater flow pattern (Bonte et al., 2011).

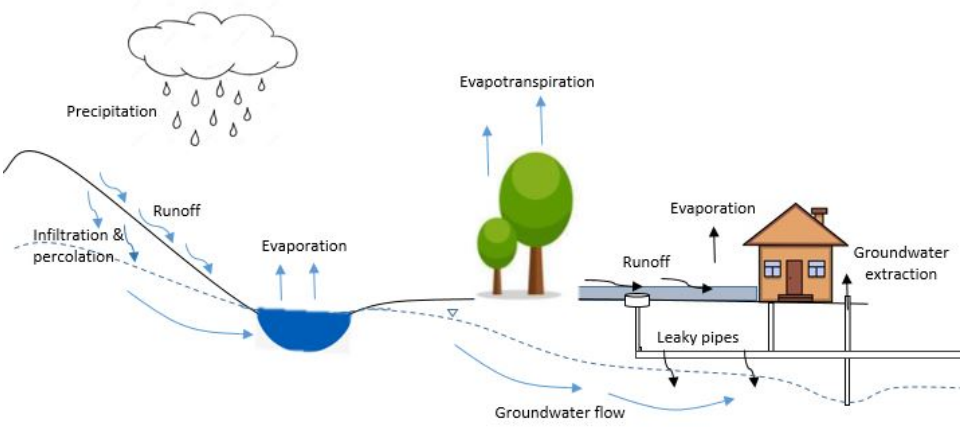

Figure 3.1: The urban hydrogeological cycle and the processes that drive it. Natural processes are indicated with blue arrows, while anthropogenic influenced processes are represented by black arrows.

3.2 Groundwater Flow

Groundwater flow is driven by gradients in hydraulic head. The total discharge Q, or volumetric flow rate, in a groundwater system can be described by Darcy's Law (eq. 3.1) (Darcy, 1856 ; Hiscock and Bense, 2014).

$$Q = -KA\frac{dh}{dl} \tag{3.1}$$

Groundwater flows in the direction of decreasing hydraulic head. K [L/T] is the hydraulic conductivity of the material and A [L^2] is the cross-sectional area of flow (Hiscock and Bense, 2014). The hydraulic head (h) is defined as the gravitational head, and can be calculated as the sum of the water elevation (z) above a datum (normally meters above sea level) and the pressure head (ψ) (Freeze and Cherry, 1979):

$$h = z + \psi \tag{3.2}$$

The pressure head (ψ) can be expressed as:

$$\psi = \frac{\rho}{\gamma_w} \tag{3.3}$$

Where ρ is water pressure [M/LT^2] and γ_w is the weight density of water. The water pressure is given as force over an area and has the unit $kN/m^2 = kPa$. Pressure is commonly measured relative to atmospheric pressure so that in unsaturated soils $\rho < 0$ and $\gamma < 0$, while in saturated soils $\rho > 0$ and $\gamma > 0$ (Dingman, 2002). The groundwater table is at the level where $\rho = 0$ (atmospheric pressure) and the pore space below is fully saturated. In the capillary fringe, above the water table, the pores may also be saturated due to capillary forces. In the saturated zone, below the groundwater table, the pressure is positive and hydrostatic if there is no groundwater flow (Dingman, 2002).

When describing groundwater flow in three dimensions as it occurs in a regional aquifer system, the law of conservation of mass needs to be considered (Hiscock and Bense, 2014). For transient groundwater flow the law of conservation of mass requires that the rate of fluid mass flow into a control volume is equal to the time rate of change in storage for the same volume. In an aquifer the specific storage (S_s) is the volume of water that is released from a unit volume in the aquifer storage if there is a decline in the hydraulic head (Freeze and Cherry, 1979). If the fluid in the aquifer is considered incompressible and Darcy´s Law is applied the transient groundwater flow can be expressed as:

$$\frac{\delta}{\delta x}\left(K_x \frac{\delta h}{\delta x}\right) + \frac{\delta}{\delta y}\left(K_y \frac{\delta h}{\delta y}\right) + \frac{\delta}{\delta z}\left(K_z \frac{\delta h}{\delta z}\right) = S_s \frac{\delta h}{\delta t} \tag{3.4}$$

where x, y and z are the spatial coordinates, K_x, K_y and K_z are the respective hydraulic conductivities and t is time.

The compressibility of a material describes the change in volume (strain (ϵ)) when a stress (σ) is applied (Freeze and Cherry, 1979, p. 51). Compressibility is the inverse of elasticity and can therefore be defined as strain/stress ($d\epsilon/d\sigma$). For a confined aquifer there are two ways that water can be released. A reduction of the aquifer porosity may cause compaction, or the water itself can expand and cause the release of water (Hiscock and Bense, 2014). In a confined aquifer the water is under pressure and for the confiding unit above the aquifer this pressure will affect the pressure within the pores of the aquitard (NGF, 2017).

3.3 Pore Pressure and Settling

In a saturated soil the stress exerted on the soil can be expressed as the sum of the stress on the grain skeleton and the stress from the pore pressure (Janbu, 1970). The stresses exerted on a geologic material in a saturated state can be expressed through the principle of total stress, as defined by Terzaghi (1936):

$$\sigma_t = \sigma_e + \rho \tag{3.5}$$

Where σ_e is the effective stress [M/LT^2] and ρ is the fluid pressure [M/LT^2]. The effective stress can be seen as the grain skeleton supporting the structure of the material, and the fluid pressure is the pressure of water filling the pore space of the geologic material (Janbu, 1970). In a confined aquifer the total downwards stress (σ_t) on the aquifer is due to the overlaying material. This is supported by the upwards effective stress (σ_e) from the aquifer material and the water pressure (ρ) in the pores (eq. 3.5) (Hiscock and Bense, 2014). Sediments with high porosity, such as clays, have a greater potential of being compressed as a result of the total stress from overlying material (Hillis, 2001 ; Hiscock and Bense, 2014).

How the sediment responds to stress depends greatly on the grain size distribution, the sediment composition (porosity and saturation) and time since the stress arose (Jernbanekompeatnse, 2016). The terms drained and undrained describe to what extent these factors allow the pore water to move through the sediment. A material that acts drained will allow the water to move through it so that the pore pressure is the same before and after a stress period. While for an undrained material the low permeability prevents the pore water from flowing and pressure will build up (Jernbanekompeatnse, 2016). In an undrained material pore pressure will take long to return to initial pore pressure conditions after a stress period, and for sediment such as clay this may take decades (Janbu, 1970).

In a confined aquifer the water is able to flow due to the aquifers hydrologic properties and pressure gradients. For the aquitard situated above, the low permeability and porosity prevents fluid flow, but the aquitard properties allows pore pressure diffusion (Ricard et al., 2012). A change in an aquifers hydraulic gradient has the potential to affect the pore pressure in the confiding aquitard. When pressure increases linearly with depth it is known as hydrostatic pressure (NGF, 2017). If the pore pressure is above hydrostatic it is considered overpressured. Aquitards with very low permeability is commonly overpressurized due to the hydraulic pressure from the underlying aquifer. How the pressure in the aquitard is distributed can vary depending on pressure history and permeability differences in the sediment (figure 3.2). Lateral pore pressure migration through sediments happens when there is a lateral pressure gradient in the sediment (Mann and Mackenzie, 1990). Such a gradient can be caused by drainage of pore water in the aquifer.

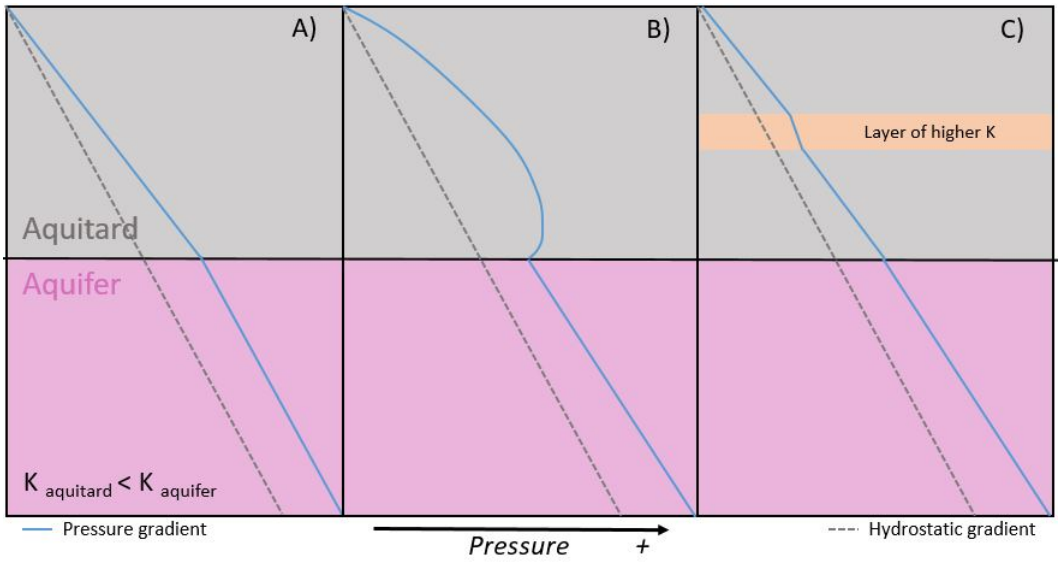

Figure 3.2: The hydraulic gradient in an aquifer unit affects the pressure gradient in the overlying aquitard. A) the pressure in the aquitard is overpressurized and linear, B) historically higher pressure has not yet dissipated through the aquitard, and C) the pressure gradient in the aquitard is affected by the presence of a more permeable layer. The black dotted line illustrate a hydrostatic pressure gradient.

The potential for sediment compaction depends on the load history on the sediment. The pressure that has previously existed is the preconsolidation pressure (p'_c), while the effective pressure (p_e) is the pressure present today (Janbu, 1970). If a clay sediment has an effective pressure equal to the preconsolidation pressure the sediment consolidation is due to the load of the sediment itself, and it is said to be normally consolidated (NC). While if $p'_c > p_e$ the sediment is considered over consolidated (OC) due to a previously present load. A heavily preconsolidated clay is less prone to cause settling due to changes in pore pressure.

Chapter 4

Method

4.1 Water Balance

When assessing the water balance in any catchment area several processes are present and a water balance equation is set up to represent the processes that account for inflows and outflows in the catchment area (Hiscock and Bense, 2014). The water balance equation is expressed as:

$$P = ET + S_R + G_g \pm \Delta S \tag{4.1}$$

Precipitation (P) includes rainfall, snowfall, freezing rain, sleet and hail, which accounts for inflow of water to the catchment. Precipitation as frozen water may cause delay and water retention, but this will not be taken into account when assessing the water balance in this study. Evapotranspiration (ET) includes both evaporation and transpiration from vegetation. Evapotranspiration and runoff accounts for the outflows of water in the catchment. In this study runoff includes both overland flow (S_R) and interflow (G_g). Change in storage (ΔS) over a defined period of time includes water quantity in groundwater and soil. When assessing the water balance in a catchment over long time periods, the net change in storage can be assumed to be zero (Dingman, 2002 ; Hiscock and Bense, 2014).

4.1.1 Catchment Area

Gaustad catchment area is part of the bigger catchment of Sognsvann. Gaustad river connects to Sognsvann river further down stream forming Forgner river. The catchment for Gaustad river has been generated using The Norwegian Water Resources and Energy Directorates (NVE) database NEVINA. To quantify the parameters of the water balance, data from Blindern meteorological station between the years 1957 - 2020 has been extracted from XGEO.no. XGEO generates surface runoff and evaportanspiration data from precipitation and temperature measurements, using the hydrologic model HBV (Seibert, 1996). Based on the average ET from XGEO,

the evapotranspiration is 55% of the yearly precipitation. The ET is considered to be over-estimated for an urban catchment, and based on the findings in Dupont and Mestayer (2006) the ET is assumed to be around 40% of P for the Gaustad catchment. The interflow (G_g) in the catchment is estimated based on the other parameters in table 4.1 by applying equation 4.1. The surface of Gaustad catchment is largely covered by urban surfaces and sediments of low hydraulic conductivity, such as clay, that is preventing precipitation from infiltrating. Parts of the runoff from tight surfaces is transported out of the system through the drainage system, but some will contribute to interflow and increase the G_g. It is assumed that recharge from precipitation occur in areas where bedrock is exposed (figure 2.2B).

Table 4.1: Yearly average measured P and T at Blindern meteorological station from 1957 - 2020. Average estimated ET and S_R from XGEO, where ET is corrected to be 40% of P. G_g is calculated by applying the water balance equation.

Parameter	Average yr (1957-2020)	1. standard deviation	2. standard deviation
P $[mm/yr]$	806.4	126.2	252.5
Daily T $[°C]$	5.6	1.1	2.3
ET $[mm/yr]$ -15%	378.6	64.7	129.4
S_r[mm/yr]	339.2	88.3	176.6
G_g[mm/yr]	88.6	47.5	95.0

It is assumed that the catchment area also defines the natural groundwater flow pattern to the study area. From figure 4.1 it is clear that the catchments in close proximity to the study area have a N-S orientation. The groundwater flow from Sognsvann catchment into the Gaustad catchment area is assumed to flow in from the north. The boundary of the Gaustad catchment does not coincide with Sognsvann lake, but due to the topography of the surrounding area it's assumed that groundwater flow in the aquifer, defined by the catchment area, is partly related to the groundwater flow and hydraulic pressure at Sognsvann lake. Figure 4.1 illustrates the piezometric surface along a profile going from Sognsvann lake to the bottom of the catchment area. The plotted values of the piezometric surface is based on borehole observations from energy wells from the Geological Survey of Norway database GRANADA. The model inflow and outflow boundaries are based on this data.

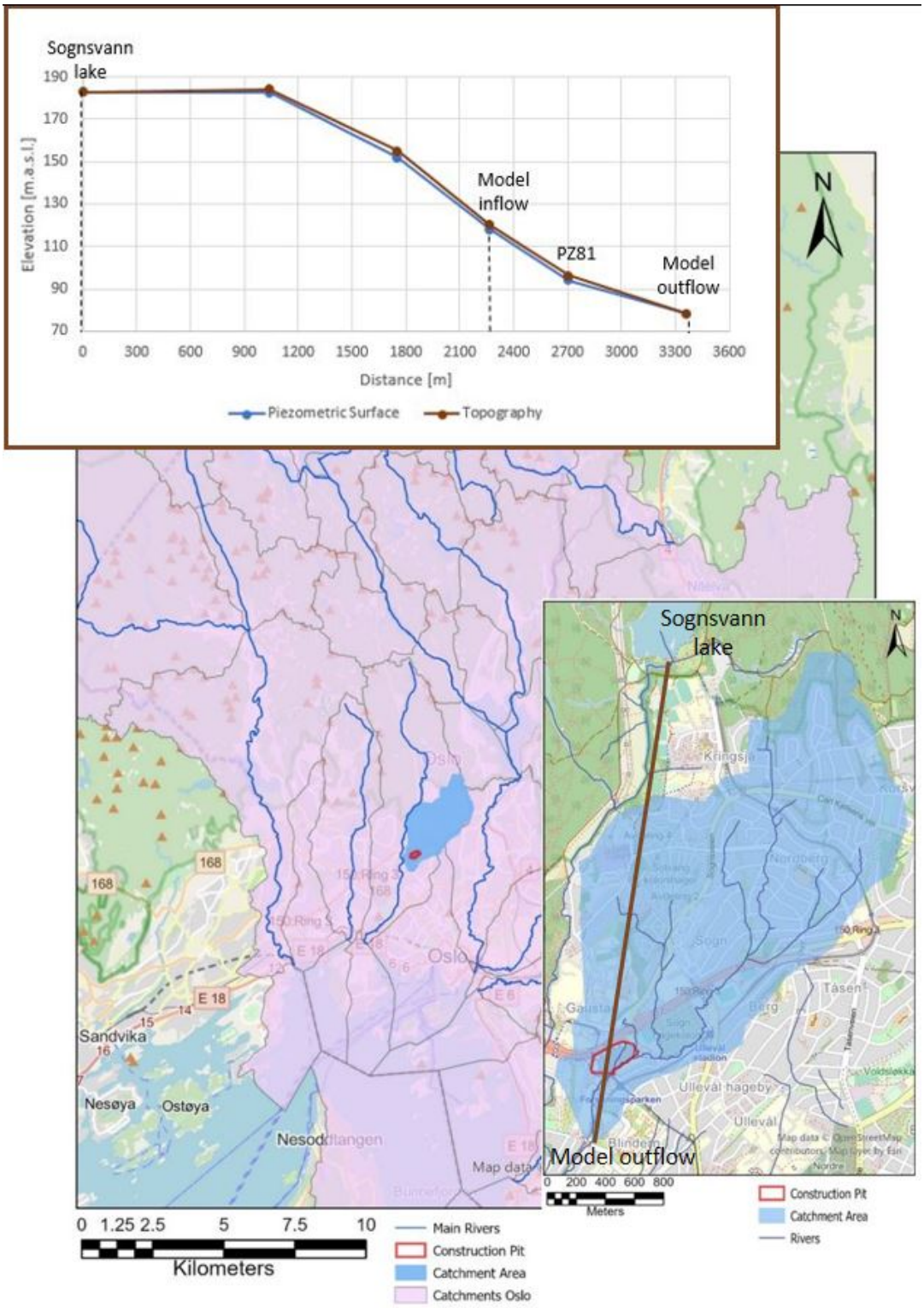

Figure 4.1: Overview of the catchments in Oslo and the catchment area for Gaustad river (blue). The orientation of the catchments surrounding Gaustad catchment area give an indication of the groundwater flow direction. The construction pit is located close to the outlet of the study area catchment. Datasets for catchments and rivers have been downloaded from The Norwegian Water Resources and Energy Directorate (NVE).

4.2 Water sampling

Temperature, pH and electric conductivity (EC) is measured continuously during water sampling from the boreholes in the construction area. When the field parameters are stable, the samples are collected. The groundwater is sampled directly from the hose into 15ml plastic tubes. The tube is filled to the top to prevent dissolution of gasses, which occurs due to reduced pressure conditions. Before capping the sample tube, 1ml of nitric acid is added to prevent dissolution of metals in the water.

4.3 Ion Chromatography

Ions dissolved in both surface water and groundwater can give information of the waters origin and pathway. The concentration of ions in the water is measured with an Ion Chromatography System (ICS-2000). In the ICS the ions are separated using two ion exchange columns and measured by using an electrical conductivity cell (DIONEX, 2006). The retention time of the ions are compared to known standards to identify them. The ICS is calibrated for known standards within a given detection range, and if the measured concentration is above this range the sample is diluted and measured again.

4.4 Numerical Modelling

To model the groundwater changes in the study area a finite-difference groundwater model is constructed using MODFLOW-2005 developed by the U.S. Geological Survey (USGS) (Harbaugh, 2005). The Groundwater Modelling System (GMS), developed by Aquaveo is used to visualize the data. To simulate groundwater flow MODFLOW-2005 uses a block-centered finite-difference approach. The model structure is built up of different packages that handles the hydrologic feature it is designed for. In this way the many features of the model can easily be considered and examined (Harbaugh, 2005). The conceptual model approach is applied to represent the hydrological features of the model. Further, to represent the heterogenity of the Quaternary sediments and the topography of the underlying bedrock the Solids tool in GMS has been utilized.

4.4.1 Model Setup

It is assumed that the general groundwater flow direction in the region is from the north towards the south. The modelled area is located at the bottom of the catchment, and the construction pit is located approximately in the middle of the modelled area. In this way the change of the aquifer piezometric surface can be modelled for the sensitive areas surrounding the construction pit.

Boundary Conditions

Inflow to the model area is defined as general head boundary in the north while the groundwater flow out of the model is represented by a changing head boundary on the southern border of the model (figure 4.2). The value for both general head and changing head is based on observations of hydraulic head during installation of energy wells, from the NGU database river is now open in the southern end of the model area. Three drains are defined; the fault line along the south-eastern border of the model area, the EPS fill and a drainage tunnel on the north-west side of the pit. Within the construction pit the sheet piling walls are represented as barriers with a very low conductivity (figure 4.2).

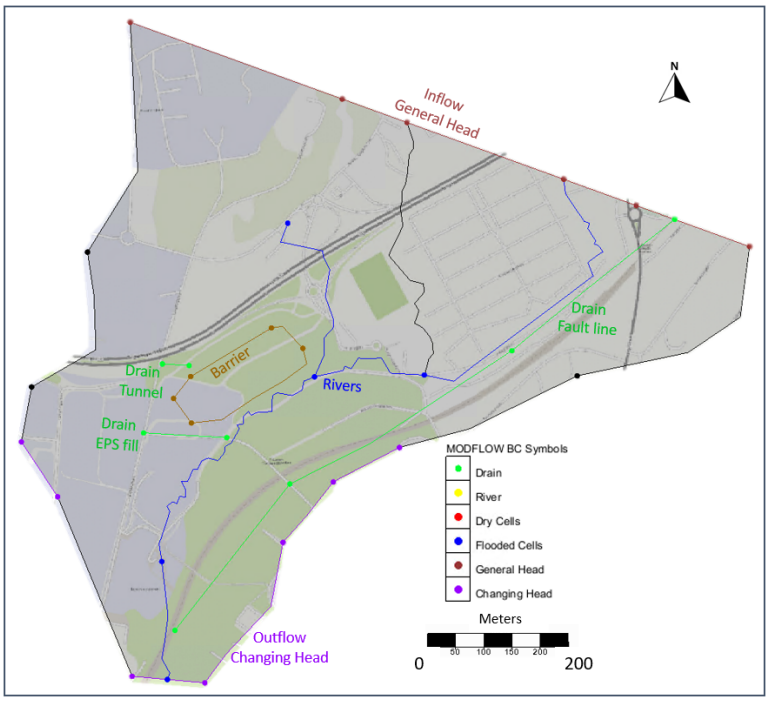

Figure 4.2: The local model area is defined by the boundaries of the catchment area. Historic rivers in the model area are represented as rivers below ground surface. The sheet piling walls surrounding the building foundation are set as barriers of low K.

GRANADA. The average groundwater level in energy wells surrounding the head nodes has been applied as hydraulic head values. The rivers and drains are defined using arcs, and the conductance of the arcs is defined as the conductance per unit length $[(L^2/T)/L]$. The historic rivers are mostly led thought pipes, but part of Gaustad

Stratigraphy

Based on interpretations from total sounding and CPTU, the model is constructed with multiple layers representing clay, silt and sand in the marine mud (figure A.3 - A.17). A basal moraine layer is defined between bedrock and the marine mud, and an anthropogenic layer is situated on top of the marine mud. The tool Solids to MODFLOW is used to interpolate layer data from total sounding and CPTU sampling points to construct a 3D

stratigraphy model of the model area (GMS, 2020b). The sampling points are represented as boreholes in GMS, where the top of each stratigraphic unit is numbered as a horizon. When the interpolated solids are transferred to the MODFLOW simulation grid in GMS the horizontal and vertical hydraulic conductivity of each stratigraphic unit is computed as a weighted mean for each grid cell (GMS, 2020a). In this way it is possible to represent thin, low permeability layers in the MODFLOW grid.

4.4.2 Sensitivity Study

To represent the interbedded silt and sand layers in the marine clay, averaged layers with a vertical thickness of minimum 0.2m is interpolated using the Solids tool. The true average layer thickness of the silt and sand is around 0.28m and 0.1m, respectively, and the lowest true vertical layer is 0.02m thick. Due to computational limitations in MODFLOW such thin layers are difficult to represent and an minimum layer thickness is applied. To test the model sensitivity related to sediment heterogenity model runs with three different hydraulic conductivity estimations are made. The first represents the marine mud stratigraphic unit with a K-value equal to that of clay. The second uses a weighted averaged K-value for the marine mud, based on the relative presence of clay, silt and sand. While in the last model run, layers with varying hydraulic conductivity are present (figure 4.3).

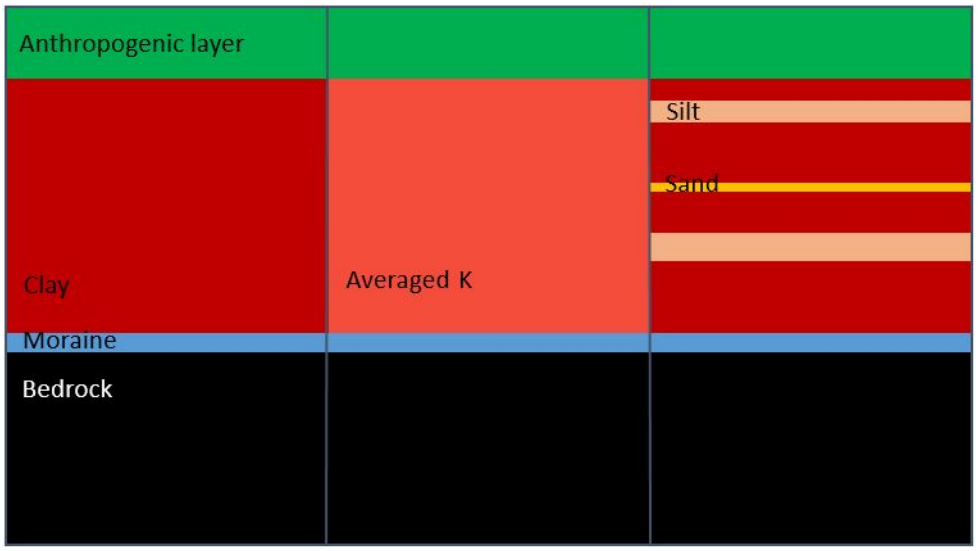

Figure 4.3: Three different statigraphic scenarios will be applied for the sensitivity study. The layer thicknesses are not true to the actual relative sizes.

4.4.3 Calibration

The steady state groundwater model is calibrated with regards to the hydraulic conductivity of the model layers. The calibration of the model

is preformed by using the hydraulic conductivity ranges in table 4.2. The model results are compared to the observed piezometric surface in seven piezometers. PZ81, PZ91, PZ92 and PZ93 are located directly outside the construction pit, while PZ68B, PZ90 and PZ94 are located around 100m away from the sheet piling walls. The model is calibrated for the steady state condition before construction started.

Table 4.2: Hydraulic conductivity ranges for model calibration. Values are modified from Freeze and Cherry (1979), Morris and Johnson (1967) & Tuttle (2020).

Layer	Hydraulic conductivity [m/s]	Hydraulic conductivity [m/d]	Porosity [%]
Anthropogenic fill	$10^{-6} - 10^{-8}$	$0.0864 - 8.64 \cdot 10^{-4}$	30
Clay (in situ)	$10^{-9} - 10^{-12}$	$8.64 \cdot 10^{-5} - 8.64 \cdot 10^{-8}$	42 - 60
Silt	$10^{-5} - 10^{-8}$	$0.864 - 8.64 \cdot 10^{-4}$	46
Sand	$10^{-3} - 10^{-7}$	$86.4 - 0.00864$	39 - 43
Basal moraine	$10^{-6} - 10^{-12}$	$0.0864 - 8.64 \cdot 10^{-8}$	31 - 34
Bedrock	$10^{-5} - 10^{-9}$	$0.864 - 8.64 \cdot 10^{-5}$	3 - 6

4.5 Risk Assessment

To assess the risk of settling due to pore pressure reduction the methodology presented in Piciullo et al. (2021) is applied. Piciullo et al. (2021) differentiates between ground-work induced soil deformation and building vulnerability. The soil deformation is viewed in a short- and long-term perspective, where the short-term displacement is considered as a function of soil type, type of retaining structure (related to construction), depth to bedrock and excavation depth and width. The long-term displacement is considered a result of an increase in effective stress due to pore pressure reduction. The impact of the displacement can be classified based on either the maximum vertical settlement ($\delta_{v,max}$) or the maximum rotation (θ_{max}) relative to the original orientation of the surface (table 4.3). The building vulnerability is determined based on an index reflecting the buildings susceptibility to damage. For the research questions in this study only the impact level of vertical displacement will be applied.

Experience data from Braaten et al. (2004) is applied to estimate the potential sediment compaction. In equation 4.2, $\delta_{v,ratio}$ is the ratio of the measured settling relative to the sediment thickness in the measuring point from figure 4.4, while $H_{marinemud}$ is the sediment thickness in the point of interest. $\delta_{v,3.75}$ is the potential sediment compaction in the point of interest, if the decline in piezometric surface is equal to the observation in figure 4.4. In equation 4.3, the potential sediment compaction in the point of interest ($\delta_{v,potential}$) is corrected for the observed decline in piezometric surface with the correction factor C.

Table 4.3: Classification of impact level based on vertical settling and rotation (Piciullo et al., 2021).

Impact Level	Settlement ($\delta_{v,max}$)	Rotation (θ_{max})
1. Negligible	< 10mm	< 1/500
2. Slight	10 - 50mm	1/500 - 1/200
3. Moderate	50 - 75mm	1/200 - 1/50
4. High	> 75mm	> 1/50

$$\delta_{v,3.75} = \delta_{v,ratio} \cdot H_{marinemud} \tag{4.2}$$

$$\delta_{v,potential} = \delta_{v,3.75} \cdot C \tag{4.3}$$

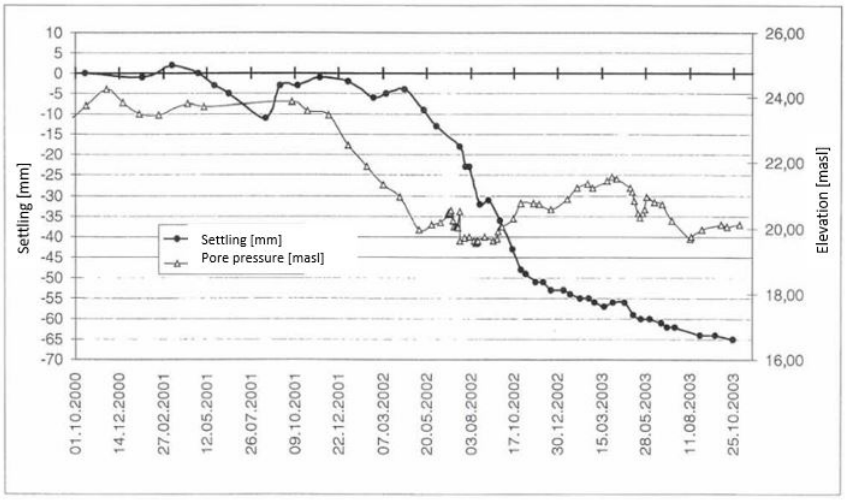

Figure 4.4: Observed pore pressure reduction in a 12m thick marine mud. The resulting vertical settling is -7mm for the observation period. Note that the settling is measured about 15m away from the piezometer. Modified from Braaten et al. (2004).

Chapter 5

Results

5.1 Groundwater Chemistry

Groundwater samples collected on August 27^{th} and October 1^{st} - 2^{nd} 2020 has been analyzed with regards to major ion concentrations. The results from the samples should be considered with care as it is recommended that three times the well volume is to be extracted before collecting groundwater samples. Neither of the groundwater wells was pumped to satisfy the recommendation before sampling. A summary of the field parameters, major cations and anions is listed in table 5.1, A.1 and A.2, respectively. Based on the measured field parameters for pH, the groundwater is considered alkaline. The temperature of the groundwater is stable at $10°C$, but the electric conductivity is higher in BH2 than BH3.

Table 5.1: Summary of field parameters for groundwater samples. BH1 was sampled on August 27^{th} 2020, while BH2 & BH3 was sampled on October 1^{st} - 2^{nd} 2020. BH1 was pumped during the field course GEO4369 and the data for field parameters was not measured.

ID	T [°C]	pH	EC [$\mu S/cm$]
BH1	-	-	-
BH2	10.0	8.67	1096
BH3	10.0	10.0	693

Figure 5.1 give the ion distribution in the three sampled wells. BH1 contain the highest relative concentration of chloride and calcium, while BH2 has the highest relative concentration of sulfate. In BH3 sodium, sulfate and chloride have a higher relative concentration than the other measured ions. Concentrations of salts in the sampled water are high (table A.1 & A.2). Calcium and chloride concentrations are greater in BH1 compared to BH2 and BH3. There is no detected ammonium and phosphate in any of the wells, and only low amounts of lithium in BH2 and BH3. The Cl/Br ration is 542 in BH1, 76 in BH2 and 118 in BH3 (table A.2).

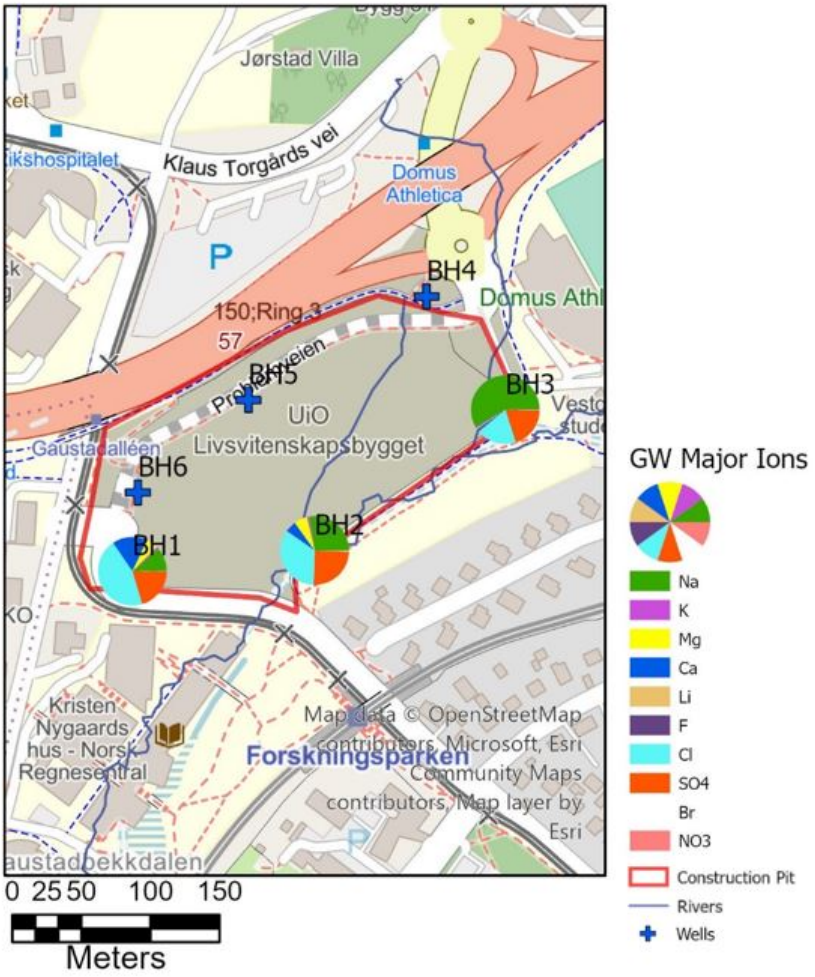

Figure 5.1: Sampling locations for groundwater taken 27^{th} of August and 1^{st} - 2^{nd} of October 2020. Relative concentrations of major cations and anions in the samples are based on the results in table A.1 & A.2.

5.2 Surface Water Chemistry

In relation with the course GEO4360, during fall 2020, river water in and around Gaustad river catchment was sampled. Four of the samples are from Gaustad river (G1 - G4 in figure 5.2), while three samples are from Sognsvann river before Sognsvann river joins Gaustad river (S1 - S3). The field parameters for the river water sampled in Gaustad river show a lower temperature, higher electric conductivity and pH, than in Sognsvann river (table 5.2). The sampling point furthest downstream at Gaustad (G4) have the lowest temperature and a higher electric conductivity compared to the sampling points upstream. The samples S1 & S2 have a higher temperature and significantly lower electric conductivity than the surface water sampled at Anne Maries vei (S3). All samples has been analyzed with regards to major ions, and a summary of the results are listed in table

A.3 & A.4.

Table 5.2: Summary of field parameters for river water samples. G1 - G4 are water form rivers in Gaustad Catchment, while S1 - S3 are sampled from Sognsvann River.

ID	T [°C]	pH	EC [$\mu S/cm$]
Solvang K (G1)	12.1	7.28	574
Konvallveien (G2)	13.9	7.81	412
Nils Bays vei (G3)	13.2	7.74	266
Blindern T (G4)	11.7	7.67	593
Sognsvann (S1)	16.6	6.75	45
Rikshospitalet (S2)	15.3	6.97	95
Anne Maries vei (S3)	13.9	6.94	1028

Generally, the concentration of ions increase down-stream in the rivers, but Gaustad river contains higher concentrations for all ions compared to Sognsvann river. None of the concentrations exceed the boundary levels in the Norwegian drinking water regulations (LovData, 2017). Calcium concentration in sampling point G1 is the highest of all measurements in river water, with 79.9 mg/L (table A.3). The Cl/Br ratio from river water samples from Gaustad river is 155 in sampling point G1, 96 in G2, 41 in G3 and 128 in G4. The same ration for samples in Sognsvann river is 19 in sampling point S2 and for S3 the Cl/Br ratio is 23 (table A.4).

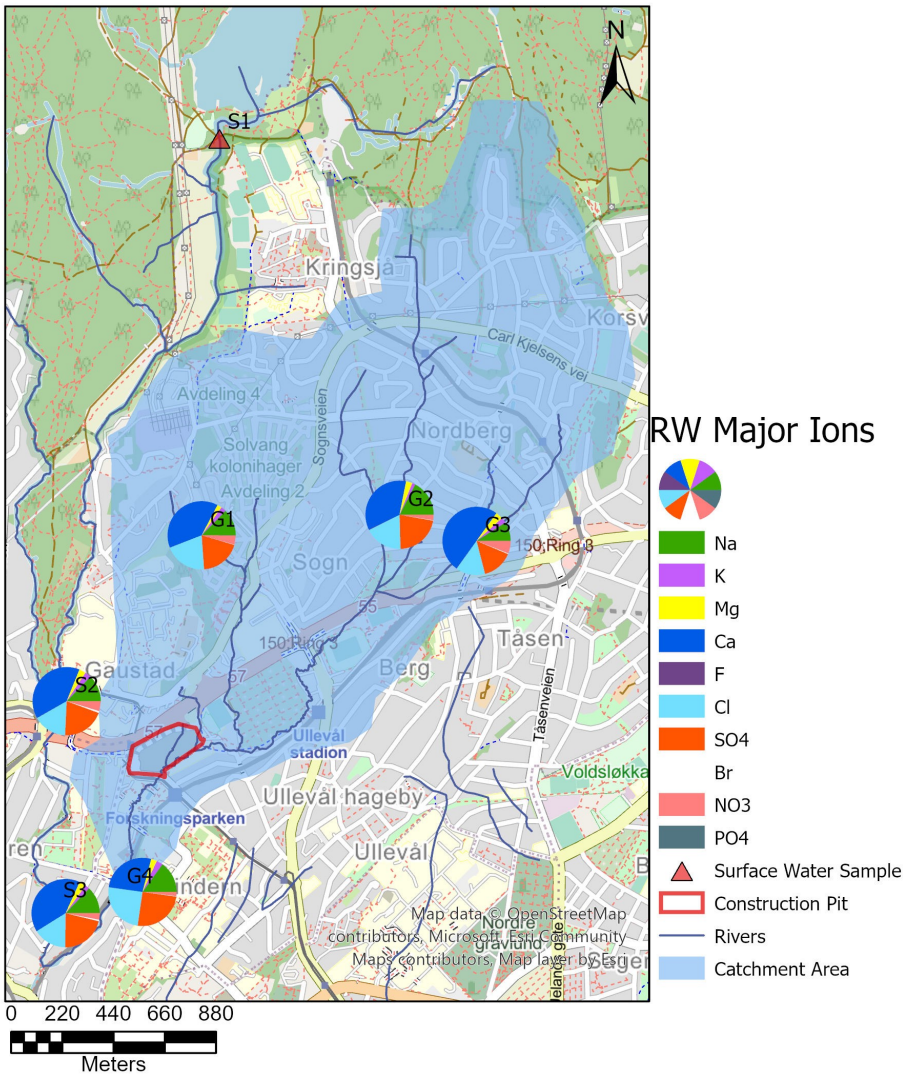

Figure 5.2: Sampling locations for river water taken 25^{th} - 31^{th} of August 2020. Relative concentrations of major cations and anions in the samples are based on the results in table A.3 & A.4. The sample S1 is not included as only major cations was measured.

5.3 Sediment Stratigraphy

The laboratory work and interpretations of the CPTU measurments done by Geostrøm AS have classified the marine sediment into five zones/sediment classes based on Fellenius and Eslami (2000) interpretation chart (figure A.3 - A.17) (VAV and Statsbygg, 2019). The interpreted stratigraphy has been simplified for the purpose of interpolating a 3D sediment coverage in MODFLOW. The simplified stratigraphy has three sediment classes: clay, silt and sand. The CPTU interpretations by Geostrøm AS does not include the full statigraphic unit in the z-direction, so an anthropogenic layer is assumed to be situated on top, while a basal moraine layer is assumed to be present between the marine mud and bedrock (VAV and Statsbygg, 2019).

Table 5.3 summarizes the average thickness of the layers in the boreholes that are interpolated to 3D stratigraphic units. Of the sediments that constitutes the marine mud (clay, silt and sand), clay is dominating the marine deposits. The presence of basal moraine is observed in some of the total soundings, but the extent of the layer is not fully mapped. For simplicity, when constructing the 3D sediment coverage in the model the moraine layer is continuous. Bjørvik (2021) has created a DEM of depth to bedrock for the catchment area of Gaustad, which has been applied to represent the bedrock topography for the areas further away from the construction pit. The models lowest point in the z-direction is set at 0 m.a.s.l.

Table 5.3: Average layer thickness and standard deviation from CPTU and total sounding. The layers have been interpolated for the whole model area.

Layer	Average thickness [m]	1. standard deviation
Anthropogen	3.04	0.63
Clay	9.41	10.53
Silt	0.28	0.50
Sand	0.10	0.08
Moraine	0.94	0.32
Bedrock	74.69	16.26

In areas were depth to bedrock is shorter the silt layers are thicker, such as in the north (T81 & PZ90) and south (T63) of the construction pit (figure 5.3). The silt and sand layers are pinching out towards the southeast (T68). In the center of the construction pit the silt and sand layers are very thin, with layers as thin as 0.02m in the z-direction. Relative to the average sediment thickness of the model area, the sand layers has the lowest presence. Sand only represent 0.4% of the sediment in the z-direction, silt is 2.6%, while clay dominates the sediment as 54% of the average sediment thickness.

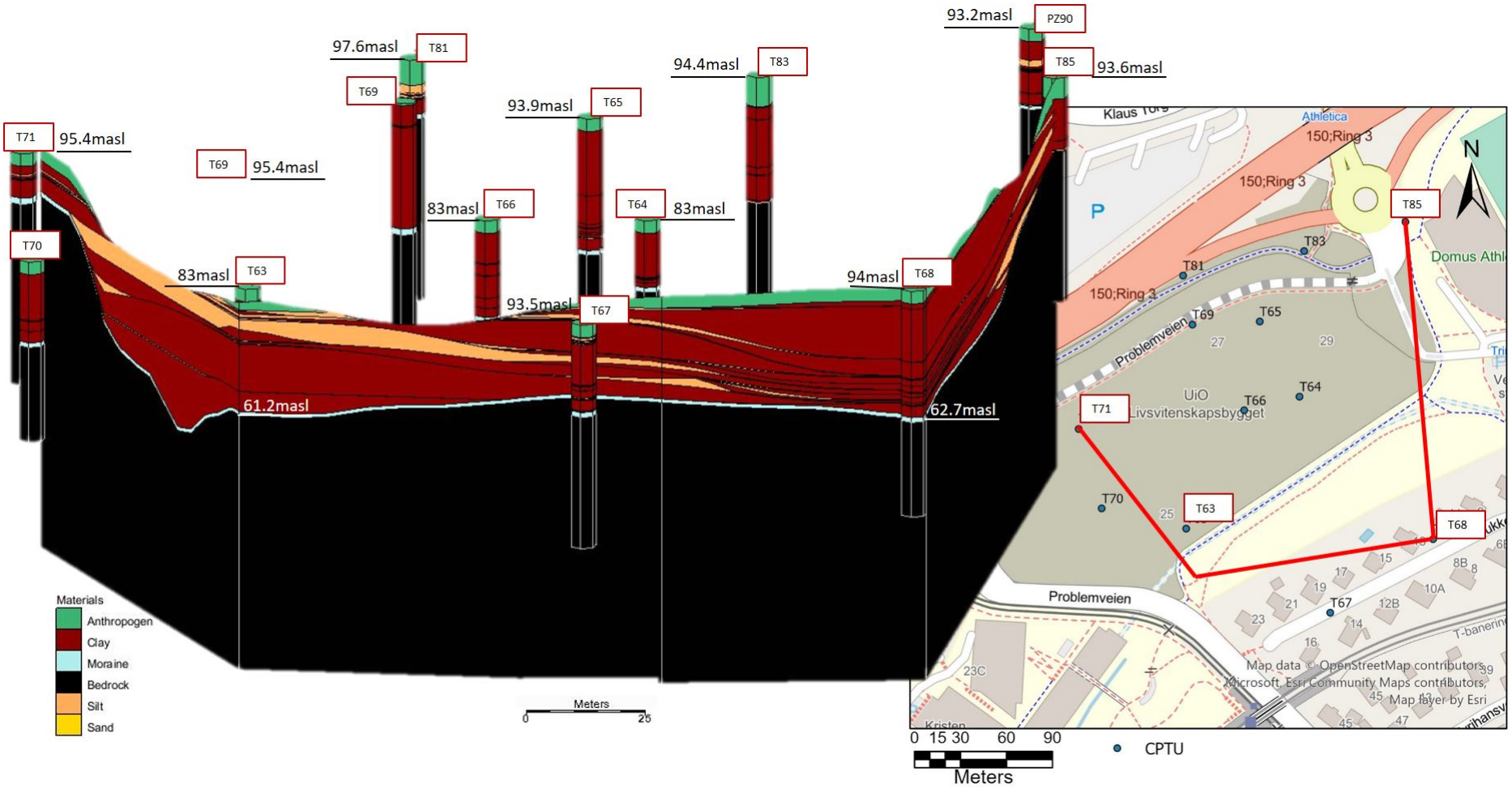

Figure 5.3: Interpolated stratigraphy displayed as cross-sections in GMS. Silt and sand layers are pinching out towards the south-east. The bottom of bedrock is set to sea level.

5.4 Groundwater Flow Model

The hydraulic gradient and groundwater flow through the model goes from the north to the south. The model results fit most of the observed piezometric values and the top layers of the MODFLOW grid is dominated by dry and flooded cells. Generally, the flooded areas are located closer to the model inflow boundary. The area of the construction pit has a flat surface and the surface elevation is lower relative to the surroundings. The construction pit is also flooded in the model results. The hydraulic properties of the model layers are listed in table 5.4.

Table 5.4: Hydraulic conductivity, vertical anisotropy (K_h/K_v) and porosity of the groundwater model.

Layer	Hydraulic conductivity, K_h [m/s]	Hydraulic conductivity, K_h [m/d]	K_h/K_v	Porosity [%]
Anthropogenic fill	$6.53 \cdot 10^{-7}$	$5.64 \cdot 10^{-2}$	7.8	30
Clay (in situ)	$1.04 \cdot 10^{-10}$	$9 \cdot 10^{-6}$	5.6	50
Silt	$7.69 \cdot 10^{-9}$	$6.64 \cdot 10^{-4}$	2.5	46
Sand	$1 \cdot 10^{-7}$	$8.64 \cdot 10^{-3}$	1.3	40
Basal moraine	$2.3 \cdot 10^{-10}$	$2 \cdot 10^{-5}$	3.6	34
Bedrock	$1.2 \cdot 10^{-5}$	$9.92 \cdot 10^{-1}$	1.5	3

5.4.1 Model Parameterization

The average piezometric surface for the model inflow and outflow in table 5.5 is calibrated within the 1. and 2. standard deviation. The length of the flow boundaries are equal to balance the water flow in and out of the model (figure 5.4). The conductance of the historic rivers are set to be relatively low as most of them flow in pipes. In scenario 1 & 2 the model is less sensitive to the river conductance, relative to scenario 3. The boundary condition for the drainage tunnel and the EPS-fill have a short spacial extent and only affects the areas in close proximity, while the drain representing the Blindern fault has a great influence on the hydraulic head in the whole modeled area.

Table 5.5: Averaged piezometric surface values at the model flow boundaries. Values are based on observed piezometric surface during installation of energy wells. Data of piezometric surface is gathered from the Geological Survey of Norway database GRANADA.

Node	Average Piezometric Surface [m.a.s.l.]	1. st. dev.	2. st. dev.
I1	127.63	0.41	0.82
I2	118.07	1.15	2.30
I3	96.67	1.15	2.30
I4	90.50	7.69	15.39
I5	92.00	7.69	15.39
I6	106.4	3.95	7.90
O1	95.37	1.56	3.12
O2	91.9	0.22	0.43
O3	73.50	-	-
O4	76.71	3.29	6.59
O5	91.53	0.73	1.45
O6	87.73	1.47	2.95
O7	97.45	0.15	0.30

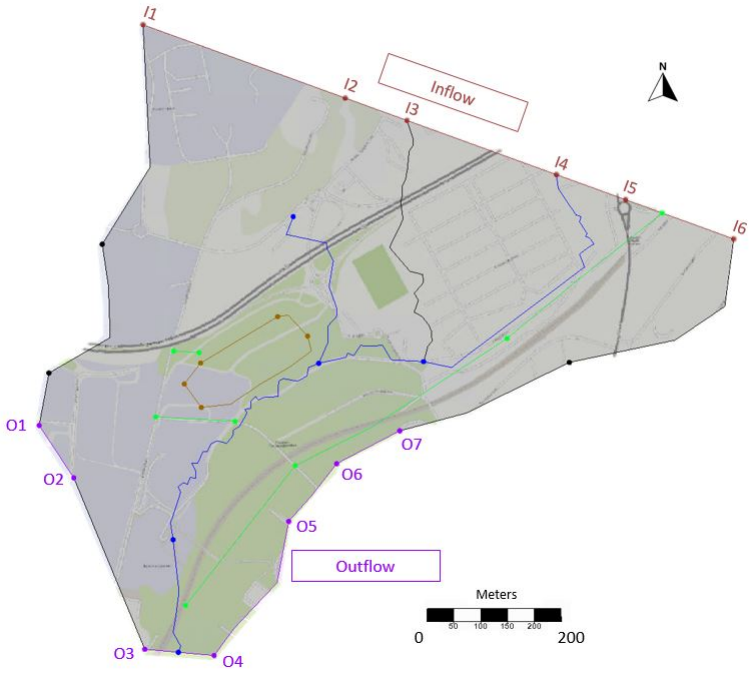

Figure 5.4: The model inflow and outflow boundaries.

5.4.2 Sensitivity Scenarios

In general, the bright red colored areas of the 3D groundwater model surface are dry cells, while the bright blue colored areas are flooded cells (figure 5.5). In all the three modeled scenarios, the area in the north of the model contains more flooded cells and the southern area contains mainly dry cells in the top layers. The areas were flooded cells are situated right under dry grid cells the model computes the hydraulic head to be above the top of the bottom cell, but the hydraulic head in the top cell is considered to be below the bottom of the cell.

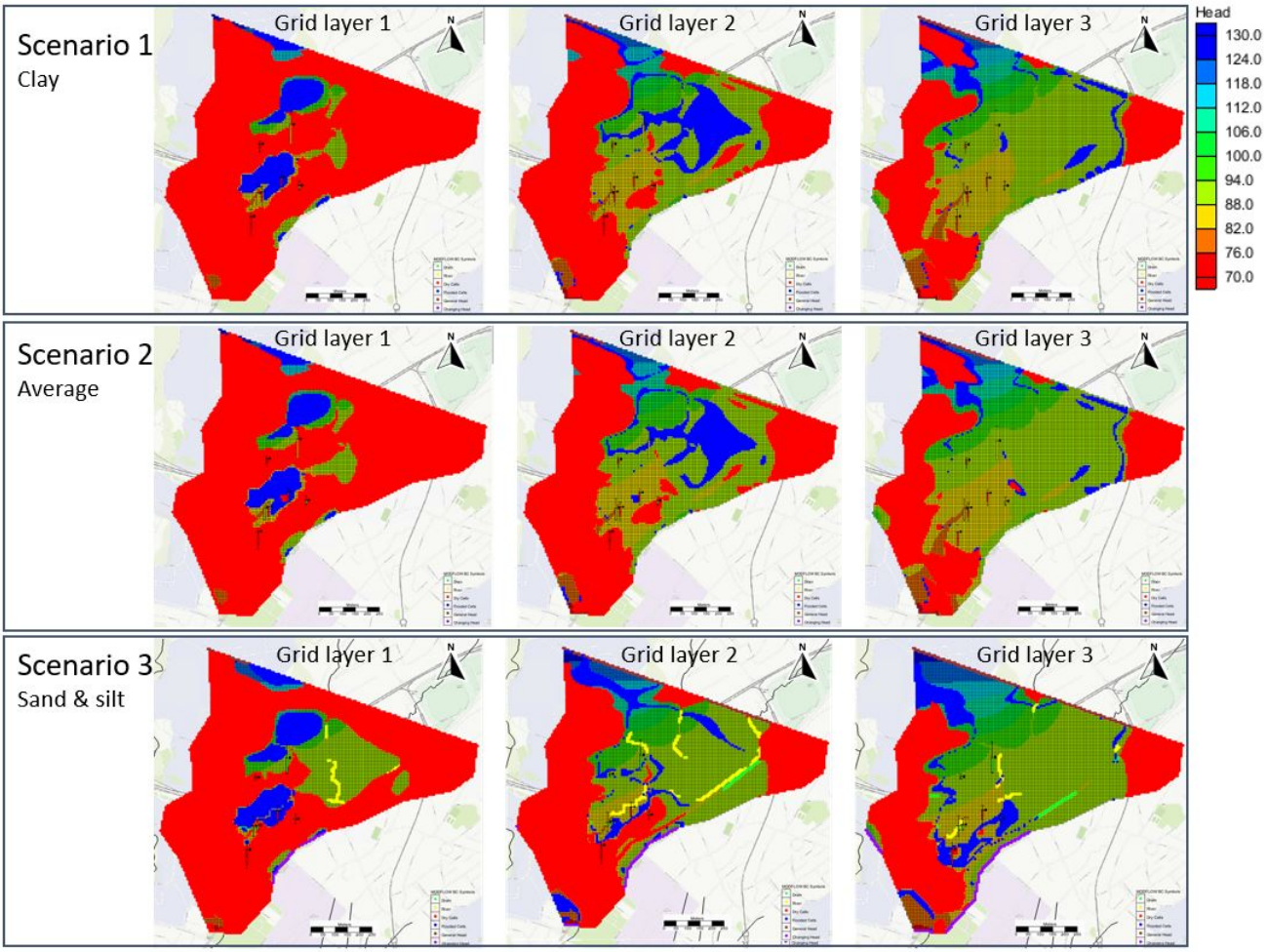

Figure 5.5: The three different model scenarios with the top three grid layers hydraulic head computations. The bright red color covering most of grid layer 1 in all scenarios are dry cells, while the bright blue are flooded cells. The simulated groundwater flow is from the north towards the south.

For the sensitivity study the hydraulic conductivity of the different startigraphic units are tested. It is apparent that the model is most sensitive to changes in the hydraulic conductivity of clay. In scenario 3, when slit and sand layers are represented in the stratigraphy, the model is more sensitive

to changes of hydraulic conductivity in the silt, relative to the sand. From table 5.6 & 5.7 it is apparent that the model is not sensitive to the change in hydraulic conductivity from scenario 1 to scenario 2. Relative to the computed hydraulic head in scenario 1 and 2, scenario 3 give the best fit simulation based on the observation points (table 5.8). The observation points with the lowest residual in scenario 3 is PZ68B and PZ81, while PZ90, PZ91 and PZ94 have the biggest residual hydraulic head. The same trend is present in the modeled scenarios 1 and 2. The biggest improvement in residual hydraulic head in scenario 3, relative to scenario 1 and 2, is in PZ92 and PZ93.

ID	Observed Head	Computed Head	Head Interval	Residual
PZ68B 29m	88.21	87.56	0.73	0.56
PZ81 13.7m	93.27	92.09	0.38	1.18
PZ90 16m	94.37	91.12	2.46	3.25
PZ91 24m	87.27	84.40	0.75	2.87
PZ92 25m	85.41	83.55	0.84	1.86
PZ93 37m	84.58	82.57	1.59	2.01
PZ94 24m	87.03	83.30	1.19	3.73

Table 5.6: The residual between the observed and computed hydraulic head for scenario 1. The residual value is only within the accepted head interval for PZ68B.

ID	Observed Head	Computed Head	Head Interval	Residual
PZ68B 29m	88.21	87.56	0.73	0.55
PZ81 13.7m	93.27	92.08	0.38	1.21
PZ90 16m	94.37	91.12	2.46	3.25
PZ91 24m	87.27	84.43	0.75	2.84
PZ92 25m	85.41	83.52	0.84	1.89
PZ93 37m	84.58	82.57	1.59	2.01
PZ94 24m	87.03	83.30	1.19	3.73

Table 5.7: The residual between the observed and computed hydraulic head for scenario 2. The residual value is only within the accepted head interval for PZ68B.

The computed hydraulic head in scenario 3 is displayed as north-south and east-west profiles in figure 5.6. The north-south profile intersects two observation points, PZ81 and PZ92. The hydraulic gradient from north to south follows the topography of the ground surface, it is steeper in the north. Flooded cells are present in an area just north of the construction pit, and in the pit itself. In the east-west profile the lower hydraulic head is present in the area of the construction pit, and an area further to the west were there is a drain (figure 5.6). The cross-sections in figure 5.7 display the extent of the model layers that are interpolated to the MODFLOW grid. In areas of the model were bedrock has a steep topography, the model has flooded areas.

ID	Observed Head	Computed Head	Head Interval	Residual
PZ68B 29m	88.21	88.28	0.73	-0.16
PZ81 13.7m	93.27	93.07	0.38	0.20
PZ90 16m	94.37	92.07	2.46	2.30
PZ91 24m	87.27	84.85	0.75	2.42
PZ92 25m	85.41	84.72	0.84	0.68
PZ93 37m	84.58	83.85	1.59	0.73
PZ94 24m	87.03	84.28	1.19	2.75

Table 5.8: The residual between the observed and computed hydraulic head for scenario 3. The residual value is not within the accepted head interval for PZ91 and PZ94.

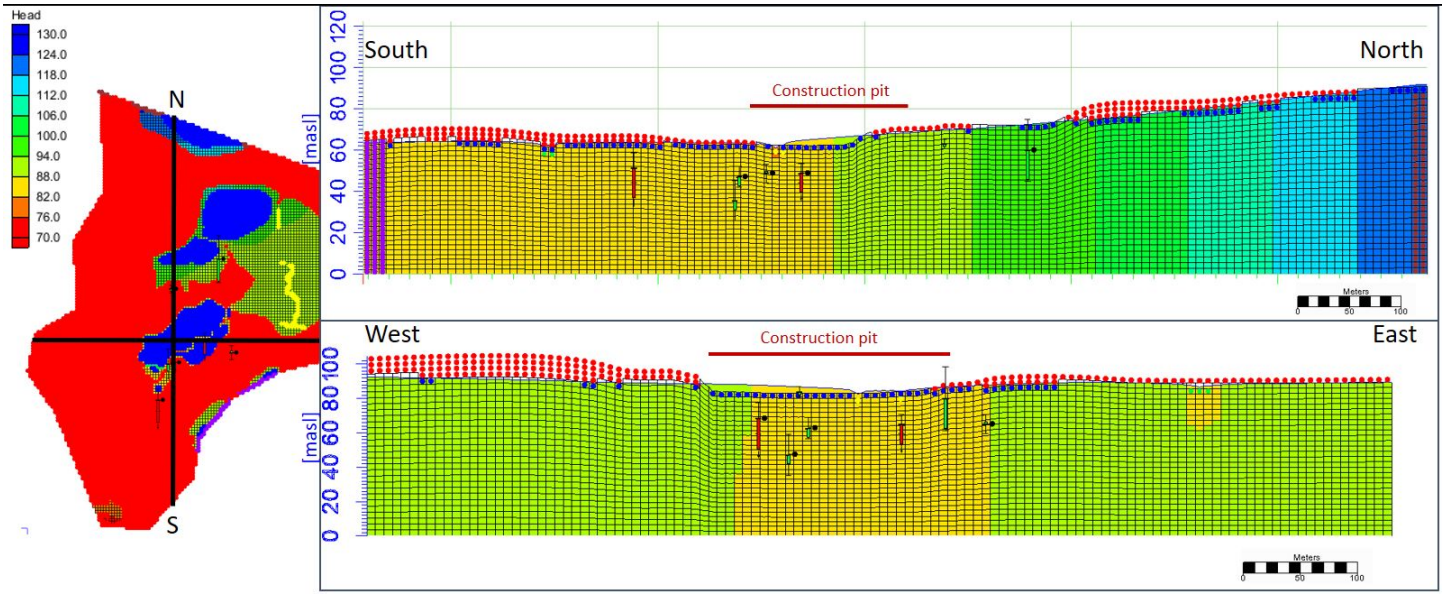

Figure 5.6: Profile of computed hydraulic head from north to south, and east to west, in the groundwater model. The hydraulic gradient is steeper in the north.

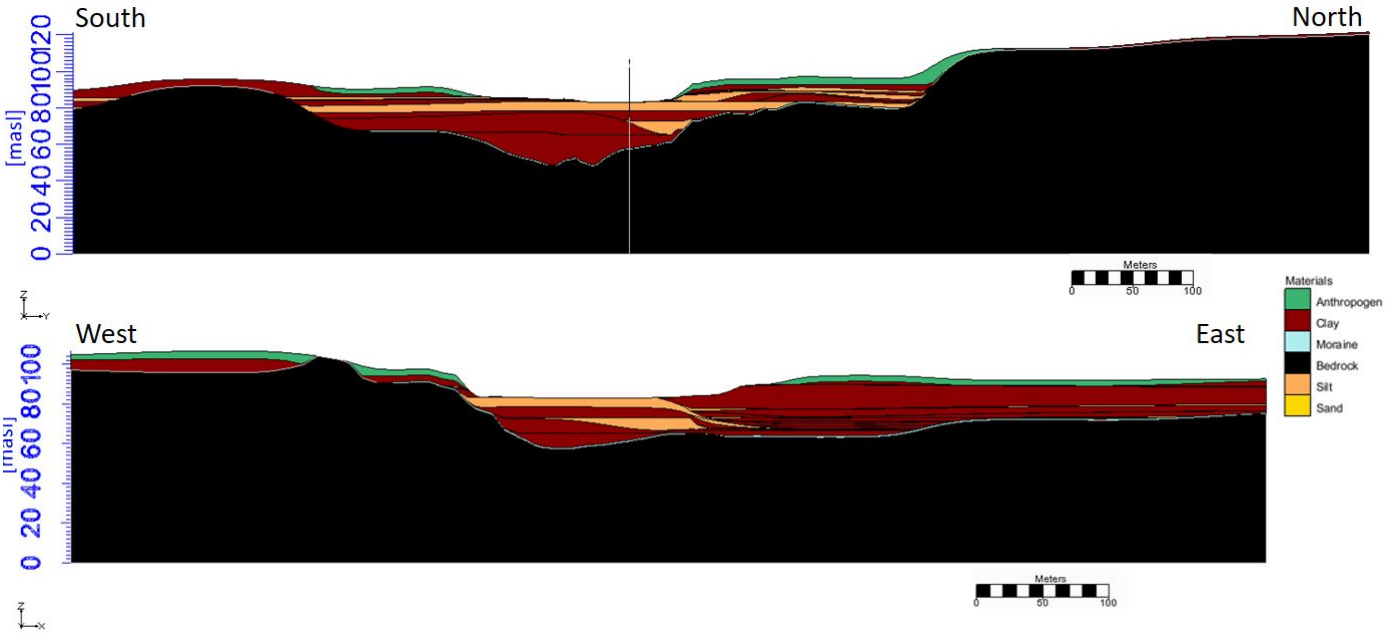

Figure 5.7: Cross-sections of the layers that are interpolated to the grid by using Solids to MODFLOW.

5.5 Pore Pressure Analysis

In each measuring point a shallow and deep piezometer is installed. The shallow piezomenters are positioned 8m below ground level, while the deep piezometers vary in depth depending on the depth to bedrock. The pore pressure data from April to December in 2019 has been applied as reference for pore pressure conditions by Hognestad and Tuttle (2020). The general trend for all pore pressure measurements is a decrease from the hydrological year 2020 to 2021 (table 5.9). Relative to the reference pore pressure from 2019, most of the pore pressure measurements have a decreasing trend, while one of the shallow piezometers show a slight increase in pressure. The greatest changes are present in the deeper part of the marine mud, close to bedrock (table 5.9). From figure 5.9 &

Table 5.9: Change in average pore pressure (ΔP) and piezometric surface (Δh). The change from the hydrological year 2020 to 2021, and from the reference year 2019 to 2021, show a decreasing trend for all the deep measurements and most of the shallow measurements.

ID	2020 - 2021 ΔP [kPa]	2020 - 2021 Δh [m.a.s.l.]	2019 - 2021 ΔP [kPa]	2019 - 2021 Δh [m.a.s.l.]
PZ68B 8m	-0.19	-0.02	-0.46	-0.05
PZ81 8m	-0.08	-0.01	1.55	0.16
PZ90 8m	-2.76	-0.28	-7.47	-0.76
PZ91 8m	-5.89	-0.60	-11.62	-1.18
PZ92 8m	-0.87	-0.09	-3.95	-0.41
PZ93 8m	-1.94	-0.20	-6.60	-0.68
PZ94 8m	-3.01	-0.31	-0.48	-0.05
PZ95 8m	-0.96	-0.10	-2.49	-0.26
PZ68B 29m	-6.87	-0.70	-5.68	-0.58
PZ81 13.7m	-12.85	-1.31	-14.77	-1.55
PZ90 16m	-6.42	-0.65	-9.60	-0.98
PZ91 24m	-9.12	-0.93	-6.98	-0.71
PZ92 25m	-9.00	-0.92	-8.44	-0.86
PZ93 37m	-12.75	-1.30	-15.88	-1.62
PZ94 24m	-11.87	-1.21	-9.95	-1.02

5.10 it is clear that the pressure in the top of the marine mud fluctuates more trough the year. In the deeper piezometers the measured pore pressure is in the ranges from 70 - 370kPa, where the lowest pressure is in PZ81 and the highest in PZ93. The pore pressure in PZ93 & PZ94 close to bedrock follows the same variations through the hydrological year, but in contrast the pressure at the same shallow piezometers have great differences. The shallow pressure in PZ94 fluctuates slowly through the year in both figure 5.9 & 5.10, while PZ93 measures sudden drops in pore pressure. The pore pressure in the deep piezometers in PZ91, PZ92 and PZ68B is stable at around 215kPa and has the same small fluctuations through the hydrological year. The same fluctuations can be observed

in PZ93 & PZ94 as well, but with different magnitudes of pressure. The shallow piezometers PZ81, PZ91 & PZ94 all measure higher pore pressure shortly after months with greater volumes of precipitation (figure 5.11). The same is observed in PZ92 & PZ95, but the pore pressure fluctuation has a higher frequency. Averaged values of the pore pressure evolution during the hydrological year 2020 and 2021 is summarized in table A.5 & A.7, respectively. The 1^{st} & 2^{nd} standard deviation (σ) indicate the fluctuations in pressure and the piezometric surface within the respective hydrological years. The greatest fluctuations are in PZ92, PZ93, PZ94 & PZ95, all located in the southern end of the study area.

Figure 5.8: Variations of the piezometric surface (Δh) in PZ81 and PZ93, close to bedrock, from 2019 to June 2021.

Figure 5.8 highlight the evolution of the piezometric surface in the two piezometers that experience the greatest change relative to reference. Located just north of the construction pit, PZ81 measures a decline in Δh close to bedrock of 1.55m. While in the south end of the area the Δh decline close to bedrock is 1.62m for PZ93.

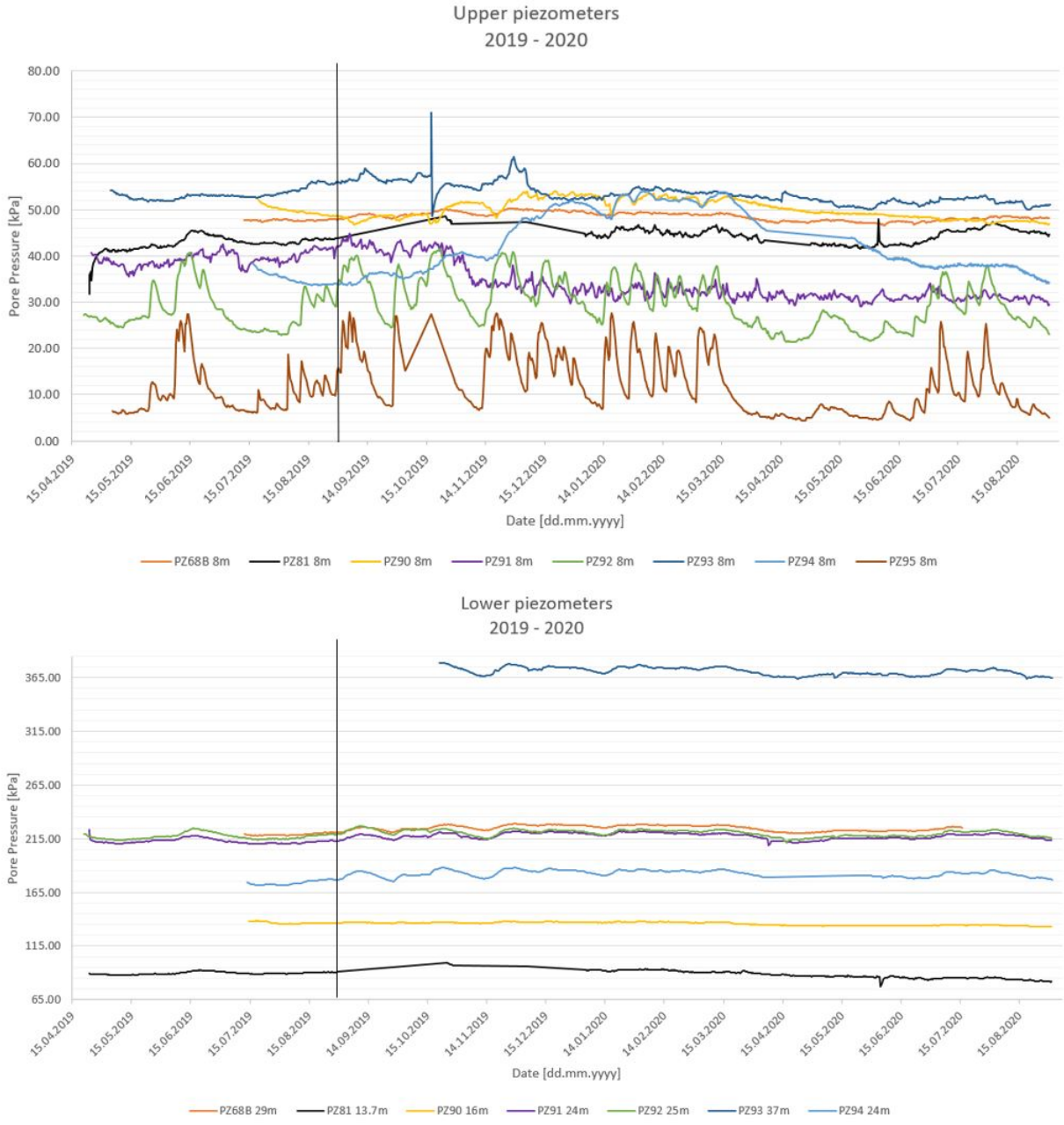

Figure 5.9: Pore pressure in both the shallow and deep piezometers for the hydrological year 2020. Average pore pressure from April to September 2019 has been applied as reference pore pressure by Hognestad and Tuttle (2020). The vertical black line marks the start of the hydrological year.

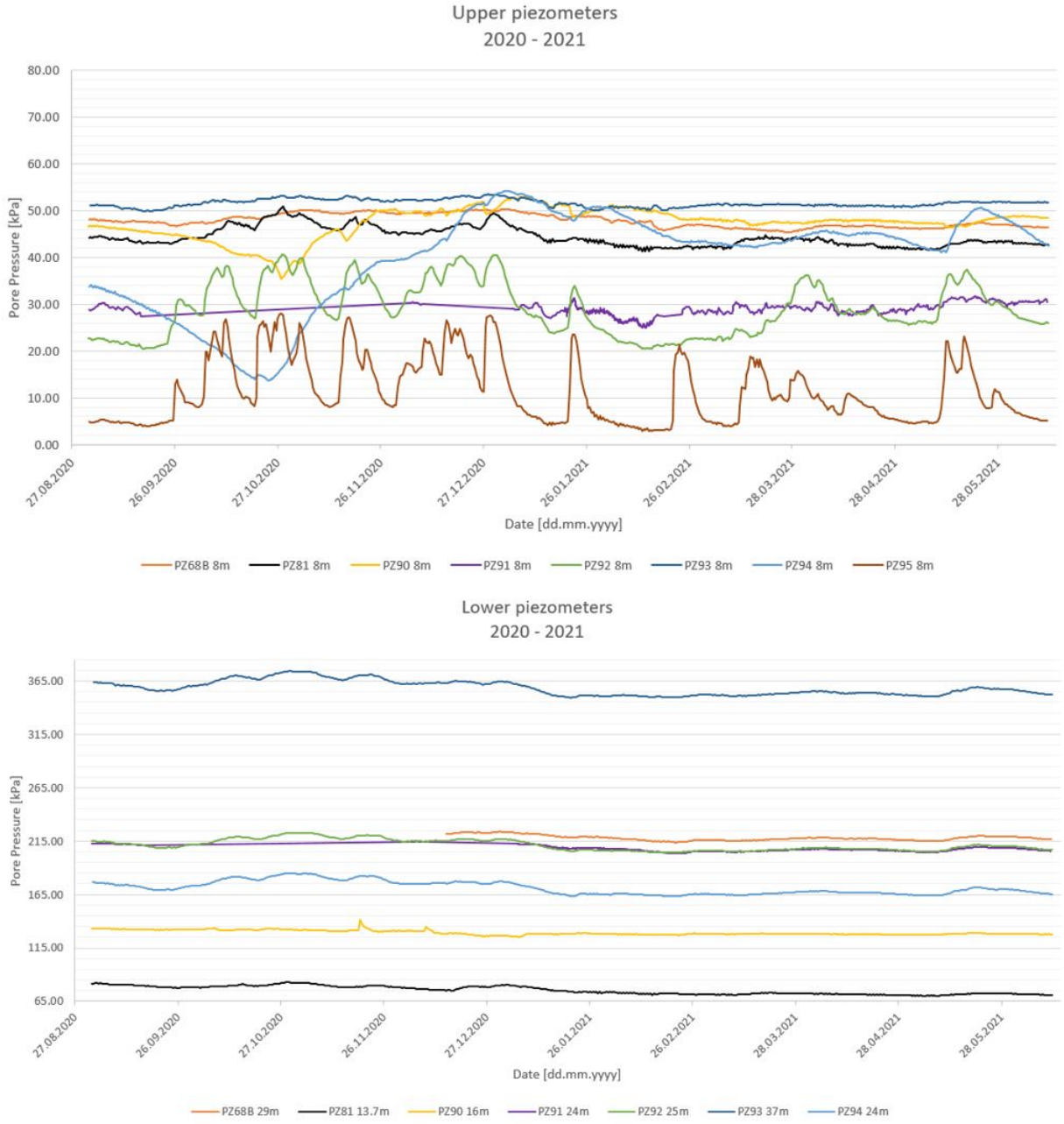

Figure 5.10: Pore pressure in both the shallow and deep piezometers for the hydrological year 2021.

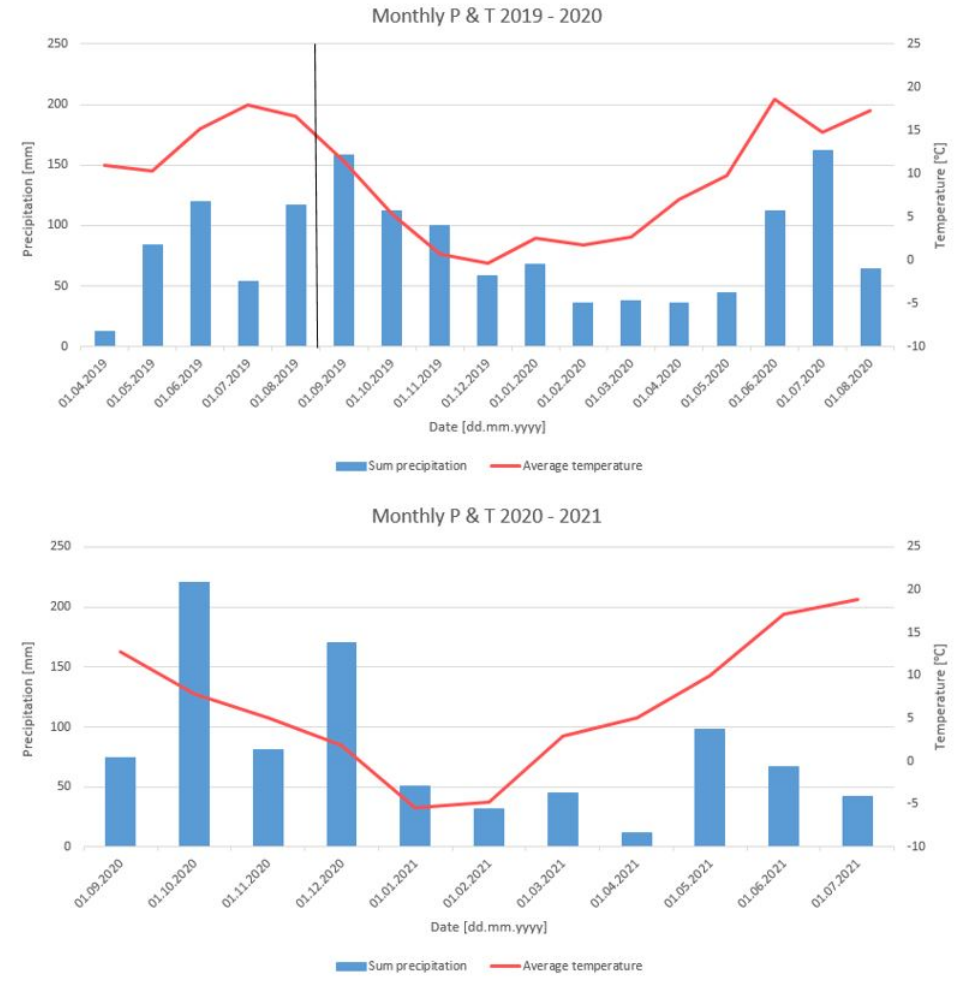

Figure 5.11: The sum of monthly precipitation and average monthly temperature at Gaustad. The vertical black line in the top plot marks the start of the hydrological year. Meteorologic data for Blindern is gathered from XGEO.no.

The Limiting Damage (Bergens Skade) project has gathered data from several sites were ground work such as deep excavations and foundation work has been preformed in clay (Karlsrud et al., 2015). In figure 5.12, the decrease of the piezometric surface (Δh) is normalized to the excavation depth below the original ground water level (H_{max}). The data points for the Life Science Building have a relatively low normalized value, indicating that Δh is low, compared to data from the case studies in Karlsrud et al. (2015).

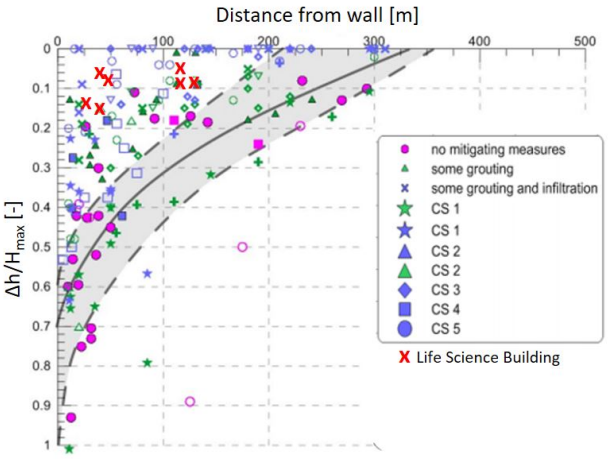

Figure 5.12: Normalized decrease of piezometric surface ($\Delta h / H_{max}$) observed close to bedrock relative to distance from sheet piling walls. Modified from Karlsrud et al. (2015). Data points in red are from the Life Science Building, while the rest are from Limiting Damage Case Studies (CS).

Braaten et al. (2004) studied the pore pressure evolution and settling in relation to construction of an underground railway tunnel from Sandvika to Asker. The Quaternary geology present in Gaustad is similar to that of the construction area studied by Braaten et al. (2004), with a basal moraine situated underneath a cover of marine mud. In figure 4.4 the pore pressure reduction measured close to bedrock is -3.75m, while the resulting sediment compaction is -7mm. Relative to the vertical thickness of the marine mud the settling ratio, $\delta_{v,ratio}$, is 0.000583. The thickness of the marine mud in PZ81 is 13.7m, while in PZ93 the marine mud is 37m thick. After correcting for the observed decline in piezometric surface in PZ81 and PZ93 the estimated settling potential is -3.3mm and -9.3mm, respectively.

Chapter 6

Discussion

6.1 Groundwater Flow Model

The sensitivity study illustrate the importance of constructing a model that represent the true conditions in the best possible way. Model scenario 1 and 2 could possibly give a satisfactory simulation of the natural condition with further calibration, but the hydraulic conductivity distribution in scenario 3 give more realistic simulations. The lateral extent of the more permeable silt and sand layers causes the marine mud to be more susceptible to the hydraulic pressure from the fractured aquifer. A simplified model with homogenic layering will not be able to simulate the complex nature of the study area. PZ90, PZ91 and PZ94 have the biggest difference between observed and computed hydraulic head in all three scenarios. The pore pressure in these areas is likely more affected by other factors than the marine mud stratification. These three observation points are situated in areas with a bigger relative presence of marine clay. In the area of PZ 92 and PZ93 the marine mud has a higher presence of silt and sand. The improvement of residual hydraulic head in PZ92 and PZ93 in scenario 3 demonstrates how the startification better the model results.

The construction of a structured MODFLOW grid assumes a horizontal and continuous aquifer (Harbaugh, 2005). The topography of the study area, and the underlying fractured aquifer, makes the computations in the model challenging. The steep valleys in the bedrock topography causes an elevation difference in horizontally adjacent grid cells which may be the cause for the flooded areas in figure 5.6. To prevent MODFLOW from computing dry cells in the top grid cells the model grid should have been set up with the grid cells at the top to be longer in the z-direction. In this way the top grid cell would cover the vadose zone and the very top part of the saturated zone. This could potentially also better the model in relation to flooded areas. To construct a grid that is not dependant on the topography of the different startigraphic units is challenging in GMS and was not successful for this study. Applying Solids to MODFLOW to interpolate the hydrological units in the study area is fitting for the sedimentary deposits, while the anisotropic nature of the bedrock is poorly represented. Further,

the Soilds to MODFLOW method does not interpolate vertical geological formations such as dikes. The syneite that is present in the borehole logs from BH1 & BH6 is therefore not included in the model.

6.2 Urban Groundwater

Groundwater in Norway holds a relative stable temperature through the year, at around $10°C$, which is observed in groundwater samples from Gaustad. The river water in Gaustad river holds a lower temperature, which indicates a bigger influence of groundwater, compared to Sognsvann river. The lower temperature in sampling point G4 (table 5.2) relative to the sampling points further upstream gives an indication that Gaustad river may be effluent at this point. The temperature in Sognsvann river has a typically season dependent temperature, and the river is not affected by groundwater. Normally, rainwater has a pH of about 5.6, and surface water may have a more neutral pH due to interactions with geological materials (Freeze and Cherry, 1979). A higher pH in samples from Gaustad river is most likely due to the river water being neutralized by the limestone in the Chambro-Silurian bedrock, both from interfering on the surface and groundwater mixing. The alkalinity of the groundwater from the wells in the construction site (table 5.1) may be caused by the stabilizing lime-cement mixture. The mixture is known to from a alkaline solution with water (StatensVegvesen, 2014).

In an urban environment there are many factors that influence the groundwater level and flow pattern. Bonte et al. (2011) states that the groundwater levels and fluxes almost always changes during UTES. The groundwater level is lowered around extraction wells, forming a cone of depression. While around infiltration wells the water table is elevated. For a confined aquifer, like the one at Gaustad, the effect will likely give a reduction in pore pressure in the aquitard at the extraction wells, and a pore pressure increase close to the infiltration wells. Despite UTES not actually removing groundwater from the system, it may still affect the local fluxes and cause a potential for settling in areas where the aquitard pore pressure is reduced.

6.2.1 Contaminant Sources

Contamination of surface and groundwater can originate from point sources and non-point sources, as described in Ritter et al. (2002). Examples of non-point sources are agricultural runoff, storm-water and urban runoff, but it may be difficult to distinguish between the point source and non-point source contamination (Ritter et al., 2002). Due to the fact that the water sampling in this study was only carried out one time, the results need to be considered with care as it may not be truly representative.

For the major ions analyzed in the river water, all are within the acceptable limits defined by the Norwegian drinking water regulations (LovData,

2017), but other sources of contamination may need to be considered before the river water can be classified as safe to drink. Heavy metals, organic material, bacteria and viruses also affect the water quality, and analyzing the river water for organic matter and bacteria, such as E. coli, may give a better indication of the potential presence of waste and sewage water.

The Norwegian Institute of Public Health (FHI) states that most surface waters in Norway are considered soft water, due to a Ca concentration below 15 mg/L (FHI, 2021). The river- and groundwater analyzed in this study is considered hard water (table A.1 & A.3). Dissolving of limestone nodules in the Cambro-Silurian bedrock may be the cause for higher Ca concentration in the water in Oslo. Other sources of Ca may be road salt ($CaCl_2$) or the solutes from the limestone cement used for stabilizing the construction pit. The high concentrations of salts in the groundwater may be due to leaching of ions from seawater in the marine mud. The higher concentration of sulfate in the groundwater samples (table A.2) and river water in G3 (table A.4) may be due to an input of sewage water in the area, or natural sources such as presence of sulfate and sulfur in the soil or bedrock. The conservative ions Cl^- and Br^- can be an indication for the source of salt in the water. The Cl/Br ratio in Standard Mead Ocean Water (SMOW) is about 288, and a Cl/Br ratio higher than the SMOW indicate that the source of salt is from mixing with waste waters, while a ratio lower than the SMOW indicate an influence from agriculture (pesticides and fertilizers) (Nair et al., 2013). From the Cl/Br ratio in BH1 it is possible to argue that the source of salt is from waste water, while for BH2 & BH3 an agricultural influence may be the source of salts. Further work is necessary to determine the actual sources of ions in the surface and groundwater.

6.3 Pore Pressure evolution

From formerly installed piezometers in the construction area (PZ6 in fig. 2.1) the pore pressure in the marine mud is considered hydrostatic (Statsbygg and VAV, 2019), which indicates that the pore pressure conditions in the marine mud has been stable for a longer time period. The fluctuations in pore pressure for the deep piezometers reoccurs in the months after August, and stabilizes around January (figure 5.9 & 5.10). August is the month with highest average precipitation in the study area (fig. A.24). This illustrates how the pore pressure in the marine mud is affected by the recharge of the fractured aquifer situated below. The reference pore pressure is based on measurements from April to December 2019 for PZ81, PZ91, PZ92, PZ93 & PZ95, while for PZ68B, PZ90, & PZ94 the measurements started in July 2019. To get the best possible reference values the measurements should ideally have been gathered for a whole year, to get the natural variation through a hydrological year. A shorter data collection period causes room for error in the reference values that has been applied. To better the reliability of the reference pore pressure, the measurements for establishing reference values should take place before ground work is initiated.

Layers of different permeability within the marine mud gives potential for the pore pressure to migrate. The decrease in pore pressure that is observed from 2019 to 2021 has a greater magnitude in the clay close to bedrock. The low permeability of the marine clay prevents the pore pressure to diffuse through the sediment, but the presence of silt and sand will accelerate the pore pressure migration. The orientation of the silt and sand layers gives potential for lateral pore pressure migration and the pore pressure changes caused by construction can potentially affect buildings and infrastructure outside the construction area.

6.4 Settling Potential and Risks

Comparison of the normalized decrease in piezometric surface for the observations at LSB to observations from Karlsrud et al. (2015) case studies show that the normalized Δh values from LSB are within the lower ranges (figure 5.12). Based on experience from the previous case studies, grouting and infiltration close to bedrock is effective mitigation measures to prevent groundwater leakage along sheet piling walls and foundation piles. At the LSB construction site such measures have been applied during foundation work, and the low values for the normalized Δh indicate that the measures are effective. However, the pore pressure reduction that is present may still cause settling. Additionally, Langford et al. (2016) emphasize that the risk of leakage during installation of foundation piles is greater than for sheet piling walls. The foundation piles at LSB has not yet been installed and the total pore pressure reduction due to construction is likely to increase. A comparison of the reduction in piezometric surface at the LSB construction pit to the observations from Braaten et al. (2004) gives an indication of what effect the start of construction and installation of sheet piling walls have on the pore pressure in the marine mud. The decline in piezometric surface at Gaustad is less than in the study area of Braaten et al. (2004), and the potential for settling due to pore pressure reduction will be smaller. The individual study sites have different hydrogeological conditions and the data should be compared with care. The span of the normalized Δh in figure 5.12 is due to both the hydrogeological conditions and mitigation measures in each case study. Additionally, the dimensions of the construction pit and the construction method affects the potential pore pressure reduction (Langford et al., 2016). Further work is needed to give a more precise estimate for the settling potential of the marine mud.

A sediments potential to compact depends on the porosity and the load history of the sediment. If a sediment that is exposed to pore pressure reduction, or added load, is over consolidated the potential for settling is less (Janbu, 1970). A layer of clay with high porosity has a greater potential for compaction than an equally thick layer of silt, or sand, with lower porosity (Trask, 1931). Additionally, the total thickness of the sediment layer will affect the settling potential. A sequence of thick marine clay has the poten-

tial to settle more than a thin layer, due to the higher total pore space in the thick clay sequence. The parts of the study area with greater thickness of marine mud, have a higher potential for ground settling, relative to thinner sections of marine mud. The risk of differential settling is higher when the thickness of marine mud varies greatly within one area. The area south-east of the construction pit, close to Bukken Bruses vei, contains thick layers of marine clay with thin interbedded silt and sand layers. The marine clay has a high potential for sediment compaction over time due to the possibility of pore pressure migration through the silt and sand layers. The estimated settling potential for the marine mud in PZ81 and PZ93 illustrates the effect the different sediment thicknesses has in relation to differential compaction. The estimated settling potential does not consider the relative distribution of clay, silt and sand in the sediment. A higher presence of silt and sand would cause the estimated settling to be lower. The distribution of clay, silt and sand in Braaten et al. (2004) is not considered, giving a great source of error in the estimations of the settling potential. The potential for soil deformation can in this study only be viewed in a short-term perspective. As the construction continues, and foundation piles are installed, the risk of further pore pressure reduction is high. Based on the estimated settling potential the impact level is considered negligible according to the classification of Piciullo et al. (2021).

The hydrogeological setting in Oslo is relevant for several other areas in Norway were marine mud is deposited on a fractured aquifer bedrock, possibly with glacial moraine deposits situated between (Hansen et al., 2014). The 3D model sensitivity study and the pore pressure analysis illustrates how the hydrogeological setting at Gaustad is sensitive to changes in the piezometric surface and pore pressure. The magnitude of the pore pressure migration and sediment compaction depends on the individual site stratigraphy. The potential risks found at Gaustad is relevant for greater parts of Oslo (Hauser, 2020), and the presence of more permeable layers interbedded within marine clay is central in how susceptible the area is related to pore pressure migration and sediment compaction. One major challenge when considering the risks of settling is the surrounding infrastructure and buildings. Over time the pore pressure changes can migrate resulting in ground settling that can cause damage to pipes, foundations, roads and public transport lines. In such cases it is often a challenge to separate the naturally occurring sediment compaction and anthropogenic influence as the cause for settling in the sediment.

Part I

Conclusion

The 3D groundwater model is more sensitive to changes in the hydraulic pressure of the fractured aquifer when the interbedded silt and sand layers in the marine clay are represented. The presence of more permeable layers in the marine mud increases the potential for pore pressure migration.

The lateral extent of the silt and sand layers gives potential for horizontal pore pressure migration to areas outside the construction pit. Compared to experience data the risks associated with the present pore pressure reduction in the marine clay are negligible.

The changing individual layer thicknesses within the marine mud affects the potential for differential compaction. The area close to Bukken Bruses vei has a high potential for sediment compaction over a longer time period, due the possibility of pore pressure migration in the thin silt and sand layers.

6.5 Further work

- Representation of the local anisotropy in the fractured bedrock would give potential for a more realistic groundwater flow model.
- A modelling simulation to predict the actual effect the groundwater lowering has on the pore pressure evolution.
- It would be interesting to collect more reliable groundwater samples to determine the actual effect of the stabilizing lime-cement mixture on the groundwater quality, and if the effects are traceable further downstream.
- For determining the potential sediment compaction and related risk the consolidation history of the marine mud should be determined based on the sediments pressure history.

Bibliography

Alley, W. M., Healy, R. W., LaBaugh, J. W. & Reilly, T. E. (2002). Flow and storage in groundwater systems. *science*, *296*(5575), 1985–1990.

Baardvik, G., Engen, A., Kalsnes, B., Karlsrud, K., Lande, E. J., Langford, J., Simonsen, A., Tvedt, G. & Veslegard, G. (2016). *Begrensing av skader som følge av grunnarbeider: Begrens skade sluttrapport*. Norges Geotekniske Institutt.

Bjørvik, F. V. (2021). *Urban impact on water quality and the local water budget - gaustad, oslo*, University of Oslo.

Bonte, M., Stuyfzand, P. J., Hulsmann, A. & Van Beelen, P. (2011). Underground thermal energy storage: Environmental risks and policy developments in the netherlands and european union. *Ecology and Society*, *16*(1).

Booth, D. B. (1991). Urbanization and the natural drainage system–impacts, solutions, and prognoses.

Braaten, A., Baardvik, G., Vik, A. & Brendbekken, G. (2004). *Observerte effekter på poretrykk på grunn av omfattende fundamenterings-arbeider i dyp utgraving i leire.* (q624.131.3 JBV Geo). Jernbaneverket.

Darcy, H. (1856). *Les fontaines publiques de la ville de dijon: Exposition et application...* Victor Dalmont.

Dingman, S. L. (2002). *Physical hydrology* (2nd Edition). Prentice-Hall Inc., New Jersey.

DIONEX. (2006). *Ics-2000 ion chromatography system operator's manual* (3rd ed.).

Dupont, S. & Mestayer, P. G. (2006). Parameterization of the urban energy budget with the submesoscale soil model. *Journal of Applied Meteorology and Climatology*, *45*(12), 1744–1765.

Eriksson, J. I., Kielland, S. G. & et al. (2019). *Undergrunnen, prosjekt for økt kunnskap om og forvaltning av undergrunnen*. Oslo Kommune. https://www.oslo.kommune.no/getfile.php/13359465-1609853457/Tjenester

Fellenius, B. & Eslami, A. (2000). Soil profile interpreted from cptu data. *Proceedings of Year 2000 Geotechnics Conference, Southeast Asian Geotechnical Society, Asian Institute of Technology, Bangkok, Thailand*, *1*, 163–171.

Fetter, C. W. (2018). *Applied hydrogeology*. Waveland Press.

FHI. (2021). *Kjemiske og fysiske stoffer i drikkevann*. https://www.fhi.no/nettpub/stoffer-i-drikkevann/kjemiske-og-fysiske-stoffer-i-drikkevann/kjemiske-og-fysiske-stoffer-i-drikkevann/

Freeze, R. A. & Cherry, J. A. (1979). *Groundwater*. Prentice-Hall Inc., New Jersey.

GMS. (2020a). *Modflow – generating data from solids* (v. 10.5).

GMS. (2020b). *Stratigraphy modeling — horizons and solids* (v. 10.5).

Hansen, L., Høgaas, F., Sveian, H., Olsen, L. & Rindstad, B. I. (2014). Quaternary geology as a basis for landslide susceptibility assessment in fine-grained, marine deposits, onshore norway. *Landslides in sensitive clays* (pp. 369–381). Springer.

Harbaugh, A. W. (2005). *Modflow-2005, the u.s. geological survey modular ground-water model—the ground-water flow process* (6-A16). U.S. Geological Survey.

Hauser, C. (2020). *Vurdering av setninger i oslo s og bjørvikaområdet*. https://www.ngi.no/eng/Projects/Vurdering-av-setninger-i-Oslo-S-og-Bjoervikaomraadet

Hillis, R. R. (2001). Coupled changes in pore pressure and stress in oil fields and sedimentary basins. *Petroleum Geoscience*, *7*(4), 419–425.

Hiscock, K. M. & Bense, V. F. (2014). *Hydrogeology, principles and practice*. Wiley-Blackwell, New Jersey.

Hognestad, Å. S. & Tuttle, K. J. (2020). *Referansenivå for pore- og grunnvannstrykk* (113511tb23).

Janbu, N. (1970). *Grunnlag i geoteknikk*.

Jernbanekompeatnse. (2016). Setninger. https://www.jernbanekompetanse.no/wiki/Underbygning/Setninger#Setninger_som_problem_for_jernbaneanlegg

Karlsrud, K., Langford, J., Lande, E. J., Baardvik, G. & NGI. (2015). *Vurdering av skader og deformasjoner knyttet til utførelse av stagforankring og borede peler i byggegroper* (Begrens Skade DP 1+2.4). Norges Geotekniske Institutt.

Langford, J. (2020). *Remedy 2 – risk reduction of groundwork damage*. https://www.ngi.no/eng/Projects/BegrensSkade-II-REMEDY-Risk-Reduction-of-Groundwork-Damage/#About-the-project

Langford, J., Baardvik, G. & Karlsrud, K. (2016). Pore pressure reduction and settlements induced by deep supported excavations in soft clay. *Proceedings of the 17th Nordic Geotechnical Meeting*.

Langford, J. & Sandene, T. (2015). *Effekter av rammede peler i leire – litteraturstudium og erfaringsrapport* (Begrens Skade DP 3.3). Norges Geotekniske Institutt.

LovData. (2017). *Forskrift om vannforsyning og drikkevann (drikkevannsforskriften)*. https://lovdata.no/dokument/SF/forskrift/2016-12-22-1868#KAPITTEL_1

Lutro, O., Graversen, O., Larsen, B., Naterstad, J., Bockelie, J. & Bockelie, T. (2017). *Bedrock map* (Asker 1814-1). https://www.ngu.no/publikasjon/berggrunnskart-bedrock-map-asker-1814-1-m-150-000

Mangerud, J., Gyllencreutz, R., Lohne, Ø. & Svendsen, J. I. (2011). Glacial history of norway. *Developments in quaternary sciences* (pp. 279–298). Elsevier.

Mann, D. M. & Mackenzie, A. S. (1990). Prediction of pore fluid pressures in sedimentary basins. *Marine and Petroleum Geology*, *7*(1), 55–65.

Mehus, J., Lahus, O., Jacobsen, S. & Myhre, Ø. (2000). *Bruk av resirkulert tilslag i bygg og anlegg – status 2000* (287 – 2000). Norges byggforskningsinstitutt.

Morris, D. A. & Johnson, A. I. (1967). *Summary of hydrologic and physical properties of rock and soil materials, as analyzed by the hydrologic laboratory of the us geological survey, 1948-60* (tech. rep.). US Government Printing Office.

Nair, I. S., Parimala Renganayaki, S. & Elango, L. (2013). Identification of seawater intrusion by cl/br ratio and mitigation through managed aquifer recharge in aquifers north of chennai, india. *J. Groundw. Res*, *2*(155162), 19.

Neumann, E.-R., Olsen, K., Baldridge, W. & Sundvoll, B. (1992). The oslo rift: A review. *Tectonophysics*, *208*(1-3), 1–18.

NGF. (2017). *Veiledning for måling av grunnvannstand og poretrykk* (Nr. 6, rev. nr. 2). Norwegian Geotechnical Society.

NGI. (1971). *Gaustadbekkdalen, nedre del. supplerende grunnundersøkelser* (No. 69085). Norwegian Geotechnical Institute.

NGI. (2020). *Groundwater and hydrogeology*. https://www.ngi.no/eng/Services/Technical-expertise/Groundwater-and-hydrogeology

NGU. (2020). *Oslogruppen*. http://aps.ngu.no/pls/utf8/geoenhet_SokiDb.Vis_enhet?p_id=145138&p_spraak=N

Oftedahl, C. (1959). Volcanic sequence and magma formation in the oslo region. *Geologische Rundschau*, *48*(1), 18–26.

Piciullo, L., Ritter, S., Lysdahl, A. O. K., Langford, J. & Nadim, F. (2021). Assessment of building damage due to excavation-induced displacements: The gibv method. *Tunnelling and Underground Space Technology*, *108*, 103673.

Ramberg, I. B. & Smithson, S. B. (1971). Gravity interpretation of the southern oslo graben and adjacent precambrian rocks, norway. *Tectonophysics*, *11*(6), 419–431.

Ricard, L. P., MacBeth, C., HajNasser, Y. & Schutjens, P. (2012). An evaluation of pore pressure diffusion into a shale overburden and sideburden induced by production-related changes in reservoir fluid pressure. *Journal of Geophysics and Engineering*, *9*(3), 345–358.

Ritter, Solomon, K., Sibley, P., Hall, K., Keen, P., Mattu, G. & Linton, B. (2002). Sources, pathways, and relative risks of contaminants in surface water and groundwater: A perspective prepared for the walkerton inquiry. *Journal of Toxicology and Environmental Health Part A*, *65*(1), 1–142.

Schirmer, M., Leschik, S. & Musolff, A. (2013). Current research in urban hydrogeology–a review. *Advances in Water Resources*, *51*, 280–291.

Seibert, J. (1996). Hbv light. *User's manual, Uppsala University, Institute of Earth Science, Department of Hydrology, Uppsala*.

Solheim, A. & Groenlie, G. (1983). Quaternary sediments and bedrock geology in the outer oslofjord and northernmost skagerrak. *Norsk geologisk tidsskrift*, *63*, 55–72.

StatensVegvesen. (2014). *Grunnforsterkning, fyllinger og skråninger* (2nd ed., Håndbok 274). Vegdirektoratet.

Statsbygg & VAV. (2019). *Grunnforhold. poretrykksmålinger.* (NO-RIG-20-14).

Stratford, W. & Thybo, H. (2011). Crustal structure and composition of the oslo graben, norway. *Earth and Planetary Science Letters*, *304*(3-4), 431–442.

Terzaghi, K. v. (1936). The shearing resistance of saturated soils and the angle between the planes of shear. *First international conference on soil Mechanics, 1936*, *1*, 54–59.

Trask, P. D. (1931). Compaction of sediments. *AAPG Bulletin*, *15*(3), 271–276.

Tuttle, K. J. (2020). *Hydrogeologisk prosjektering. hydrogeologisk modellering av ulike scenarioer av tettetiltak for byggegropen mot grunnvannslekkasjer* (NO-RIG-20-39).

VAV & Statsbygg. (2016). *Ny kulvert og åpen bekk, kapasiteter og vannstander* (Rev. 02, NO-RIVA-70-04).

VAV & Statsbygg. (2019). *Geoteknisk datarapport. grunnforhold* (Rev. 04, RA-RIG-20-001).

VAV & Statsbygg. (2020). *Geoteknisk prosjektering. oppsummering borehullslogging* (Rev. 00, NO-RIG-20-41).

Vázquez-Suñé, E., Sánchez-Vila, X. & Carrera, J. (2005). Introductory review of specific factors influencing urban groundwater, an emerging branch of hydrogeology, with reference to barcelona, spain. *Hydrogeology Journal*, *13*(3), 522–533.

Appendix A

Appendix

A.1 Previous Data

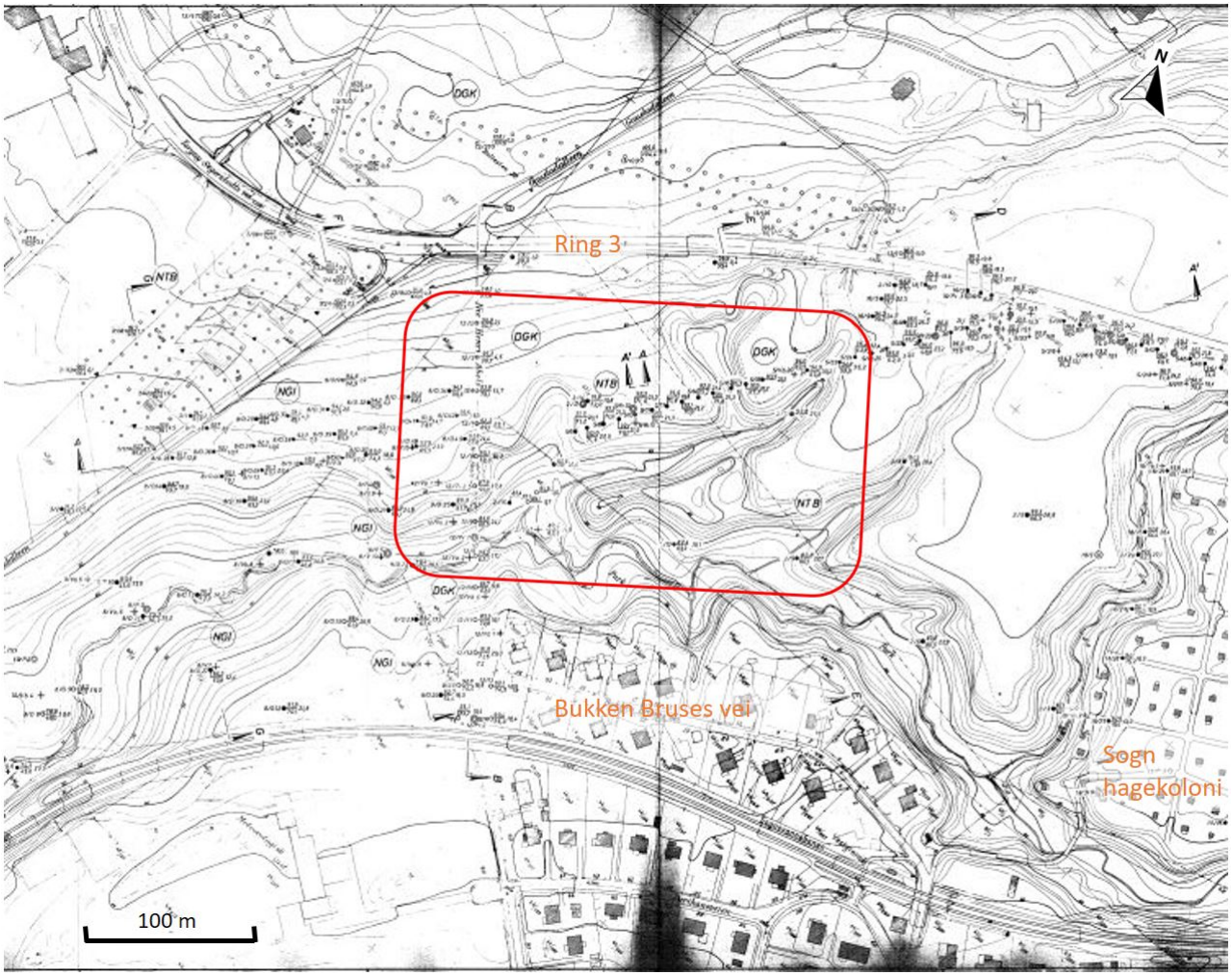

Figure A.1: Topographic map of Gaustadbekkdalen from 1969 (VAV and Statsbygg, 2019). The construction site is located inside the area of the red box. Three old river valleys connect with Gaustad river towards the south-west.

A.1.1 Total sounding and CTPU

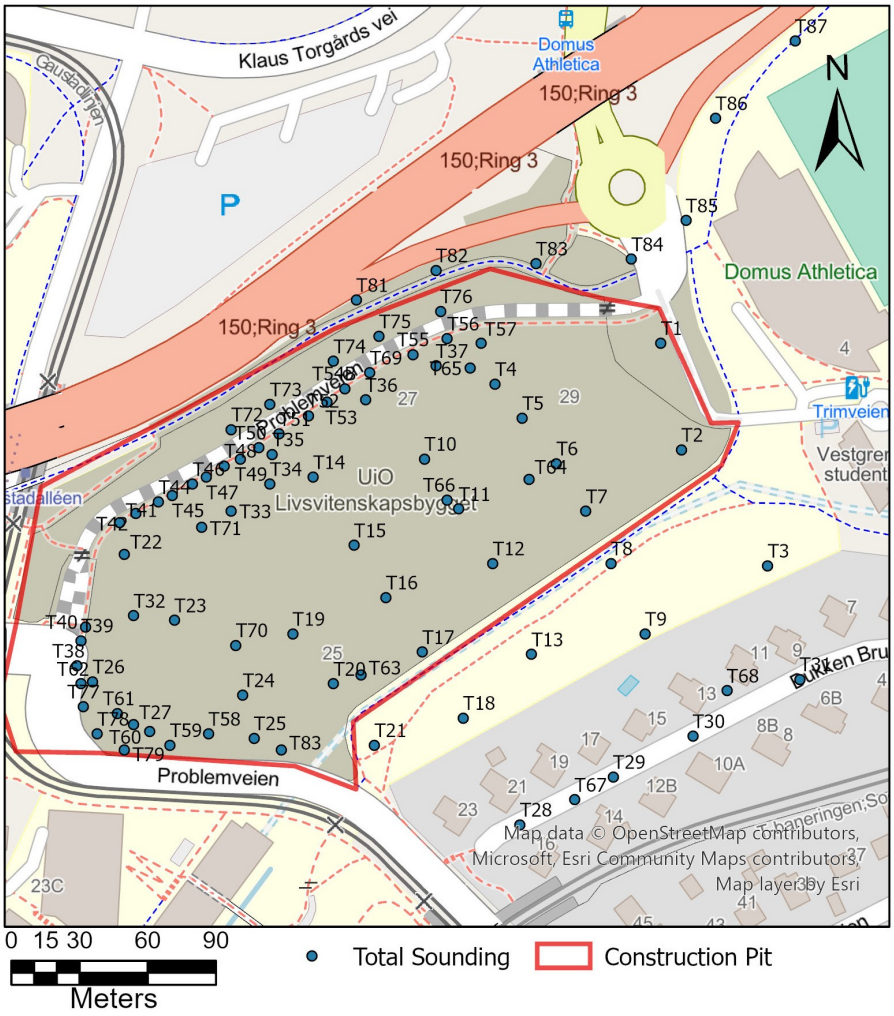

Figure A.2: Measuring points for total sounding from VAV and Statsbygg (2019).

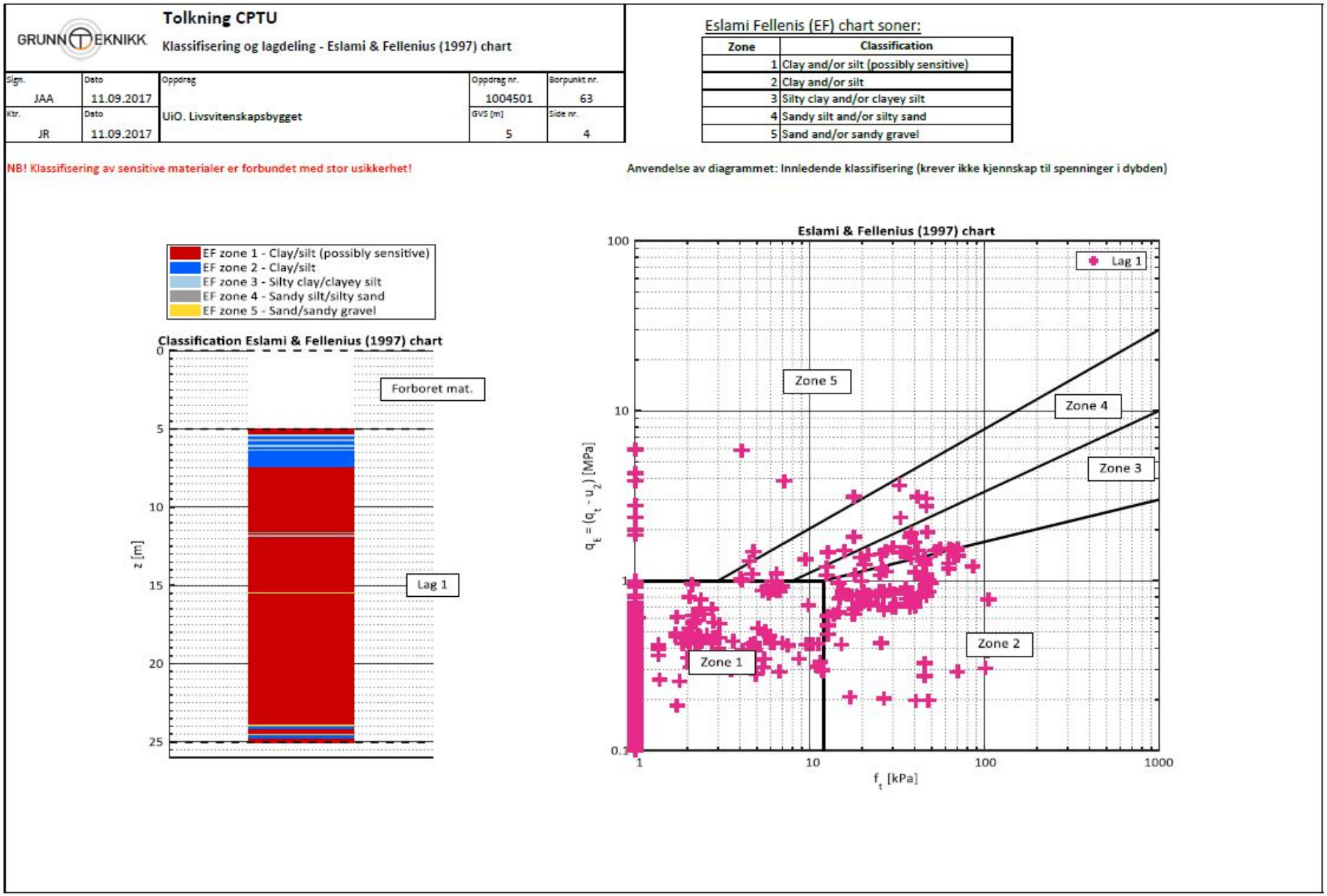

Figure A.3: CPTU interpretation from T63. In the MODFLOW model the stratigraphy is determined based on the classification zones, where zone 1 2 is clay, zone 3 4 is slit and zone 5 is sand. Modified from VAV and Statsbygg (2019).

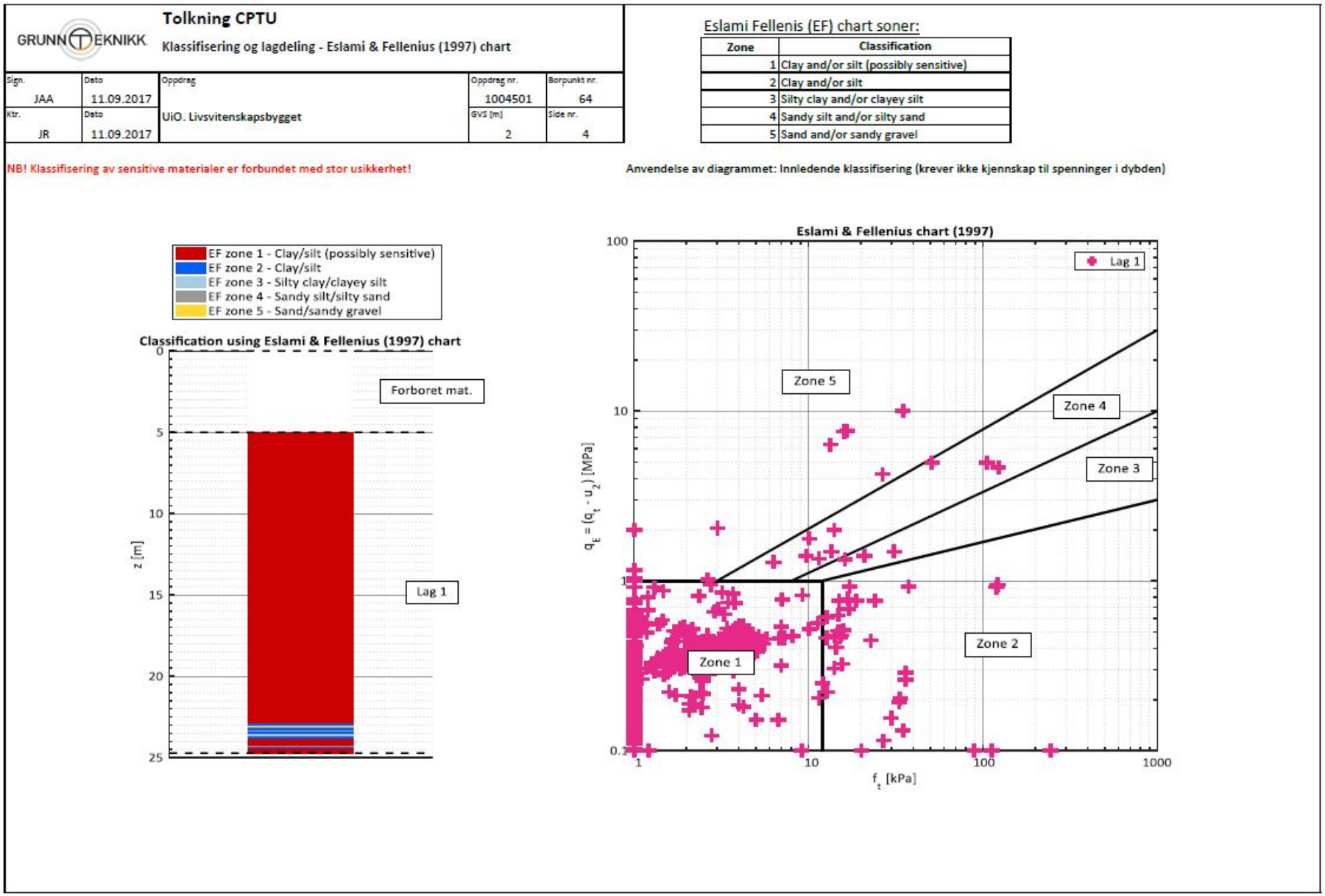

Figure A.4: CPTU interpretation from T64. In the MODFLOW model the stratigraphy is determined based on the classification zones, where zone 1 2 is clay, zone 3 4 is slit and zone 5 is sand. Modified from VAV and Statsbygg (2019).

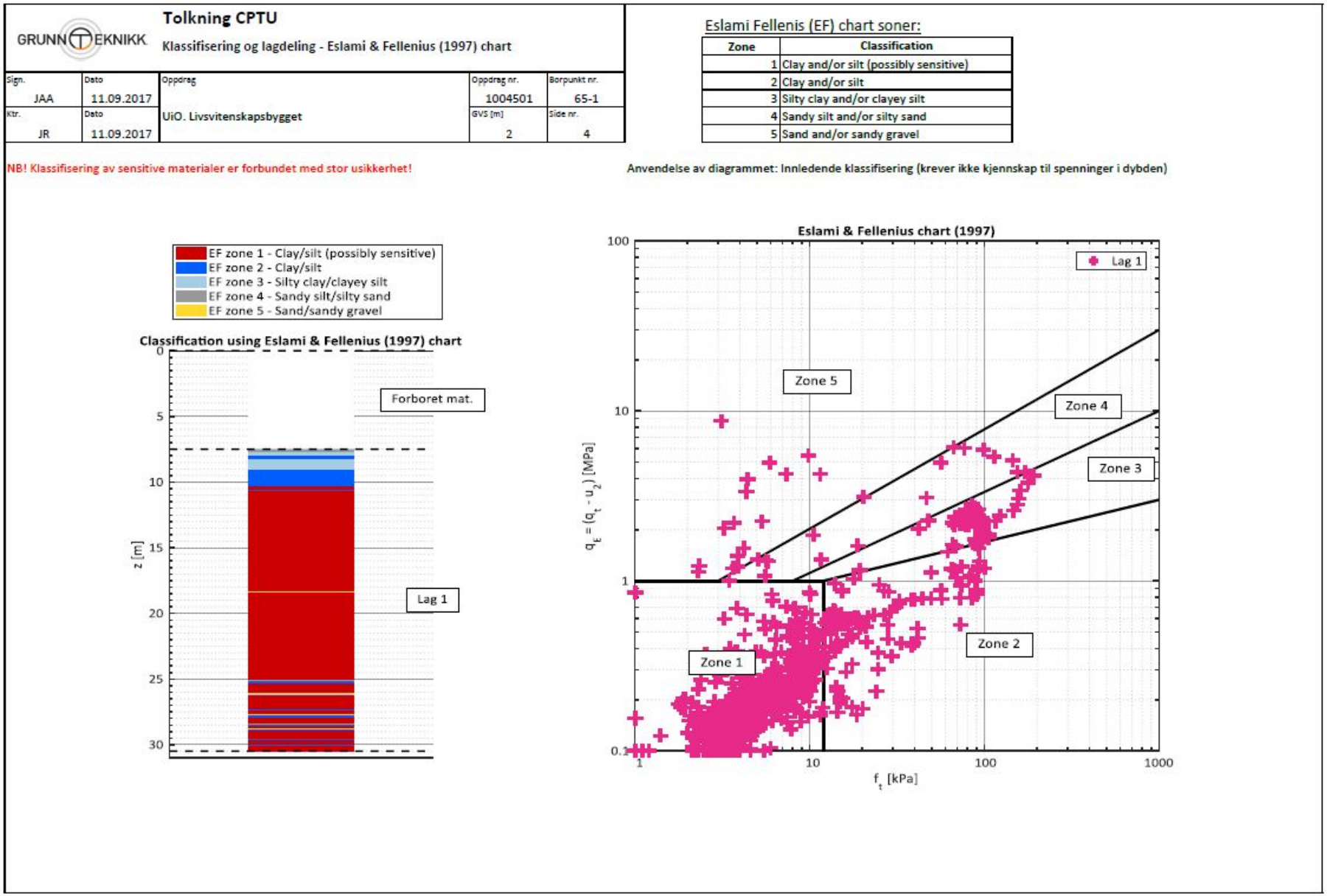

Figure A.5: CPTU interpretation from T65. In the MODFLOW model the stratigraphy is determined based on the classification zones, where zone 1 2 is clay, zone 3 4 is slit and zone 5 is sand. Modified from VAV and Statsbygg (2019).

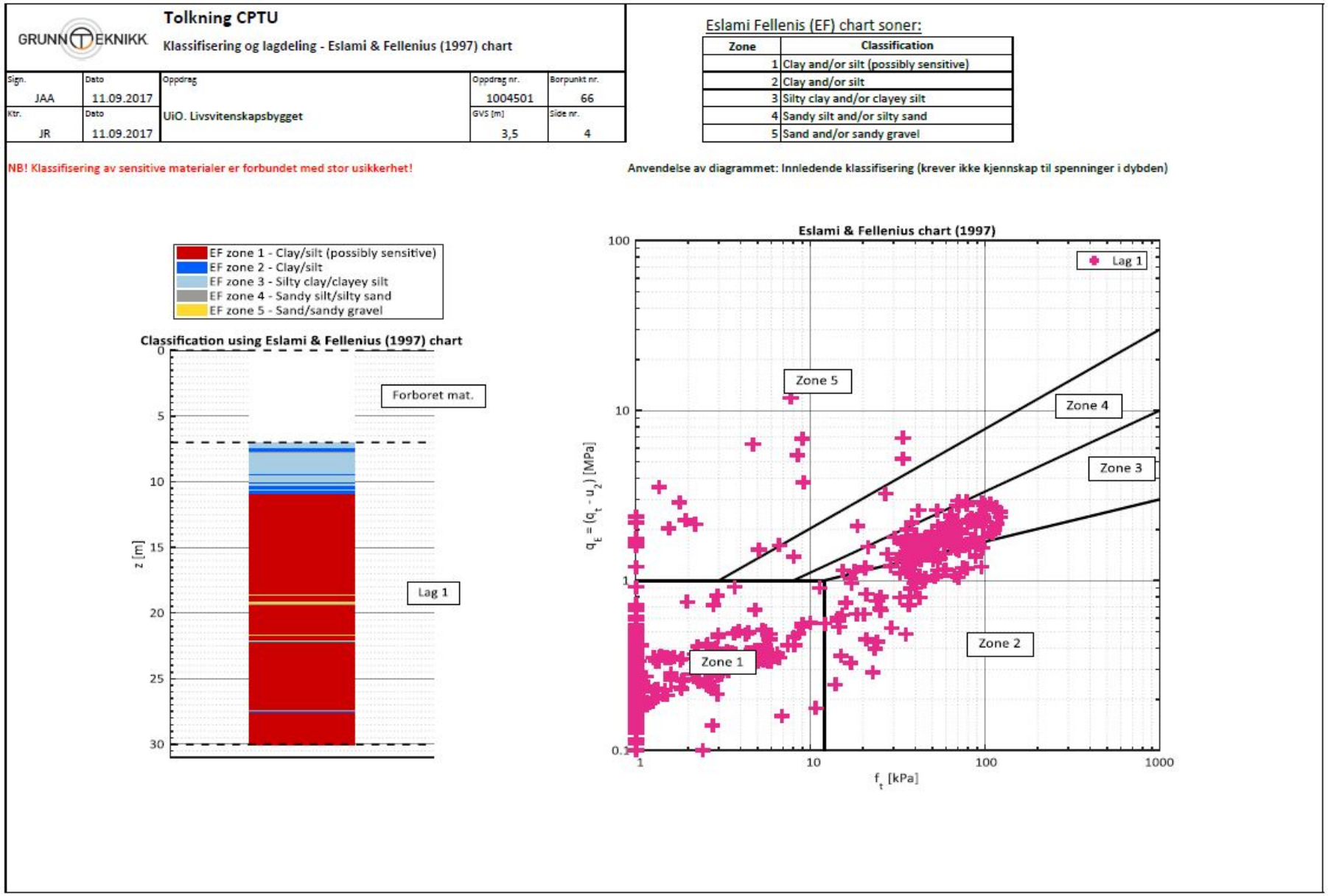

Figure A.6: CPTU interpretation from T66. In the MODFLOW model the stratigraphy is determined based on the classification zones, where zone 1 2 is clay, zone 3 4 is slit and zone 5 is sand. Modified from VAV and Statsbygg (2019).

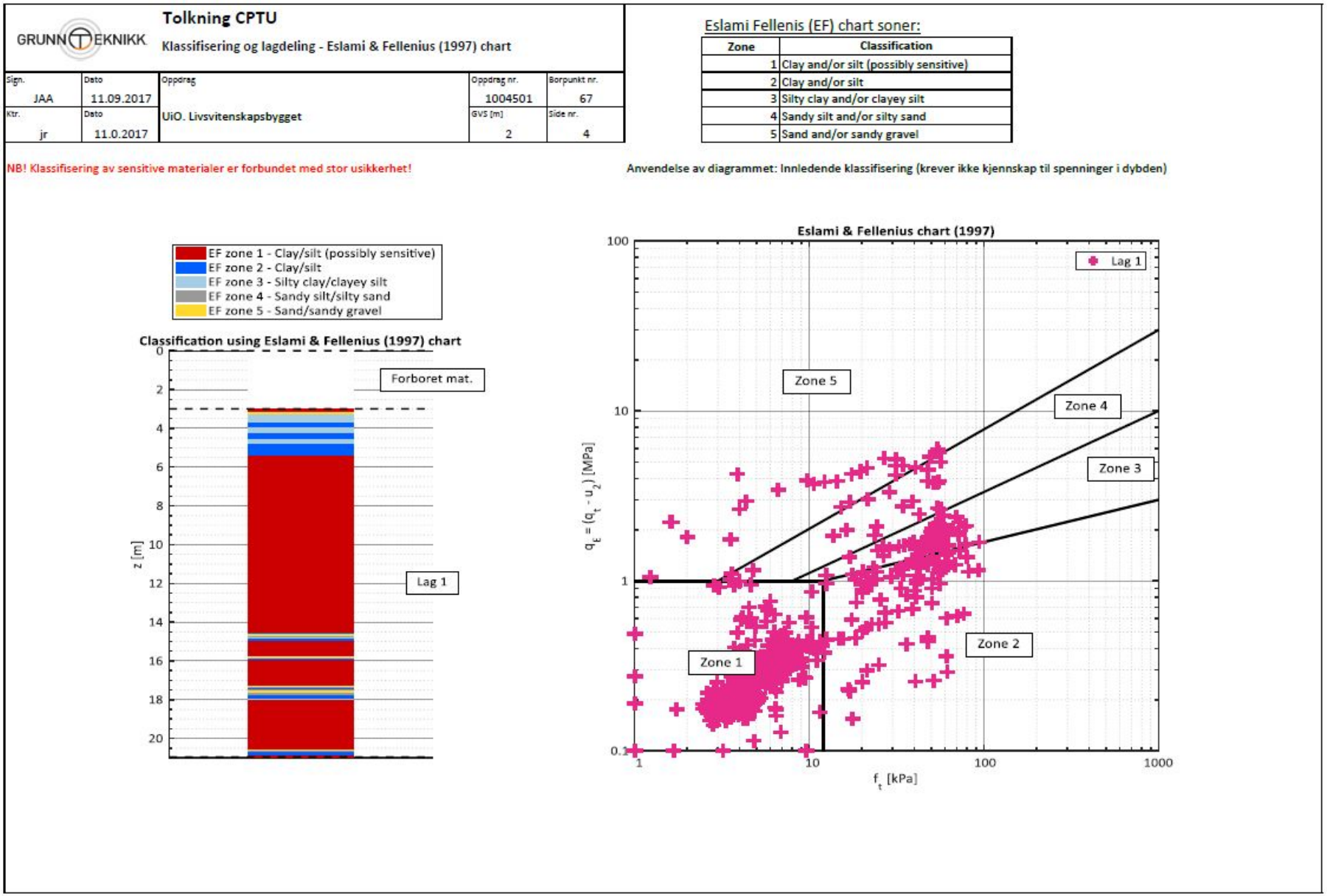

Figure A.7: CPTU interpretation from T67. In the MODFLOW model the stratigraphy is determined based on the classification zones, where zone 1 2 is clay, zone 3 4 is slit and zone 5 is sand. Modified from VAV and Statsbygg (2019).

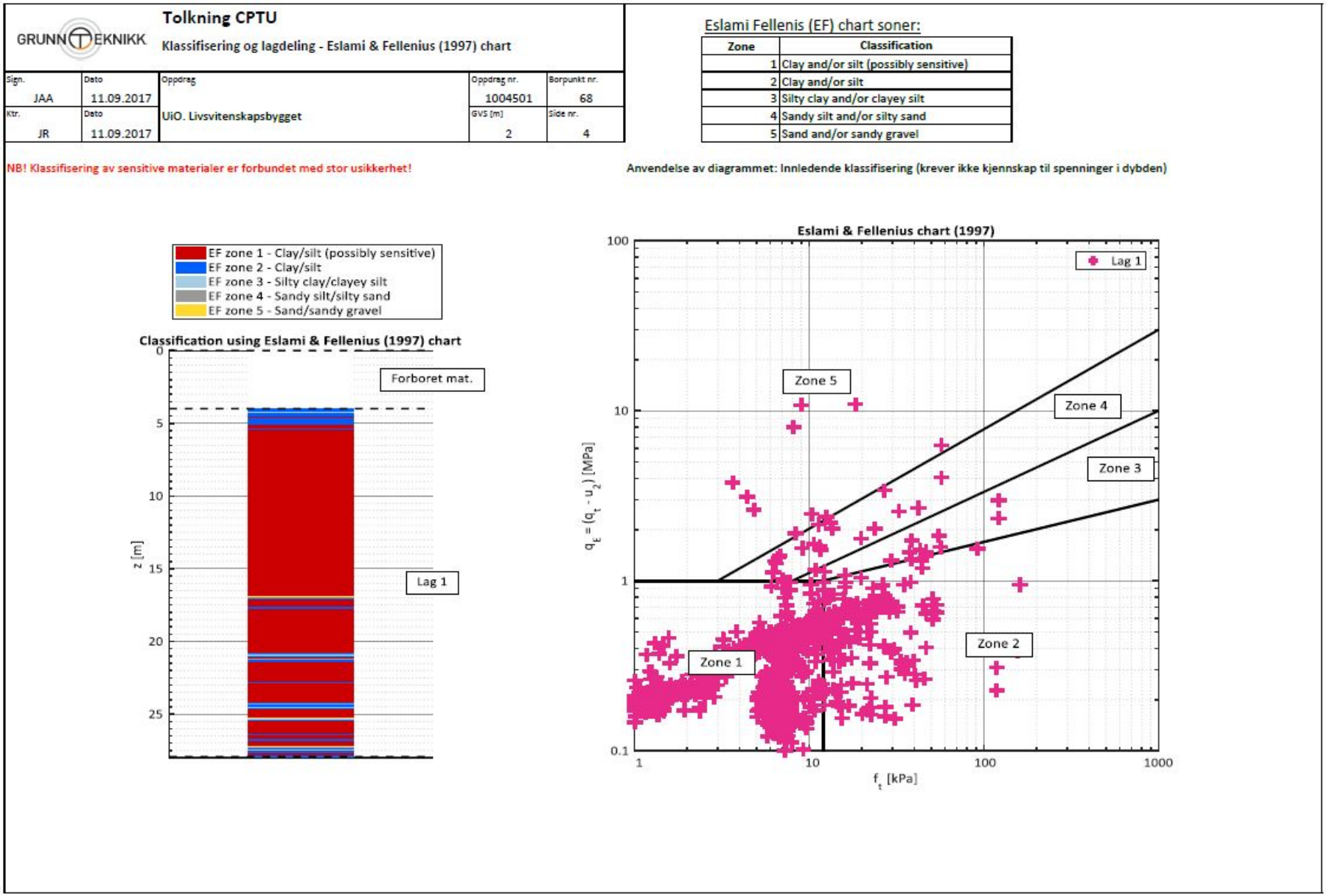

Figure A.8: CPTU interpretation from T68. In the MODFLOW model the stratigraphy is determined based on the classification zones, where zone 1 2 is clay, zone 3 4 is slit and zone 5 is sand. Modified from VAV and Statsbygg (2019).

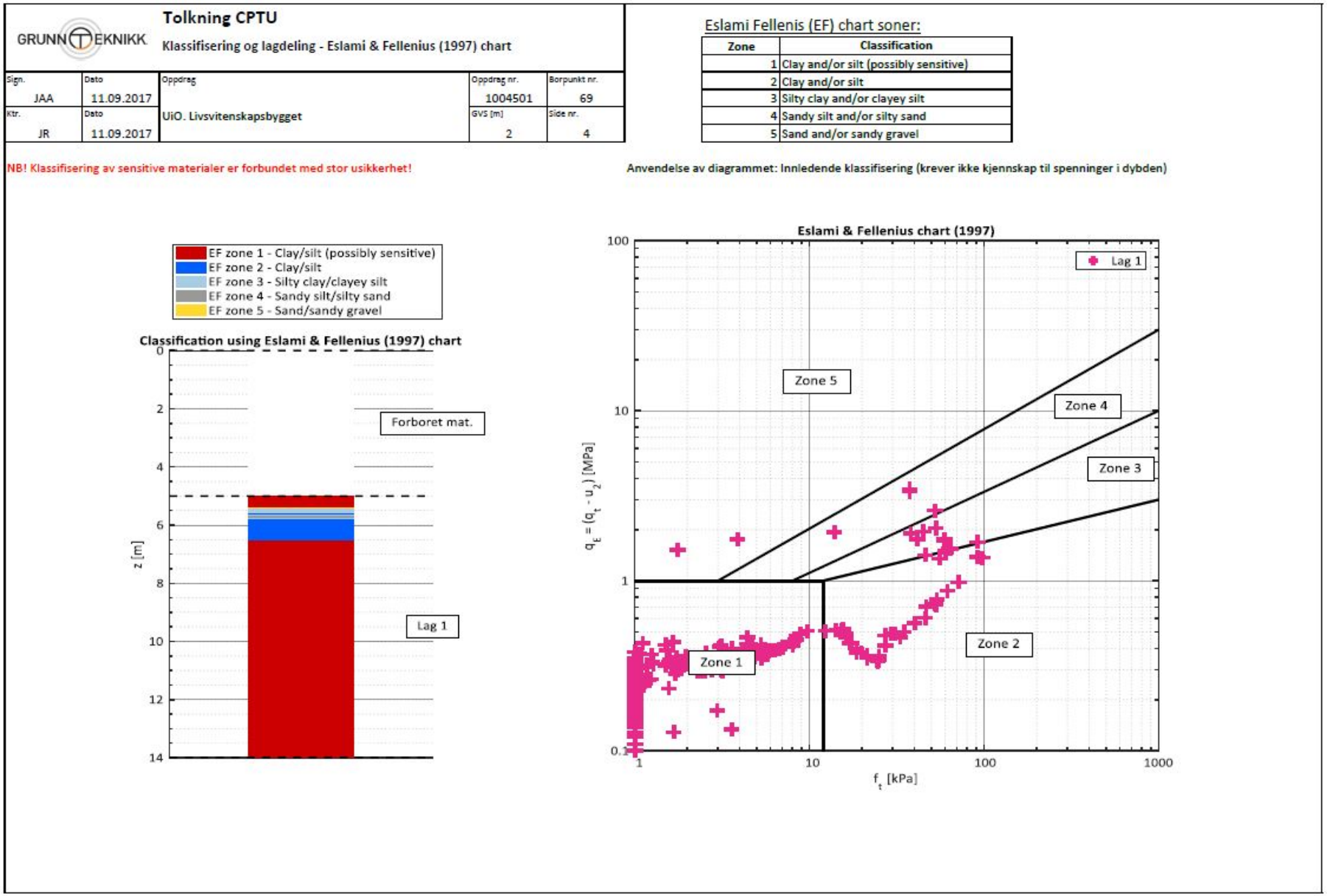

Figure A.9: CPTU interpretation from T69. In the MODFLOW model the stratigraphy is determined based on the classification zones, where zone 1 2 is clay, zone 3 4 is slit and zone 5 is sand. Modified from VAV and Statsbygg (2019).

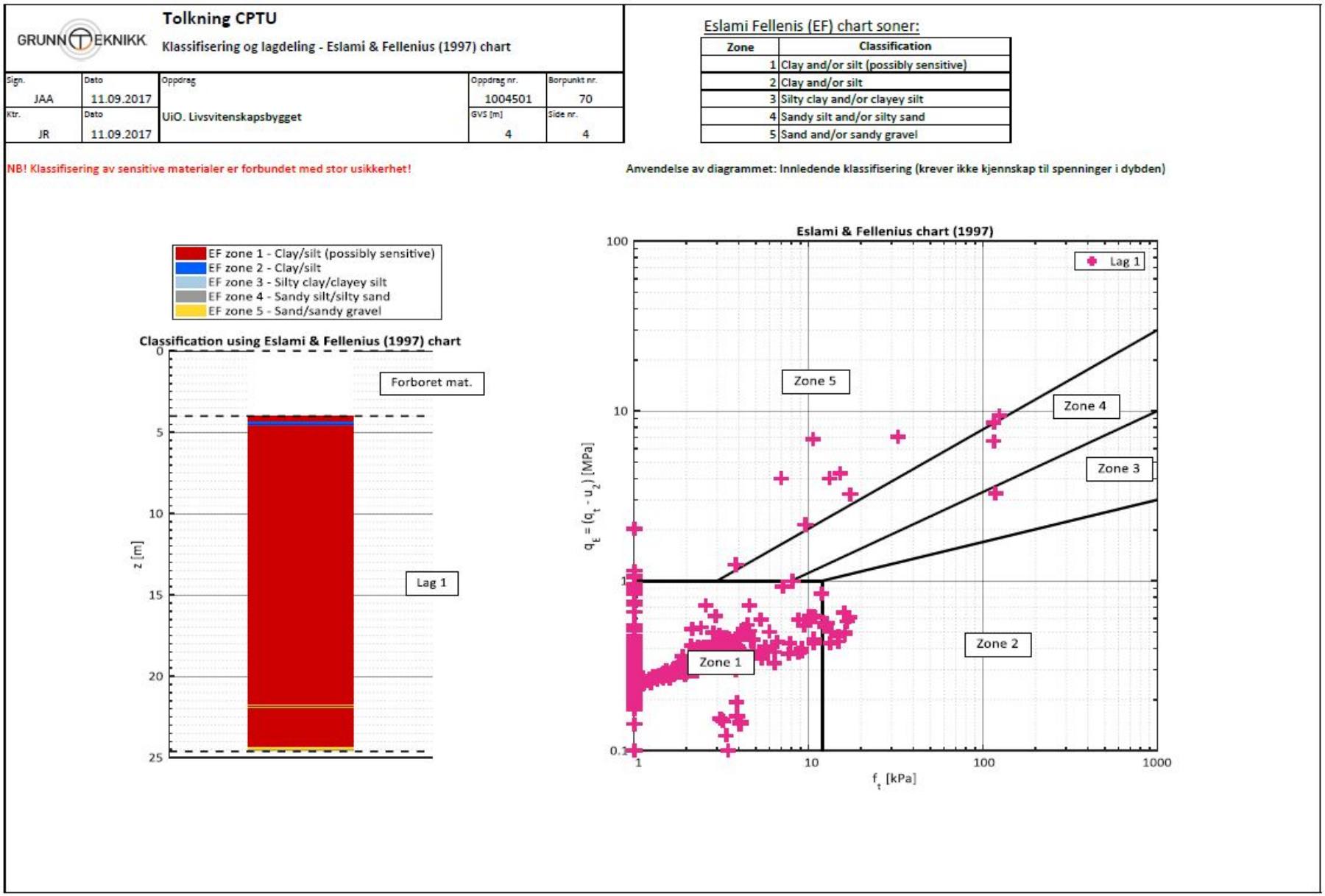

Figure A.10: CPTU interpretation from T70. In the MODFLOW model the stratigraphy is determined based on the classification zones, where zone 1 2 is clay, zone 3 4 is slit and zone 5 is sand. Modified from VAV and Statsbygg (2019).

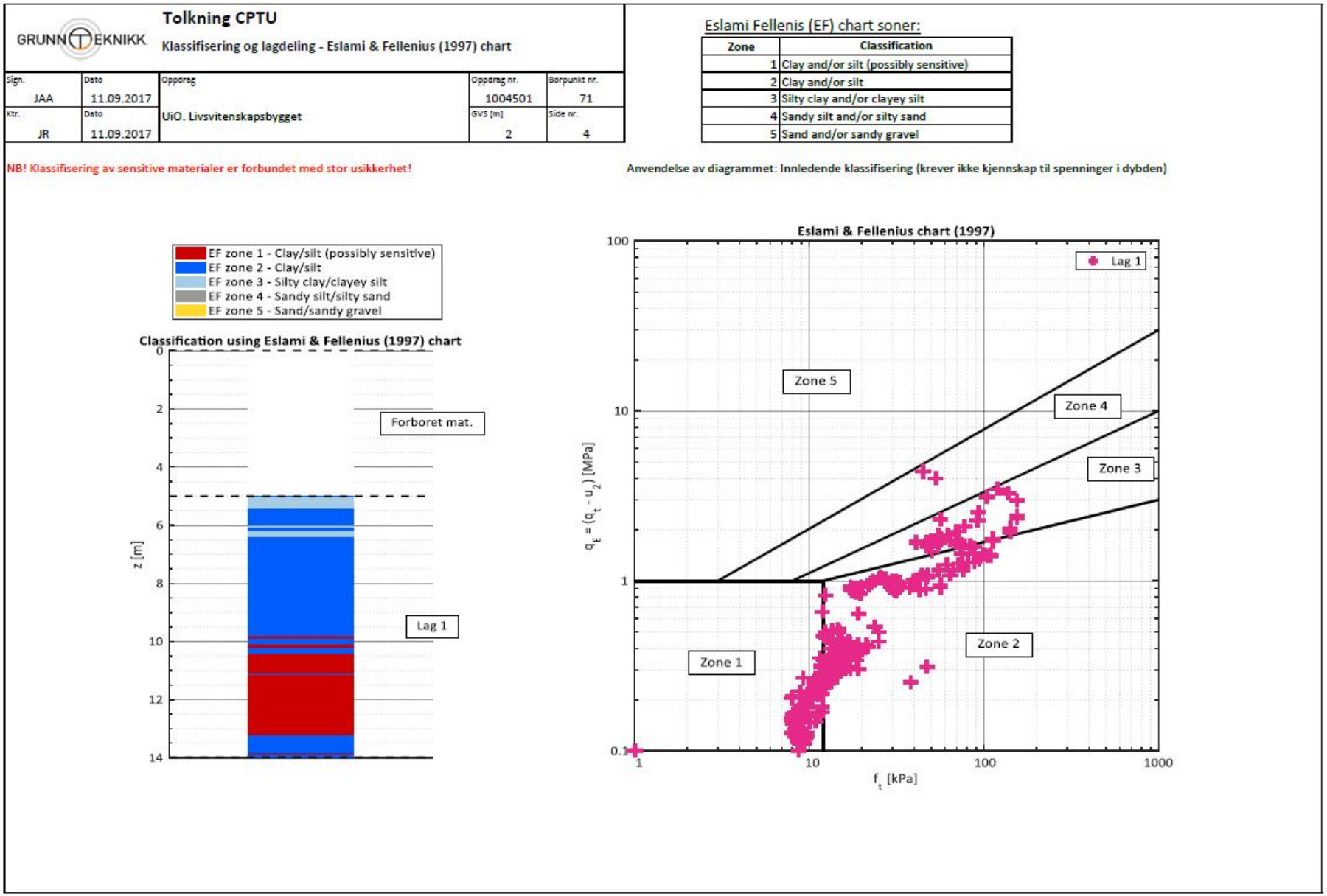

Figure A.11: CPTU interpretation from T71. In the MODFLOW model the stratigraphy is determined based on the classification zones, where zone 1 2 is clay, zone 3 4 is slit and zone 5 is sand. Modified from VAV and Statsbygg (2019).

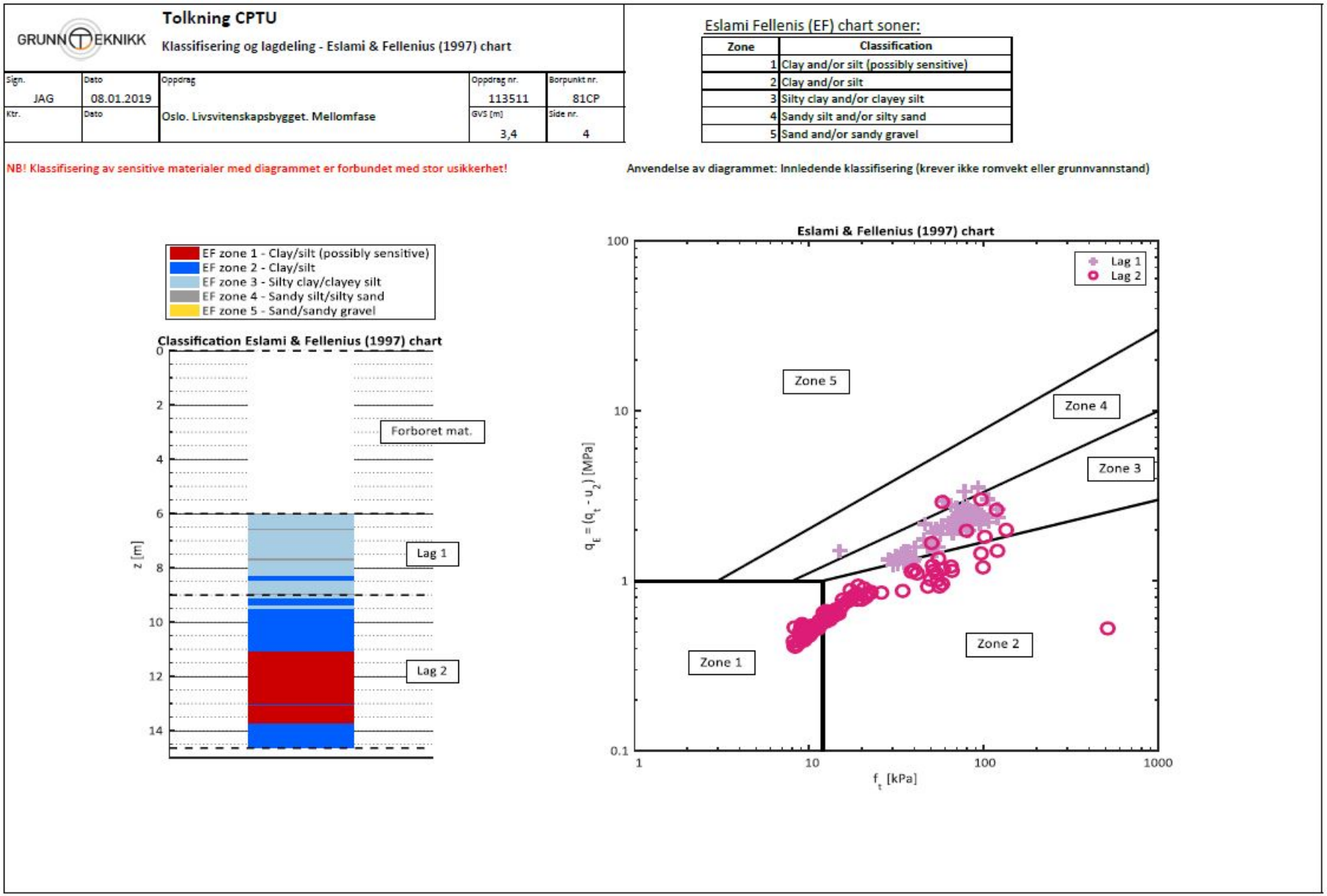

Figure A.12: CPTU interpretation from T81. In the MODFLOW model the stratigraphy is determined based on the classification zones, where zone 1 2 is clay, zone 3 4 is slit and zone 5 is sand. Modified from VAV and Statsbygg (2019).

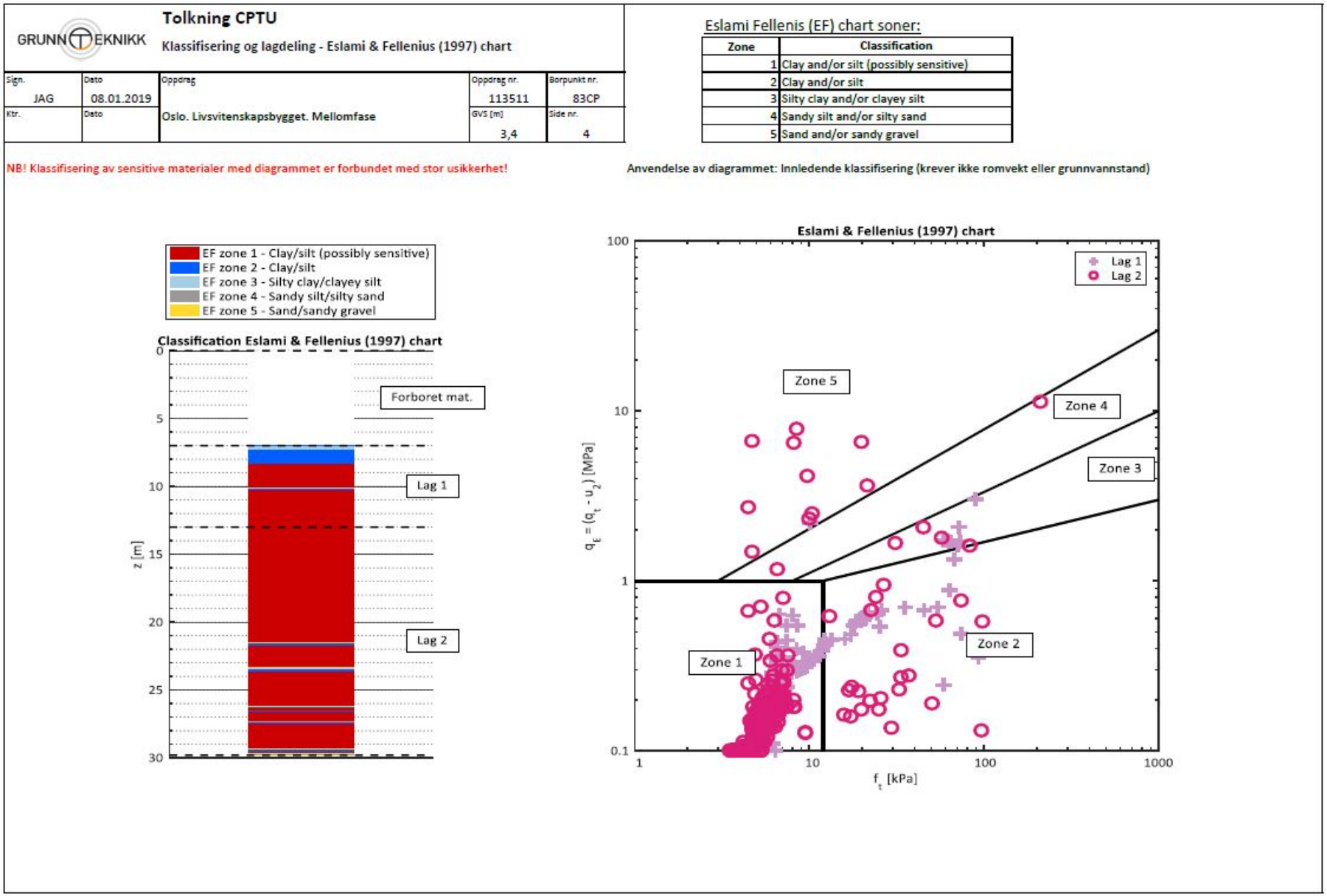

Figure A.13: CPTU interpretation from T83. In the MODFLOW model the stratigraphy is determined based on the classification zones, where zone 1 2 is clay, zone 3 4 is slit and zone 5 is sand. Modified from VAV and Statsbygg (2019).

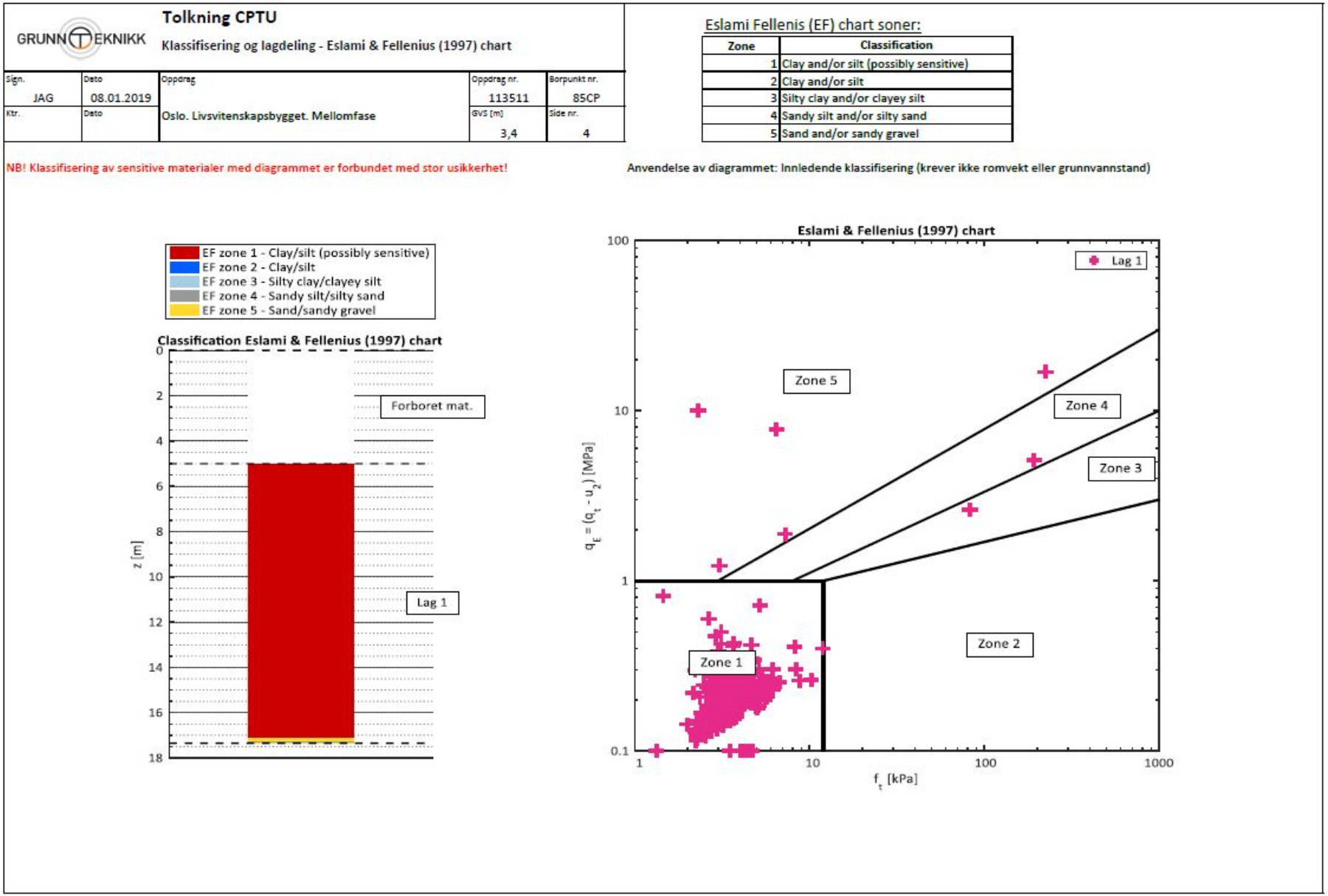

Figure A.14: CPTU interpretation from T85. In the MODFLOW model the stratigraphy is determined based on the classification zones, where zone 1 2 is clay, zone 3 4 is slit and zone 5 is sand. Modified from VAV and Statsbygg (2019).

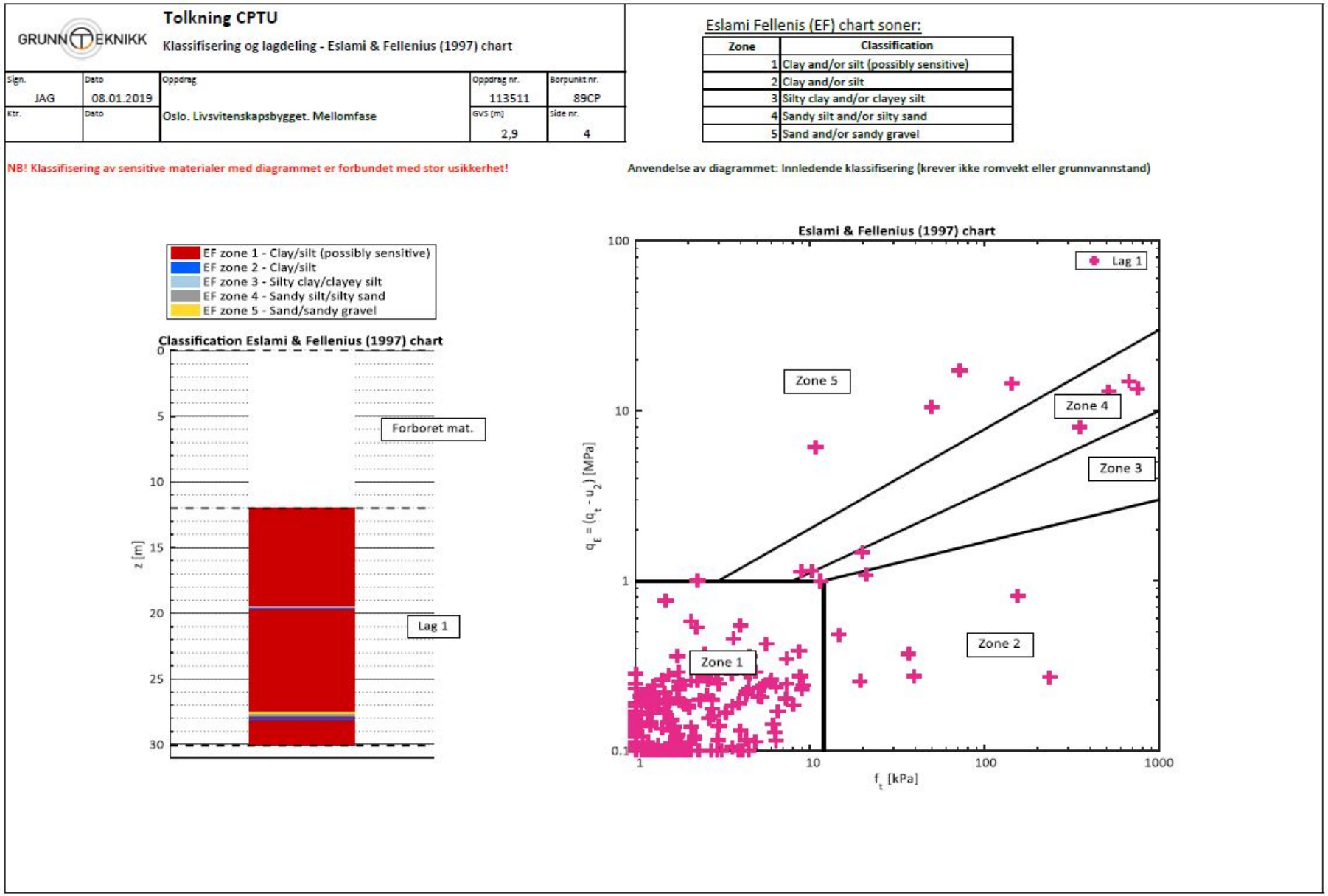

Figure A.15: CPTU interpretation from T89. In the MODFLOW model the stratigraphy is determined based on the classification zones, where zone 1 2 is clay, zone 3 4 is slit and zone 5 is sand. Modified from VAV and Statsbygg (2019).

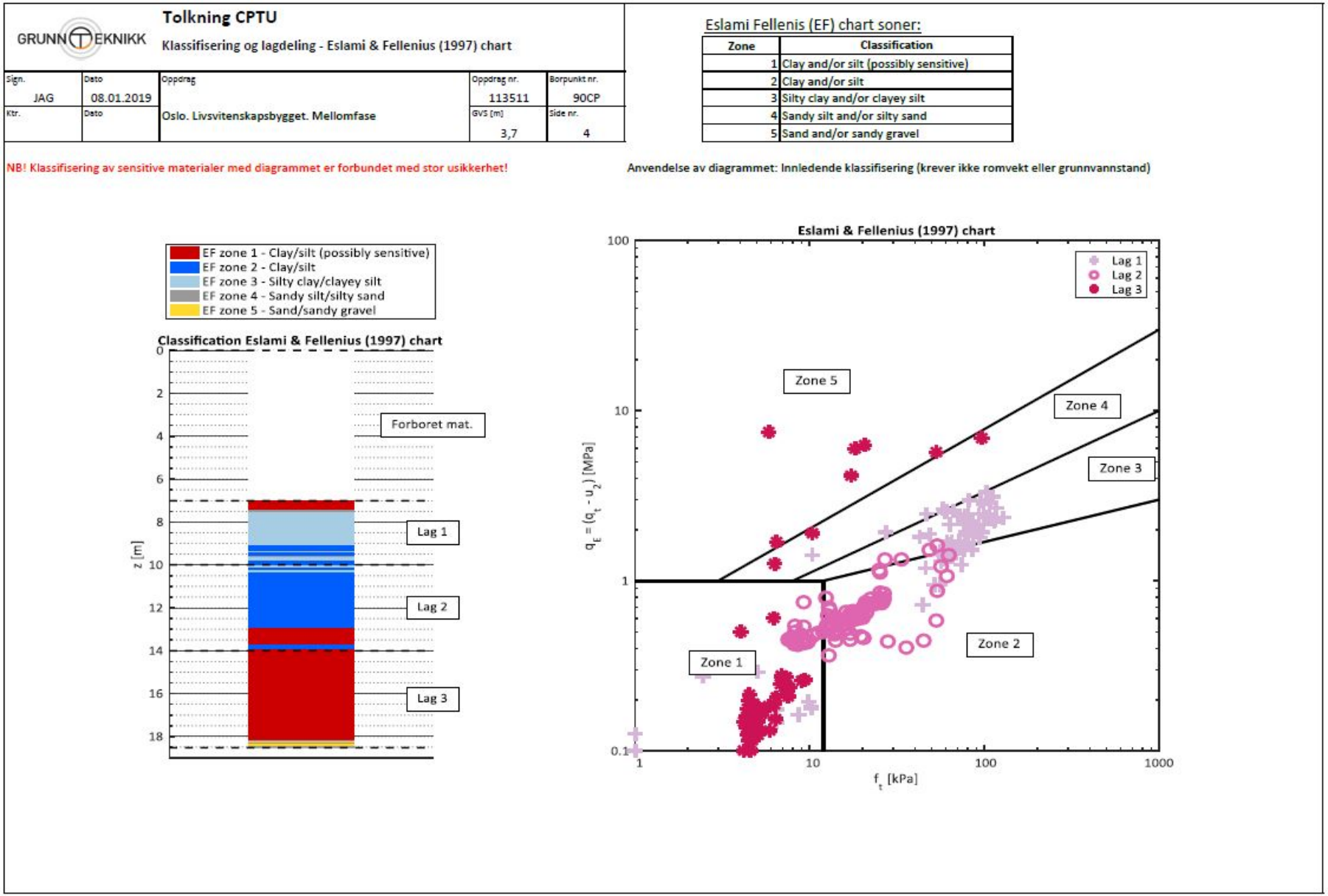

Figure A.16: CPTU interpretation from T90. In the MODFLOW model the stratigraphy is determined based on the classification zones, where zone 1 2 is clay, zone 3 4 is slit and zone 5 is sand. Modified from VAV and Statsbygg (2019).

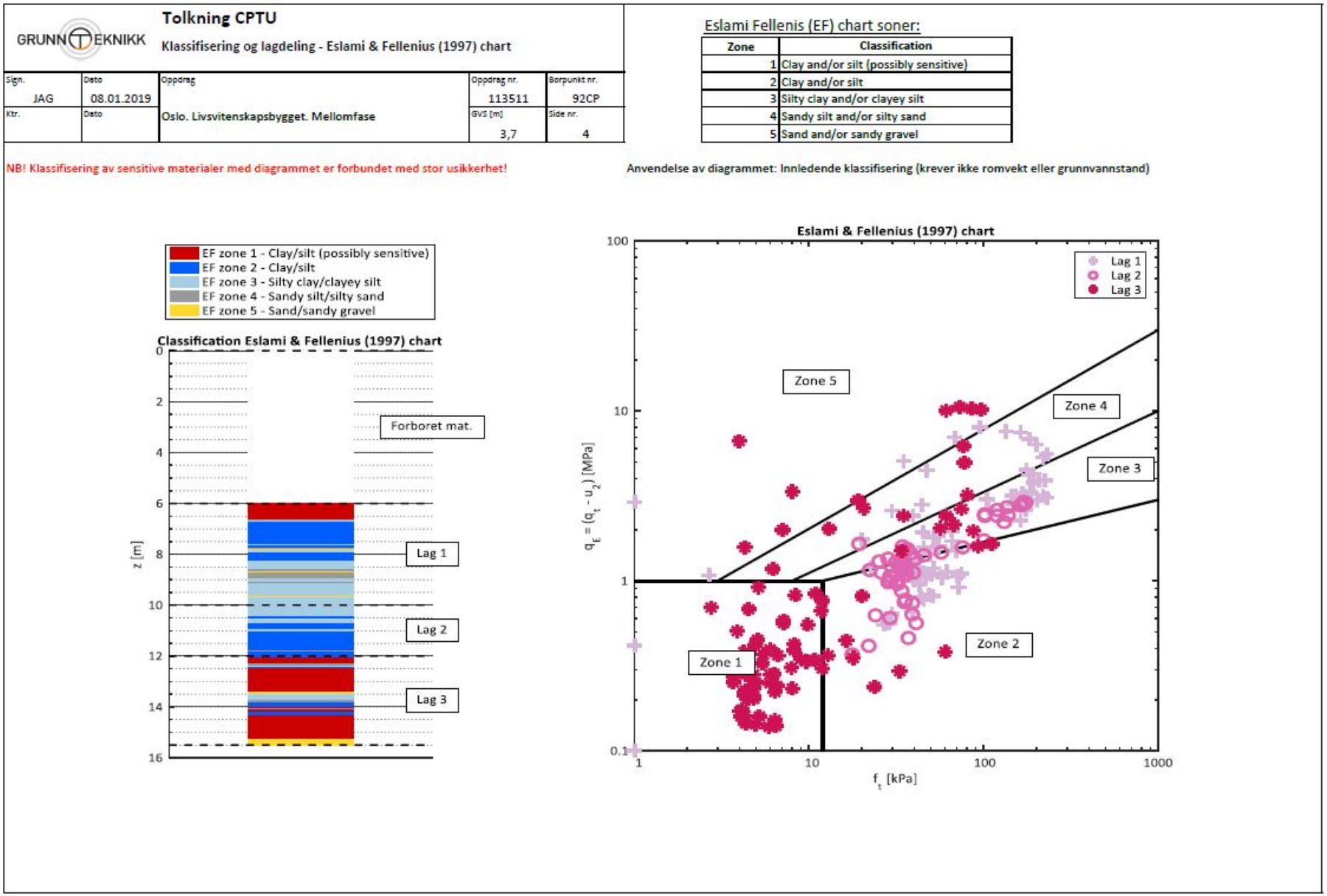

Figure A.17: CPTU interpretation from T92. In the MODFLOW model the stratigraphy is determined based on the classification zones, where zone 1 2 is clay, zone 3 4 is slit and zone 5 is sand. Modified from VAV and Statsbygg (2019).

A.1.2 Borehole logs

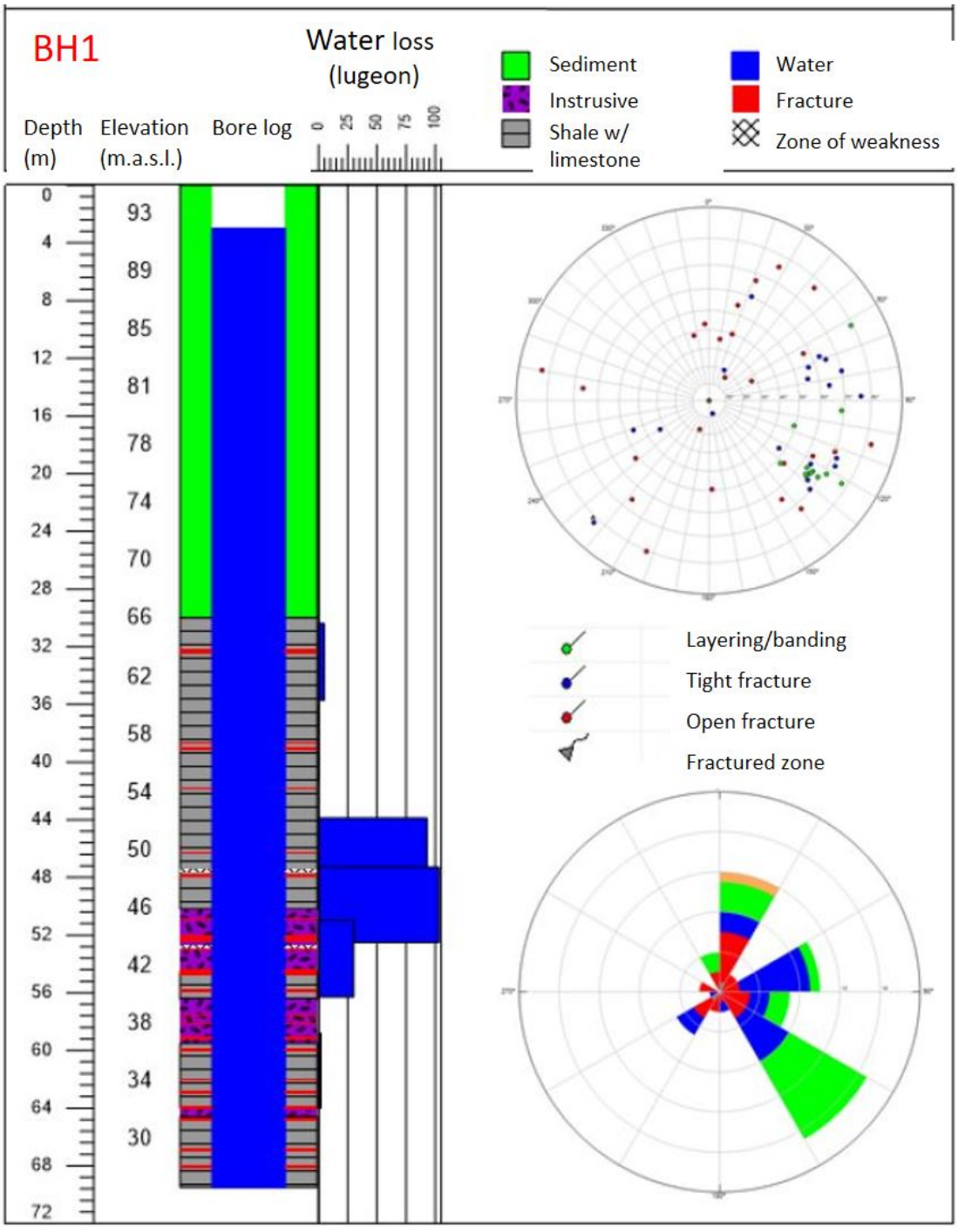

Figure A.18: Borehole interpretation modified from VAV and Statsbygg (2020) for borehole 1.

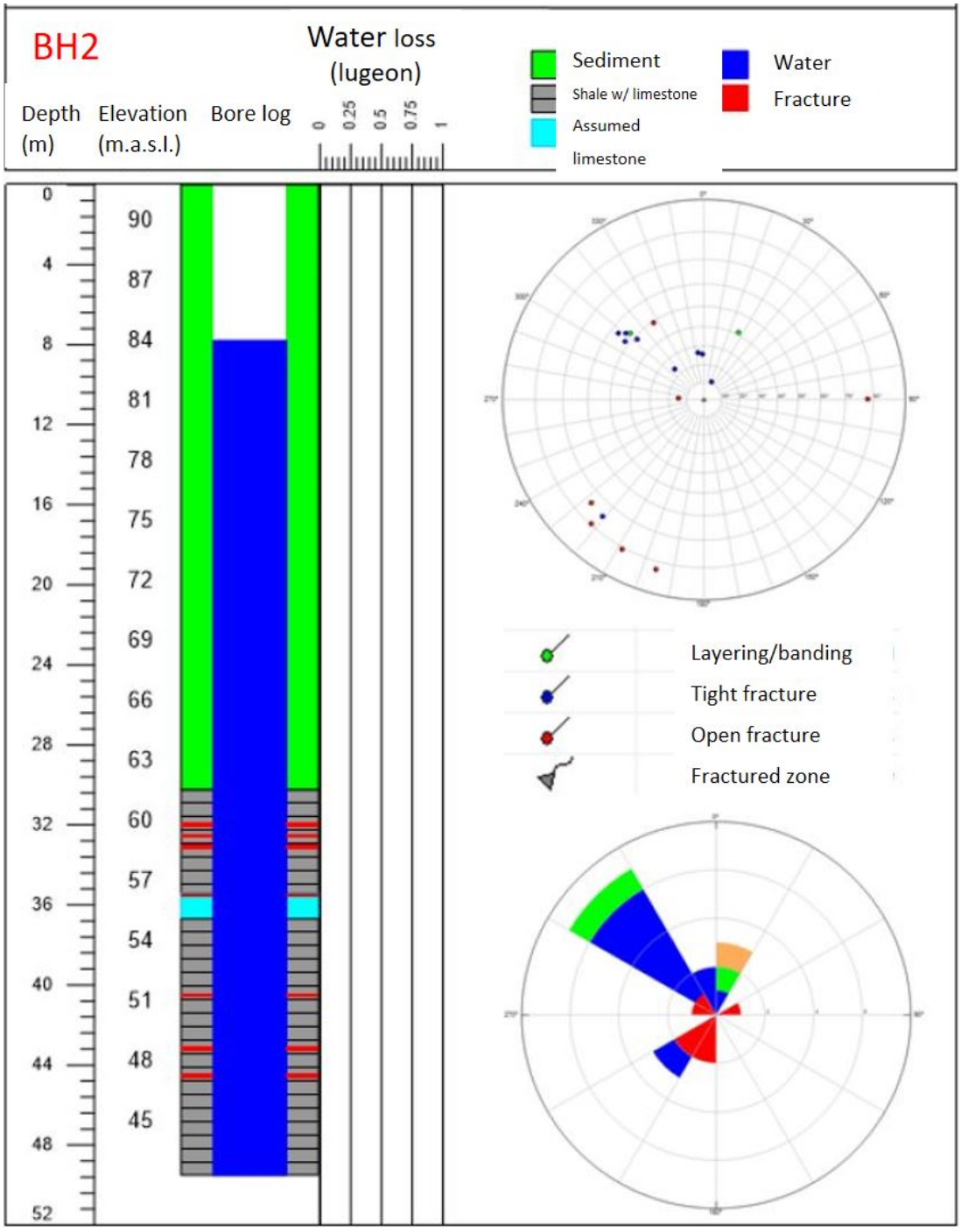

Figure A.19: Borehole interpretation modified from VAV and Statsbygg (2020) for borehole 2.

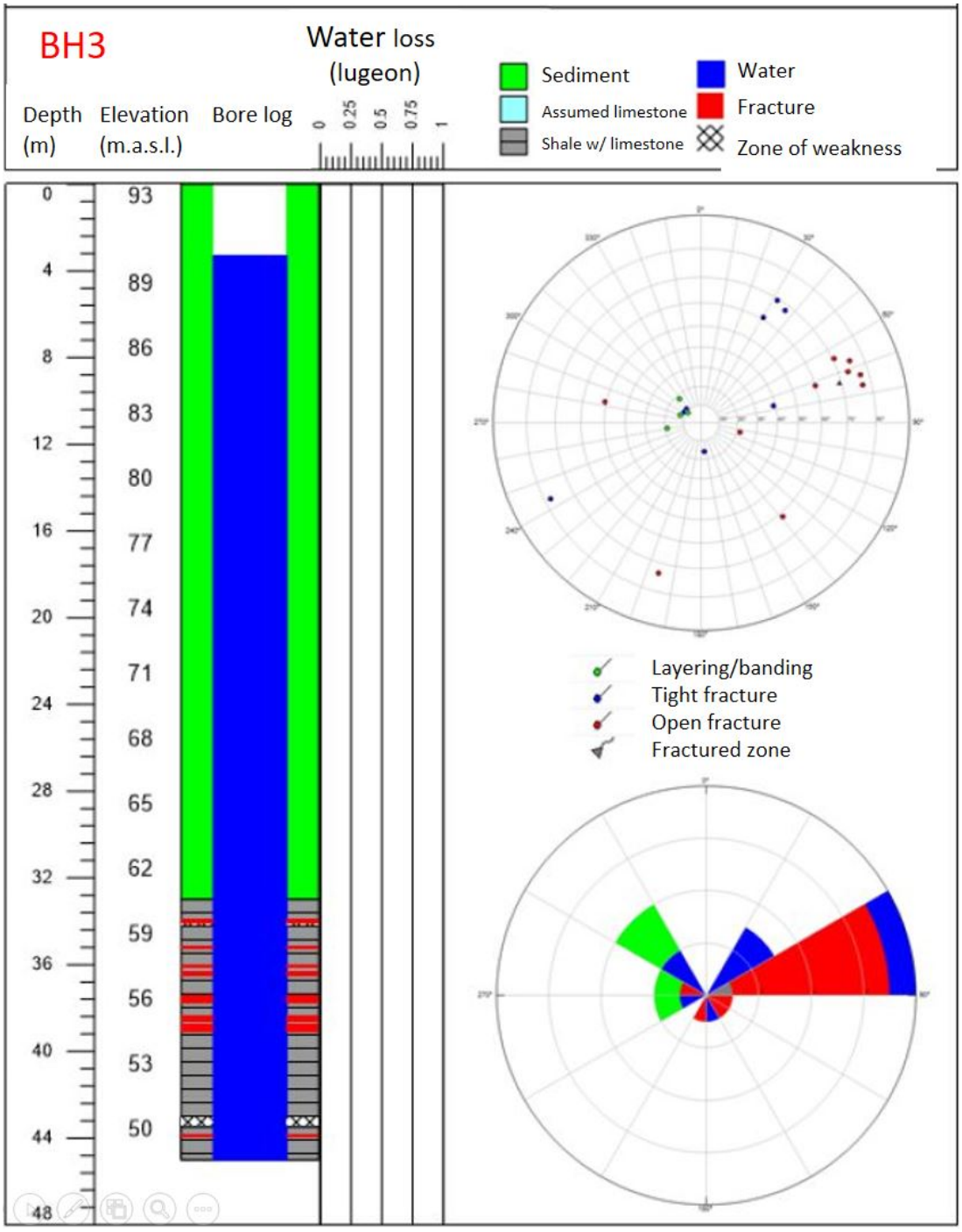

Figure A.20: Borehole interpretation modified from VAV and Statsbygg (2020) for borehole 3.

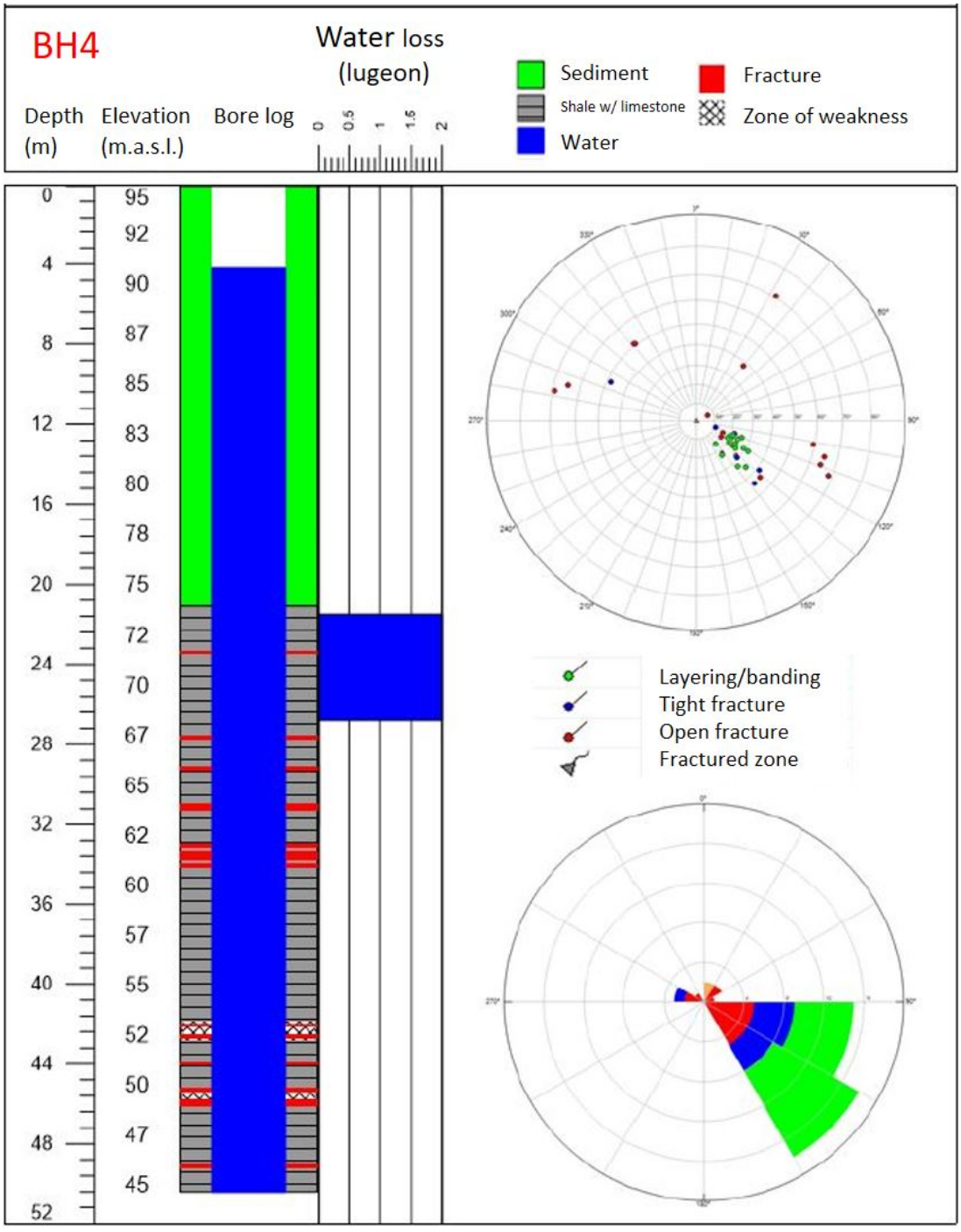

Figure A.21: Borehole interpretation modified from VAV and Statsbygg (2020) for borehole 4.

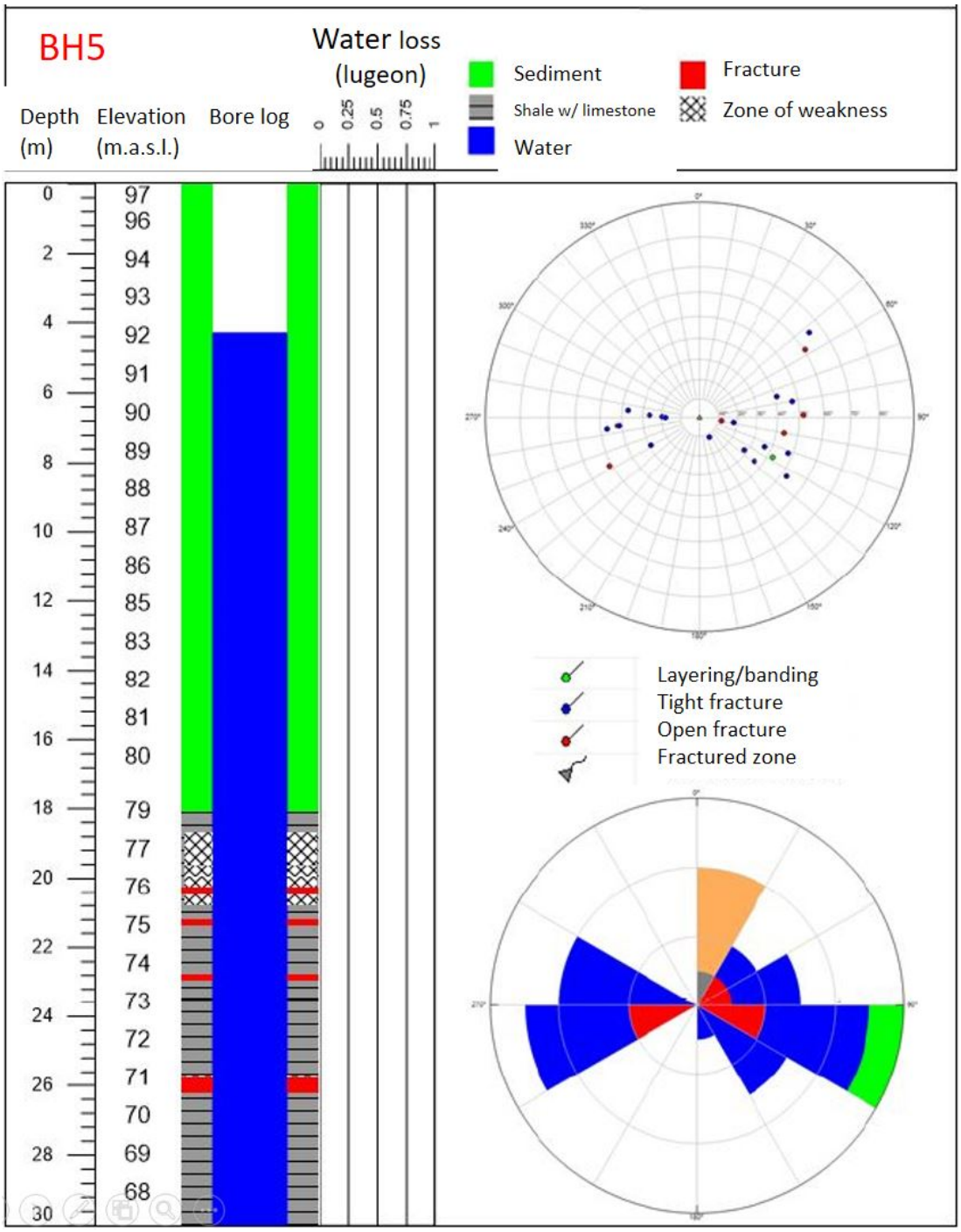

Figure A.22: Borehole interpretation modified from VAV and Statsbygg (2020) for borehole 5.

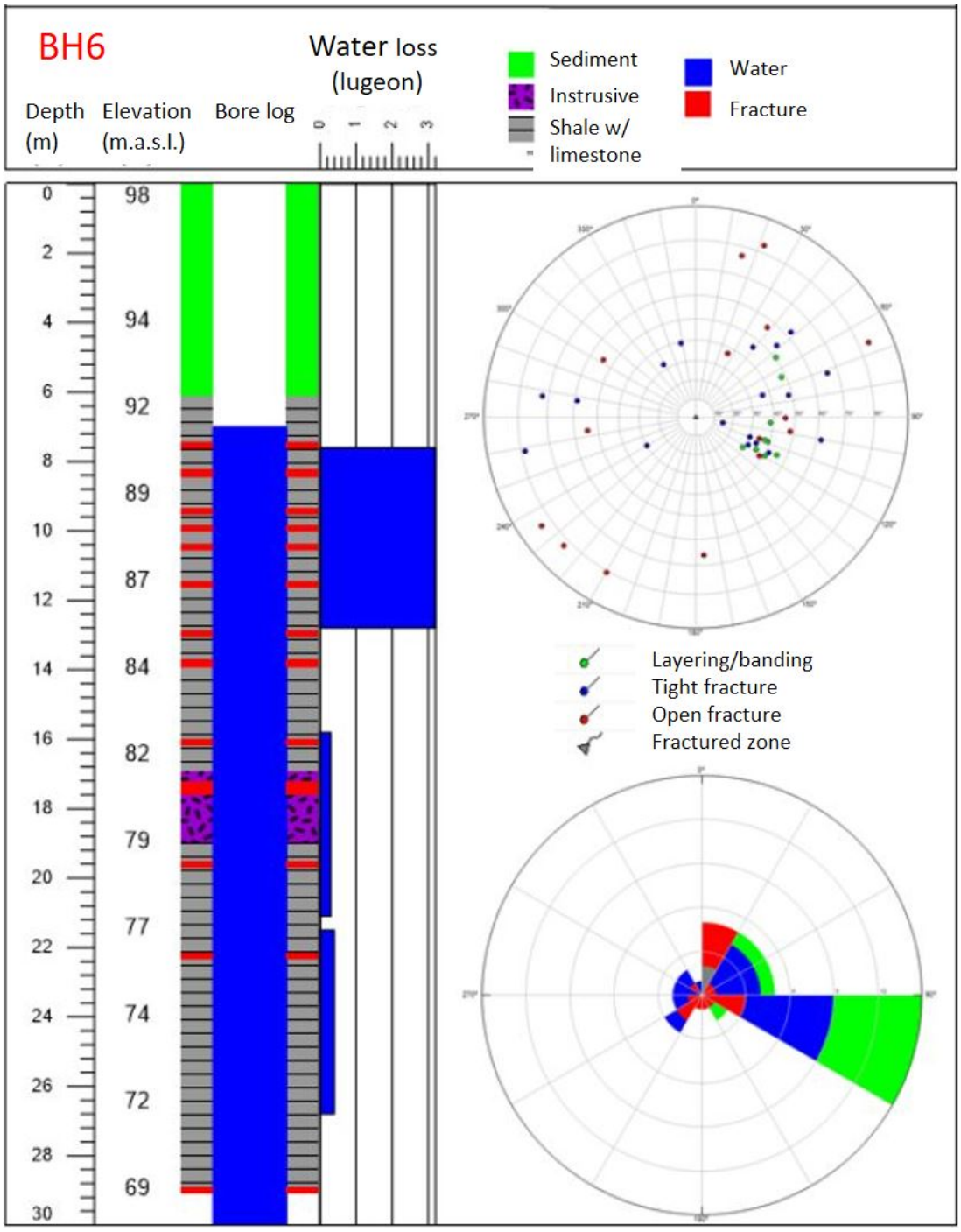

Figure A.23: Borehole interpretation modified from VAV and Statsbygg (2020) for borehole 6.

A.2 Groundwater Chemistry

For some of the samples the measured value was higher that the calibrated detection range, and the sample was diluted to ten times its volume and measured again. From table A.1 & A.2 is it apparent that the diluted samples have a measured value approximately ten times lower than the original sample. This gives reason to believe that the originally measured value can be used as an estimate for major ion concentration in the water.

Table A.1: Summary of major cations in groundwater samples. Values in red are above the calibrated detection limit and was diluted 10 times.

ID	Na [mg/L]	K [mg/L]	Mg [mg/L]	Ca [mg/L]	Li [mg/L]	NH4 [mg/L]
BH1	51.4881	5.4522	24.1908	75.7482	-	-
BH1 x 10	5.1483	0.5469	2.4143	7.5908	-	-
BH2	148.3742	6.1431	33.7866	27.5554	0.0007	-
BH2 x 10	15.1101	0.6402	3.7003	3.1643	-	-
BH3	152.6187	1.8712	0.9389	1.7628	0.0046	-
BH3 x 10	15.5879	0.2218	0.2984	0.7220	-	-

Table A.2: Summary of major anions in groundwater samples. Values in red are above the calibrated detection limit and was diluted 10 times.

ID	F [mg/L]	Cl [mg/L]	SO_4 [mg/L]	Br [mg/L]	NO_3 [mg/L]	PO_4 [mg/L]
BH1	-	204.559	91.946	0.377	0.352	-
BH1 x 10	-	20.304	9.191	0.273	0.305	-
BH2	1.57	184.54	134.69	2.40	0.32	-
BH2 x 10	0.15	18.21	13.46	0.50	0.33	-
BH3	1.71	49.60	51.48	0.42	0.35	-
BH3 x 10	0.10	4.84	5.03	0.35	0.36	-

A.3 Surface Water Chemistry

For some of the samples the measured value was higher that the calibrated detection range, and the sample was diluted to ten times its volume and measured again. From table A.3 & A.4 is it apparent that the diluted samples have a measured value approximately ten times lower than the original sample. This gives reason to believe that the originally measured value can be used as an estimate for major ion concentration in the water.

Table A.3: Summary of major cations in river water samples taken in the period 25^{th} - 31^{th} of August 2020. Values in red are above the calibrated detection limit and was diluted 10 times.

ID	Na [mg/L]	K [mg/L]	Mg [mg/L]	Ca [mg/L]
Solvang K (G1)	26.3376	5.0934	4.4012	79.9039
Solvang K (G1) x 10	2.6373	0.5111	0.4275	8.0150
Konvallveien (G2)	24.8680	2.1487	4.2948	50.3819
Konvallveien (G2) x 10	2.5649	0.2243	0.4163	5.0393
Nils Bays vei (G3)	7.0342	1.9790	2.7202	38.8347
Nils Bays vei (G3) x 10	0.6955	0.1880	0.2573	3.8123
Blindern T (G4)	38.0236	7.6468	6.9941	67.7918
Blindern T (G4) x 10	3.7775	0.7402	0.7197	7.5872
Sognsvann (S1)	2.2508	0.3277	0.5477	4.8506
Rikshospitalet (S2)	3.9491	0.9112	0.9954	12.1606
Rikshospitalet (S2) x 10	0.4122	0.1093	0.0785	1.1653
Anne Maries vei (S3)	4.9341	0.7918	1.2198	15.4460

Table A.4: Summary of major anions in river water samples taken in the period 25^{th} - 31^{th} of August 2020. Values in red are above the calibrated detection limit and was diluted 10 times.

ID	F [mg/L]	Cl [mg/L]	SO_4 [mg/L]	Br [mg/L]	NO_3 [mg/L]	PO_4 [mg/L]
Solvang K (G1)	0.184	41.883	39.994	0.269	9.078	0.153
Solvang K (G1) x 10	-	4.118	3.950	0.267	1.049	-
Konvallveien (G2)	0.292	25.770	31.155	0.267	3.673	-
Konvallveien (G2) x 10	-	2.547	3.101	0.267	0.593	-
Nils Bays vei (G3)	0.108	10.825	11.433	0.261	4.610	0.029
Blindern T (G4)	0.182	62.891	63.307	0.488	5.020	-
Blindern T (G4) x 10	-	6.329	6.414	0.275	0.672	-
Sognsvann (S1)	-	-	-	-	-	-
Rikshospitalet (S2)	0.035	4.957	6.244	0.260	1.474	-
Anne Maries vei (S3)	0.024	6.072	8.135	0.260	1.183	-

A.4 Pore Pressure

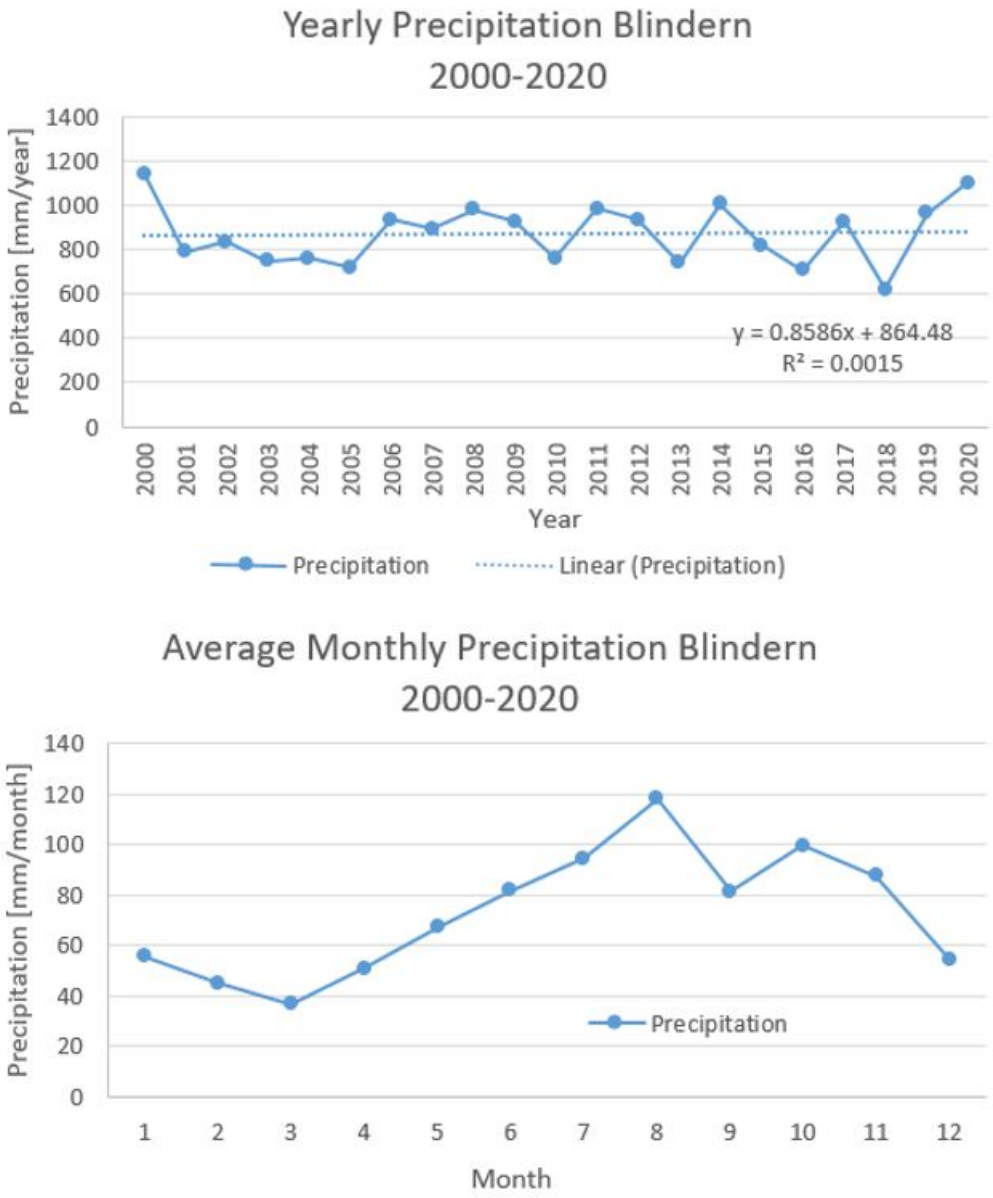

Figure A.24: Yearly and monthly average precipitation at Blindern from 2000 - 2020. Data from XGEO.no.

Table A.5: Average pore pressure and piezometric surface in the hydrological year 2020.

	Average	1σ	2σ
PZ68B 8m			
Pressure (kPa)	48.57	0.88	0.09
Piezometric Surface (m.a.s.l.)	91.25	1.77	0.18
PZ68B 29m			
Pressure (kPa)	224.94	2.52	5.05
Piezometric Surface (m.a.s.l.)	88.24	0.26	0.51
PZ81 8m			
Pressure (kPa)	44.47	1.55	3.10
Piezometric Surface (m.a.s.l.)	94.33	0.16	0.32
PZ81 13.7m			
Pressure (kPa)	88.04	3.54	7.08
Piezometric Surface (m.a.s.l.)	93.08	0.36	0.72
PZ90 8m			
Pressure (kPa)	50.13	2.09	4.17
Piezometric Surface (m.a.s.l.)	93.31	0.21	0.43
PZ90 16m			
Pressure (kPa)	135.75	1.51	3.03
Piezometric Surface (m.a.s.l.)	94.04	0.15	0.31
PZ91 8m			
Pressure (kPa)	33.70	3.95	7.91
Piezometric Surface (m.a.s.l.)	84.74	0.40	0.81
PZ91 24m			
Pressure (kPa)	217.58	2.72	5.43
Piezometric Surface (m.a.s.l.)	87.49	0.28	0.55
PZ92 8m			
Pressure (kPa)	30.02	5.23	10.46
Piezometric Surface (m.a.s.l.)	83.06	0.53	1.07
PZ92 25m			
Pressure (kPa)	220.29	2.93	5.87
Piezometric Surface (m.a.s.l.)	85.46	0.30	0.60
PZ93 8m			
Pressure (kPa)	53.55	2.33	4.67
Piezometric Surface (m.a.s.l.)	82.06	0.24	0.48
PZ93 37m			
Pressure (kPa)	371.20	4.74	9.47
Piezometric Surface (m.a.s.l.)	85.45	0.48	0.97
PZ94 8m			
Pressure (kPa)	43.32	6.65	13.29
Piezometric Surface (m.a.s.l.)	89.02	0.68	1.36
PZ94 24m			
Pressure (kPa)	182.65	2.90	5.79
Piezometric Surface (m.a.s.l.)	87.22	0.30	0.59
PZ95 8m			
Pressure (kPa)	12.35	6.46	12.92
Piezometric Surface (m.a.s.l.)	91.66	0.66	1.32

Table A.7: Average pore pressure and piezometric surface in the hydrological year 2021.

	Average	1σ	2σ
PZ68B 8m			
Pressure (kPa)	48.37	1.42	2.85
Piezometric Surface (m.a.s.l.)	91.23	0.15	0.29
PZ68B 29m			
Pressure (kPa)	218.07	2.51	5.02
Piezometric Surface (m.a.s.l.)	87.54	0.26	0.51
PZ81 8m			
Pressure (kPa)	44.39	2.09	4.19
Piezometric Surface (m.a.s.l.)	94.33	0.21	0.43
PZ81 13.7m			
Pressure (kPa)	75.19	3.83	7.67
Piezometric Surface (m.a.s.l.)	91.77	0.39	0.78
PZ90 8m			
Pressure (kPa)	47.37	3.26	6.52
Piezometric Surface (m.a.s.l.)	93.03	0.33	0.66
PZ90 16m			
Pressure (kPa)	129.33	2.17	4.34
Piezometric Surface (m.a.s.l.)	93.39	0.22	0.44
PZ91 8m			
Pressure (kPa)	27.81	1.35	2.70
Piezometric Surface (m.a.s.l.)	84.14	0.14	0.28
PZ91 24m			
Pressure (kPa)	208.46	1.82	3.64
Piezometric Surface (m.a.s.l.)	86.56	0.19	0.37
PZ92 8m			
Pressure (kPa)	29.15	5.72	11.43
Piezometric Surface (m.a.s.l.)	82.97	0.58	1.17
PZ92 25m			
Pressure (kPa)	211.29	5.20	10.40
Piezometric Surface (m.a.s.l.)	84.55	0.53	1.06
PZ93 8m			
Pressure (kPa)	51.61	0.83	1.66
Piezometric Surface (m.a.s.l.)	81.86	0.08	0.17
PZ93 37m			
Pressure (kPa)	358.45	6.92	13.84
Piezometric Surface (m.a.s.l.)	84.15	0.71	1.41
PZ94 8m			
Pressure (kPa)	40.31	10.06	20.11
Piezometric Surface (m.a.s.l.)	88.71	1.03	2.05
PZ94 24m			
Pressure (kPa)	170.78	6.10	12.19
Piezometric Surface (m.a.s.l.)	86.01	0.62	1.24
PZ95 8m			
Pressure (kPa)	11.40	6.92	13.84
Piezometric Surface (m.a.s.l.)	91.56	0.71	1.41